AD-A112 088 FOREIGN TECHNOLOGY DIV WRIGHT-PATTERSON AFB OH F/G 9/5
ANTENNAS.(U)
MAR 82
UNCLASSIFIED FTD-ID(RS)T-1168-81 NL

1 OF 2
AD-A
[illegible]

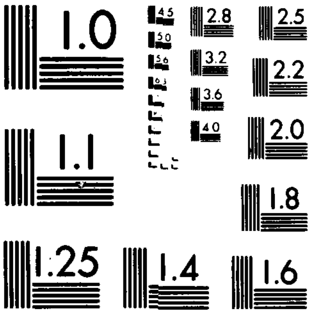

MICROCOPY RESOLUTION TEST CHART

NATIONAL BUREAU

2

FTD-ID(RS)T-1168-81

FOREIGN TECHNOLOGY DIVISION

AIR FORCE SYSTEMS COMMAND

ANTENNAS

Approved for public release;
distribution unlimited.

FTD -ID(RS)T-1168-81

EDITED TRANSLATION

FTD-ID(RS)T-1168-81 3 March 1982

MICROFICHE NR: FTD-82-C-000281

ANTENNAS

English pages: 177

Source: Antenny, Nr. 4, 1968, pp. 1-136

Country of origin: USSR
Translated by: LEO KANNER ASSOCIATES
F33657-81-D-0264
Requester: USAMICOM
Approved for public release; distribution unlimited.

A

PREPARED BY:

TRANSLATION DIVISION
FOREIGN TECHNOLOGY DIVISION
WP-AFB, OHIO.

Table of Contents

U. S. BOARD ON GEOGRAPHIC NAMES TRANSLITERATION SYSTEM

Block	Italic	Transliteration	Block	Italic	Transliteration
А а	*А а*	A, a	Р р	*Р р*	R, r
Б б	*Б б*	B, b	С с	*С с*	S, s
В в	*В в*	V, v	Т т	*Т т*	T, t
Г г	*Г г*	G, g	У у	*У у*	U, u
Д д	*Д д*	D, d	Ф ф	*Ф ф*	F, f
Е е	*Е е*	Ye, ye; E, e*	Х х	*Х х*	Kh, kh
Ж ж	*Ж ж*	Zh, zh	Ц ц	*Ц ц*	Ts, ts
З з	*З з*	Z, z	Ч ч	*Ч ч*	Ch, ch
И и	*И и*	I, i	Ш ш	*Ш ш*	Sh, sh
Й й	*Й й*	Y, y	Щ щ	*Щ щ*	Shch, shch
К к	*К к*	K, k	Ъ ъ	*Ъ ъ*	"
Л л	*Л л*	L, l	Ы ы	*Ы ы*	Y, y
М м	*М м*	M, m	Ь ь	*Ь ь*	'
Н н	*Н н*	N, n	Э э	*Э э*	E, e
О о	*О о*	O, o	Ю ю	*Ю ю*	Yu, yu
П п	*П п*	P, p	Я я	*Я я*	Ya, ya

*ye initially, after vowels, and after ъ, ь; e elsewhere.
When written as ë in Russian, transliterate as yë or ë.

RUSSIAN AND ENGLISH TRIGONOMETRIC FUNCTIONS

Russian	English	Russian	English	Russian	English
sin	sin	sh	sinh	arc sh	$\sinh^{-1}$
cos	cos	ch	cosh	arc ch	$\cosh^{-1}$
tg	tan	th	tanh	arc th	$\tanh^{-1}$
ctg	cot	cth	coth	arc cth	$\coth^{-1}$
sec	sec	sch	sech	arc sch	sech^{-1}
cosec	csc	csch	csch	arc csch	csch^{-1}

Russian	English
rot	curl
lg	log

FIVE-METER SPHERICAL MILLIMETER-BAND ANTENNA

P.M. Geruni

This article presents the basic parameters of millimeter- and centimeter-band spherical twin-reflector antennas in which the diameter of the large stationary reflector is about 5 meters.

The choice of parameters is substantiated and data are presented on the design execution. Information is given on spatial orientation, on the automatic control system and on the radiometer. Some findings from experimental investigation of the antenna and measurements of the solar and lunar temperature at a wavelength of 8 mm are presented

INTRODUCTION

The five-meter spherical twin-reflector antenna system (DAS-5) deployed near the village of Byurakan in the Armenian SSR at an altitude of 1600 meters above sea level is a precision instrument designed for radioastronomical and radiophysical research in the millimeter and centimeter wavebands. Another goal of creating this antenna was to check the operation of a twin-reflector antenna system with a spherical stationary main reflector and to find optimal relationships within such a system. In this sense, the DAS-5 is a prototype for studying the possibility of creating larger instruments within this system.

Development and work on building the DAS-5 began in late 1960-early 1961. The first integrated tests were made in May of 1966, and work on measuring the antenna parameters was carried out between September and November 1966.

The basic operating principles and questions relating to the theory and analysis of twin-reflector antennas with a large spherical reflector were examined in [1,2]. Specific material relating to this antenna will be presented below

SELECTION OF PARAMETERS. RADIOPHYSICAL DATA

Figure 1 shows the schematic diagram of the spherical twin-reflector antenna and presents basic notation. The second (small) reflector is used for total correction of spherical aberrations. In addition, it is used to change the direction of emission of the antenna over a wide range without distortion. In order to do this, it is only necessary to turn the small reflector about the center of the sphere without moving the large reflector.

The coordinates of the points of the profile of the small reflector, obtained from the equiphase condition of the field in the antenna aperture are provided by the relationships:

$$x = A_x - \rho \cos 2\Theta,$$
$$y = A_y - \rho \sin 2\Theta,$$

where

$$A_x = 1 - 2(1 - \cos\Theta)\cos^2\Theta,$$
$$A_y = \sin\Theta - (1 - \cos\Theta)\sin 2\Theta,$$
$$\rho = \frac{c^2 - (A_x - f)^2 - A_y^2}{2\,[c - (A_x - f)\cos 2\Theta - A_y \sin 2\Theta]},$$
$$c = 1 - 2l + f.$$

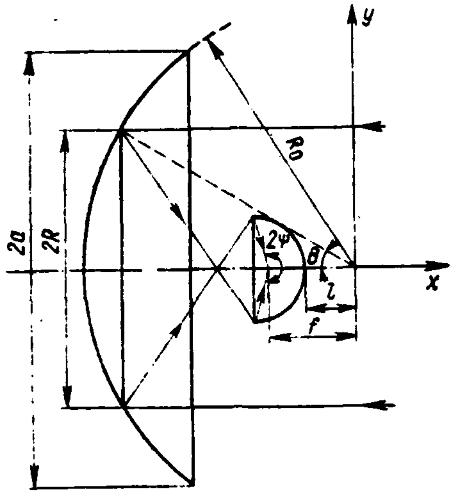

Fig. 1.

In order to realize a high utilization factor, to improve the noise tolerance of the antenna, and for design considerations as well, the small reflector was placed beyond the focal point of the large one ($\ell<0.5\ R_0$), and the following basic system parameters were used ($R_0=1$): c=0.6246, R=0.6293, a=0.7571, f=0.6046, ℓ=0.4900, X=0.6221. Y=0.1002, where X and Y are the coordinates of the extreme points of the small reflector, and 2R is the diameter of the utilized (or irradiated) aperture.

These parameter values were selected on the basis of the following premises:

1. A millimeter-band antenna of this diameter should be used primarily for investigating heavenly bodies within the Solar System. Consequently, a view of the sky within the meridional plane within ±25° of the zero declination point is sufficient. This is determined by the ratio R/a (the geometric aperture utilization factor).

2. Since the absolute dimensions of the antenna and the small reflector are small, it made no sense to attempt to minimize the dimensions of the latter just to simplify construction.

By increasing Y slightly, it was possible to obtain a higher geometric aperture utilization coefficient, i.e., the ratio of the "illuminated" aperture to the total aperture. These considerations are at the basis of the ratio Y/R. The shadow from the small reflector is 2.5% of the area of the utilized aperture (πR^2). In addition, X and Y are selected such that the edges of the small reflector fall short of reaching the focal plane of the large reflector by the amount 2λ in the middle of the band.

3. The apex of the small reflector is located 32 mm (i.e., more than 3λ for millimeter-band waves) above the apex of the focal surface of the large reflector; hence $\ell=0.49$.

4. The aperture angle 2ψ of the small reflector is ~200°, which makes it easier to obtain a low level of irradiation of the edges of the small reflector, and helps to produce nearly uniform field amplitude distribution across the active aperture of the large reflector in this particular scheme [2]. Besides providing high efficiency, the use of a large aperture angle also meets the requirements of providing a low level of internal antenna noise. These are the considerations involved in the choice of f.

5. The value of the constant c is determined uniquely by the choice of ℓ and $f(R_0=1)$.

These premises, plus a number of other factors (constructiveness and adaptability to manufacture, convenience in operating and control, etc.), determine these final data (dimensions in millimeter):
$R_0=3200$; $2a=4850$; $2R=4000$; $f=1935$; $\ell=1568$; $2Y=641$; $X-\ell=423$.

If $S_{3\Phi\Phi}=\pi R^2_{3\Phi\Phi}$ is the effective area of the antenna, we call $R^2_{3\Phi\Phi}/R^2$ the aperture utilization factor (kip). As usual, this is the product of a number of components: the power (amplitude) dissipation kip, the shading kip, etc. the ratio R^2/a^2 is conveniently called the geometric kip (kipg), while $R^2_{3\Phi\Phi}/a^2$ is the total kip (kipp).

Since the total (geometric) area of the aperture of the large reflector in the DAS-5 is 18.5 m^2, the utilized aperture area 12.6 m^2 and the effective area 9 2 m^2 (see below), the kip is 0.73, and the kipp=0.5 (kipg=0.685).

The waveband of the DAS-5 extends from 2mm to 12 cm. The antenna can operate without using the second reflector at longer wavelengths (to 1 m). At a wavelength of 4 mm, the diameter of the utilized aperture is 1000λ .

In order to define the tolerances for installation of the system elements, phase distortions in the aperture were analyzed when the parameters deviate from the calculated values. Computer analyses yielded the following values: the accuracy with which the small reflector is placed along the x axis is ±0.6 mm, and ±0.3 mm on the y axis; the accuracy of focal placement of the reflector is ±1.2 mm along the x axis and ±0.8 mm along the y axis. The precision of the surface of the large reflector is ±0.3 mm, and ±0.2 mm for the small reflector. The precision with which the radius of curvature of the large reflector is executed is ±0.8 mm. Deflection of the small reflector suspension must not exceed ±1 minute of arc. These are the maximum tolerable deviations for which the greatest phase errors in the aperture at a wavelength of 8 mm do not exceed $\lambda/20$, or 18°.

CONSTRUCTION

The large reflector, 4850 mm in diameter and weighing 4 tons, was cast in eight wedge-shaped pieces of aluminum-zinc alloy. The casting was done in a special molding frame from a wood model. The radius of curvature of the reflector was to have been approximately ~~32~~ 3200 mm after mechanical polishing. The castings were 50 mm thick, with stiffening ribs 150 mm thick.

In order to polish the reflector, a rotary grinding tool was set up at the antenna site (Fig. 2). The reflector (1) was assembled in a rigid frame (2) and placed on a turning table (3) with a vertical axis of rotation. A grinding head (5) holding an end-milling cutter was fastened to a boring bar (4) which rotates (through 50°) about the center of curvature of the reflector and which is counterbalanced by counterweight (6). The entire structure rested on an 8x8 meter concrete foundation (7). The drive mechanisms for the table, boring bar, milling head, etc., were controlled from a main and a portable panel. The table drive was built with adjustable d.c. motors. The speed was varied in order to maintain a constant grinding mode.

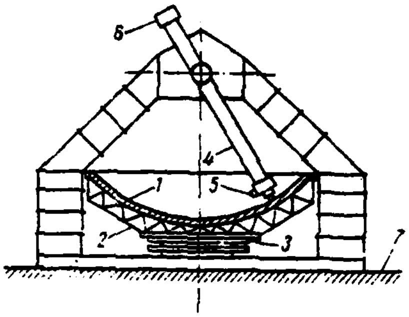

Fig. 2.

Figure 3 shows the setup in operation. Several "rough" and two "clean" surface layers were cut from the reflector. The depth of the cut during the last pass was 0.5 mm. In order to maintain a constant temperature while removing the "clean" layers, the entire setup was covered with a tarpaulin, and work was done only at certain times of day. The main difficulties involved controlling vibration, play and temperature deformations, and of monitoring coincidence of the vertical axis of rotation of the table and the horizontal axis of rotation of the boring arm. Were this not done, a toroid would have resulted rather than a sphere. The sphericity was monitored, and the co-axiality adjusted, by cutting a radial "control" strip across the reflector (Fig. 4.) and then turning the table through 180° and measuring the difference of the readings of micron indicator 1 (Fig. 4a) fastened to "flag" 2. By regulating the position of the boring arm shaft, coaxial deviation was reduced to within ±0.1 mm of zero.

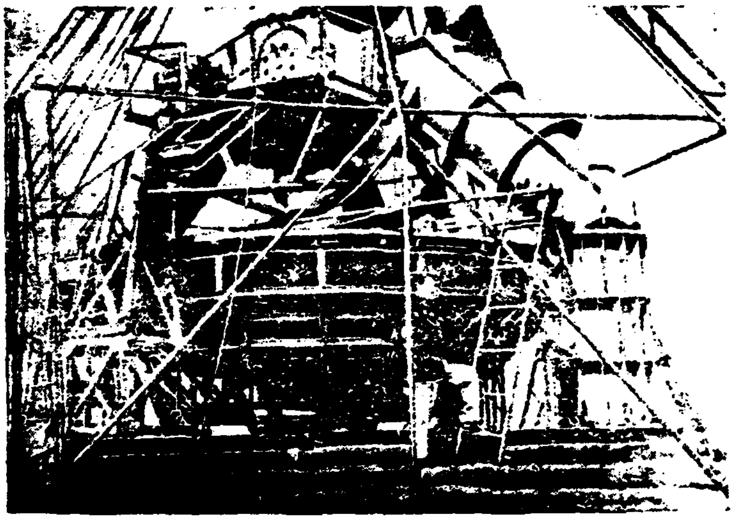

Fig. 3.

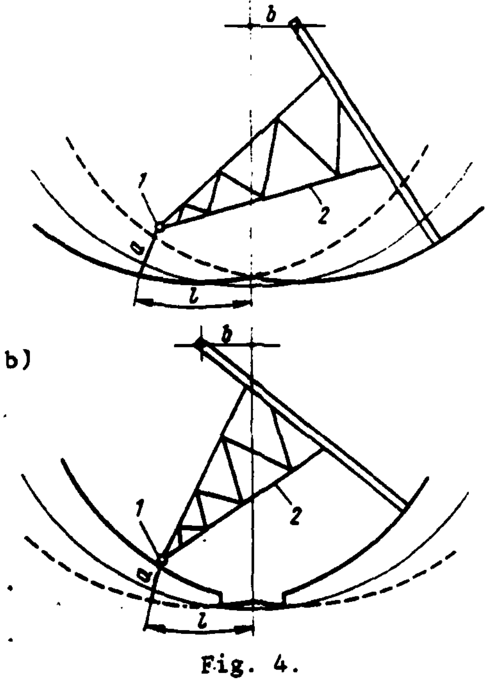

Fig. 4.

A series of measurements of the reflector surface after polishing indicated that it had been finished to within ±0.25 mm (maximum error).

Certain difficulties were overcome in measuring the absolute radius of curvature. As a result of repeated measurements, a value of R_0=3202.7 mm was obtained.

After this work, the polishing assembly was removed, and then the mirror, permanently fixed to the supporting foundation, was tilted 40° to the south together with the base (cf. below).

A tripod made of double-walled tubing (to provide high rigidity even though the diameter is small) was used to hold the central and cardan frames holding the gears and drive mechanisms which move the shaft which turns the small reflector. Then the "yoke", small reflector and counterweights were put in place.

The profile of the small reflector was designed by computer with a 0.1 mm step (considering R_0=3202.7 mm). The reflector itself was cast of duralumin in a mold from a wood model and finished on a lathe to within ±0 2 mm.

The small reflector and "yoke" were made coaxial during finishing, and then trued optically. According to geodetic measurements, the deflection of the "yoke" did not exceed 1' at the maximum angles from vertical even with the additional load imposed by the small reflector.

The total shadowing of the structures in front of the large reflector comprises 9-11% of the area of the utilized aperture (depending upon the spatial position of the beam).

The "yoke" holds the drive mechanism which is used for remote adjustment of the suspension of the small reflector, which provides setting accuracy of ±0.1 mm over a range of ±30 mm.

The antenna feed and receiver waveguide sections are installed at the focus of the small reflector on an adjustable tripod made of chrome-plated rods 10 mm in diameter. The entire feed assembly can be moved smoothly along the antenna shaft through a range of ±35 mm during adjustment. The feed assembly creates no additional shadowing

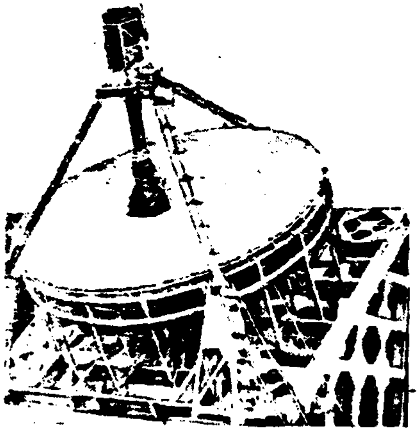

Fig. 5.

The shaft on which the small reflector turns was set to intersect the center point of the large sphere experimentally, using a micron indicator fastened to the yoke and touching the surface of the large reflector. This work was only done at a particular time of day as well. After the large reflector had been rotated again and finally set in place, the surface accuracy was re-checked. No significant deviations were noted.

Figure 5 shows an external view of the antenna.

SPATIAL ORIENTATION

The main area of application of the DAS-5 antenna in radio astronomy is the millimeter waveband. In the millimeter band, we can expect to receive thermal radiation, which with a 10 m^2 antenna area actually reduces the problem to that of working with radiation sources within the Solar System: in this case there is no need for a wide view of the sky. In order to ensure year-round observation, a declination view within limits of $\delta=\pm 25^\circ$ is, generally speaking, sufficient.

In order to provide a view of this declination sector, the main axis of the antenna is directed along the line of the intersection of the planes of the equator and the local meridian. The antenna beam is able to move through an angle of 25° on both sides of the main axis. Figure 6a shows the orientation of the field of view of the antenna. A conical viewing sector with an apical angle of 50° facilitates the observation of each radiation source for an average of 2 hours daily near the highest apparent altitude (Fig. 6b). The viewing time (in hours) can be calculated using the formula

$$t^h = 0{,}133 \arccos\left[\frac{\cos\alpha}{\cos\delta\cos(\varphi-\psi)} \mp \tan\delta\,\tan(\varphi-\psi)\right], \qquad (9)$$

where for our case the latitude of the site $\phi=40^\circ$, the angle of inclination between the beam and the main axis $\alpha=25^\circ$, and the angle of inclination of the main axis from the zenith point (in the meridian plane) $\psi=40^\circ$.

With an angle of beam deviation of 23° from the main axis, distortions in the directivity pattern due to loss of aperture area approach 8% [2]. The losses result from the fact that when $\alpha>13^\circ$ part of the utilized aperture "extends" beyond the edges of the large reflector.

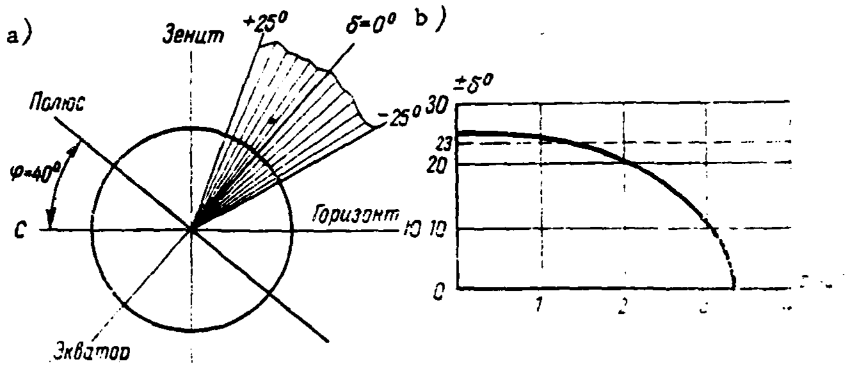

Fig. 6.
Key: (1) pole; (2) zenith; (3) horizon; (4) Equator.

CONTROL SYSTEM

The automatic control system is designed using a plan [4] which allows the influence of yoke deformations to be eliminated. In order to accommodate the optical radiator, the construction of the cardan frame provides a free area near the center of the large sphere. However, since the yoke of this antenna is rigid, the automatic control system thus far uses an ordinary scheme in which the error signal is simulated (or comes from a photoelectric guiding device). The control panel is housed in a small building located 60 meters from the antenna. There is a coarse and a fine scale for each shaft. The shaft and scale gears are high-precision, as are the gears in the main drives of the small reflector; the system used is a parallax system. The main motors are powered from electronic and magnetic amplifiers. The speed of the small reflector can be varied continuously for both shafts separately. The maximum speed is 20 deg/min for both shafts. The guidance accuracy is no worse than 1 minute of arc. There is a remote control panel on the top antenna frame. An optical guidance telescope with a 0.5° field of view is also installed there on the counterweights. The system is also equipped with a precise automatic photoelectric guidance device for the Sun and Moon. The control panel also has quartz clock scales for solar and stellar time. The control system allows a scanning mode following some defined rule to be imposed on the basic beam guidance mode during manual or photoelectric guidance. The length of the yoke, i.e., the suspension height of the small reflector, is adjusted from the control panel. The control panel communicates with the antenna via a duplex radiotelephone link.

RADIOMETER

The λ=8mm wavelength radiometer uses an ordinary superheterodyne modulation circuit, with an amplitude modulator. Figure 7 shows a functional diagram of the high frequency section. This section of the radiometer is located at the focus along the shaft of the small reflector (Fig. 8). The i-f preamplifier, power supply filters, auxiliary electric motors, etc. are fastened to the outside of the small reflector.

The operations building, located 60 meters from the antenna, contains the other sections of the radiometer: the i-f amplifier, low-frequency amplifiers, synchronous detector, oscillators, power supplies and recording equipment. An adjacent room contains a Nairi computer which is used for calculations. The basic specifications of the present version of the radiometer are as follows: modulation frequency -- 32 Hz (rectangular), i-f carrier -- 57 MHz, i-f preamplifier gain 20, i-f amplifier -- 10^5, ℓ-f amplifier 10^4; the i-f preamplifier-i-f amplifier bandpass is 7 MHz. The resultant sensitivity is 15°K with a 2-second time constant.

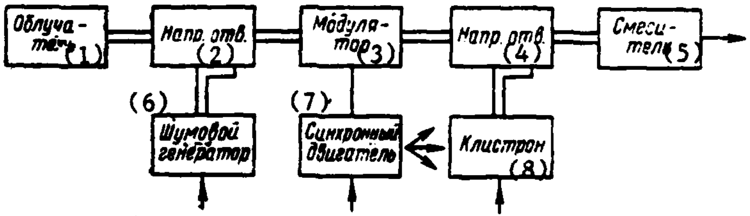

Fig. 7.

Key: (1) feeder; (2) directional coupler; (3) modulator; (4) directional coupler; (5) mixer; (6) noise generator; (7) synchronous motor; (8) klystron.

The radiometer is calibrated by means of a type GSh-6 argon noise tube inserted in the waveguide and connected to the circuit through a 10 dB directional coupler. The spectral density is 61 kT. Ignition is done remotely from the radiometer racks in the operations building. The constant component of the mixer current, synchronous operation of the modulator, etc., are also monitored there.

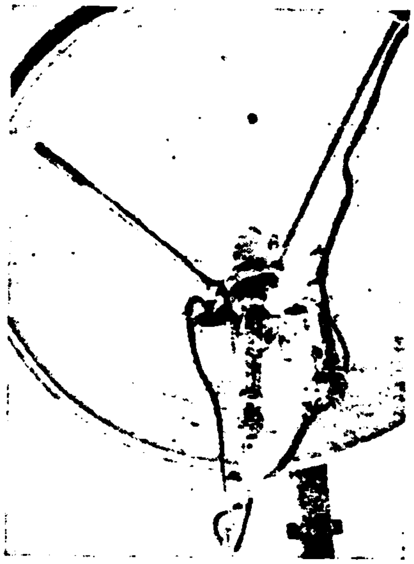

Fig. 8.

EXPERIMENTAL RESULTS

Experimental investigation of the antenna parameters involved a number of difficulties. Since the antenna cannot "look" any lower than 25° to the horizon (south), and the boundary of the far zone for $\lambda=8$ mm is 3-4 km away and the terrain itself drops off to the south, parameters cannot be taken using a tower-mounted oscillator. A tower 100 meters high is needed even at a distance of 250 meters. The use of helicopters and aerial balloons is very difficult, since the expected directivity pattern width is only a few minutes of arc even at $\lambda=8$ mm. This leaves only radioastronomical methods. The brightest "point" source is Venus. The expected antenna temperature from Venus for the center phase is $2^{o}K$ (at a wavelength of 8 mm). Such a signal can be received only with an adjusted antenna and improved radiometer. The only possibility of measuring the pattern now is thus to use the edge of the Solar and Lunar disc. Unfortunately, the accuracy of this method is low, and side lobes are practically impossible to measure.

Preliminary trueing of the antenna was done using optical methods. The quality of finish of the surface of the large reflector makes acceptable optical reflection possible. For this reason, the quality of the large reflector could be given a positive evaluation in advance, since the focal surface was clearly described in space when the reflector was illuminated by the Sun or Moon. The paper began to char at a quasi-focal spot (apex of focal surface) 5-7 cm in diameter. The small reflector was polished in order to do the optical trueing. When the small reflector is positioned correctly, the focal spot from the Moon (it was impossible to work with the Sun because of the extreme brightness and high temperature in the small reflector) had a slightly elongated shape and was 2-3 cm in diameter. When a lamp was placed at the focus (even a very weak one) it was possible to see the focal surface (of the large reflector) and a "utilized" spot 4 meters in diamter on the large reflector with very sharp edges. The amplitude distribution in the aperture corresponded to uniform irradiation of the small reflector, i.e., the intensity in the utilized spot increased sharply toward the edges.

In order to obtain near-uniform amplitude distribution in the antenna aperture, special waveguide feeders were developed and tested at $\lambda=8$ mm which created a strong field at small angles to the axis. Figure 9a,b shows one such feeder and its directivity pattern in two planes, taken experimentally, SWR=1.13.

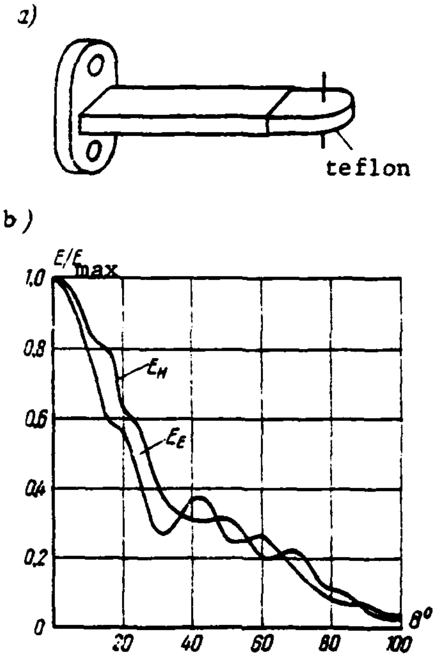

Fig. 9.

In order to evaluate the internal antenna noise, two "levels" were recorded: the level of "internal" noise was recorded with the antenna aimed at an angle of 30° to zenith, then the level was measured with an unmatched load at the radiometer input (~300°K); finally, the level was measured with the noise generator activated (~1600°K). Allowing for the quality of the matching of the input load, the amount of attenuation in the directional coupler, tropospheric noise and other factors, a value of 10-15°K was obtained for the internal antenna noise.

Figure 10 shows examples of the recording of Solar (a) and Lunar (b) radiation at $\lambda = 8$ mm. The calibration pulses from the noise generator can also be seen here.

In order to determine the directivity pattern of the antenna, the average envelope was constructed from the recording (Fig. 10a) and its first derivative found. At half-power, the width of the main lobe is 6.5-7 minutes of arc (the

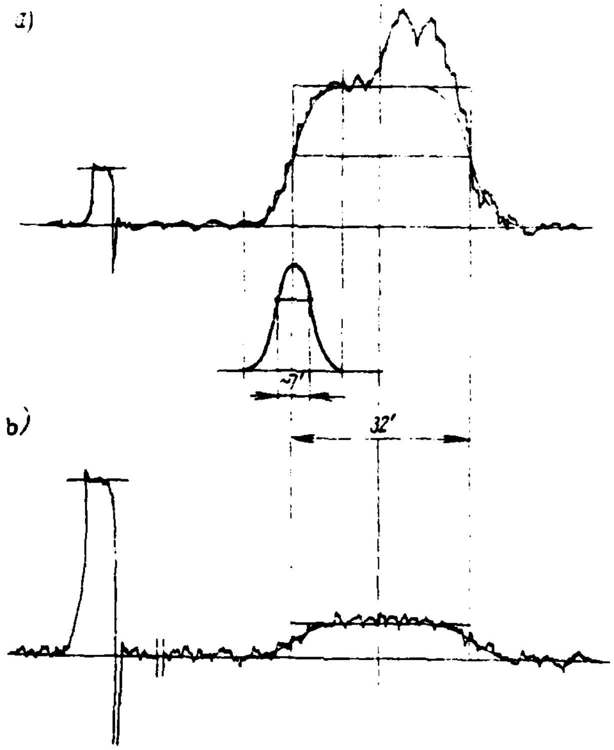

Fig. 10.

feeder receives only a single linearly polarized field component). This recording of the Sun contains radiation from a group of spots on the right half (of the recording) of the Solar disc. Since the angular dimensions of active formations in the region of sun spots are smaller than the angular dimensions of the antenna directivity pattern, when they pass through the pattern, the plot of the recording imitates the shape of the pattern. The figure shows recording of the main lobe of the directivity pattern from two adjacent spots. Measurements of the pattern in the perpendicular plane (by scanning the Solar disc) also yielded a value of 6.5-7 minutes of arc for the half-power width of the main lobe.

Since the width of the directivity pattern at half power is less (by a factor of 5) then the angular dimensions of the source, we can assume with a certain degree of accuracy that we are dealing with a case of thermodynamic equilibrium, and the temperature at the antenna focus (antenna temperature T_a) must be approximately equal to the brightness temperature of the source $T_я$ [Translator's note: Subscript letter "я" indicates "brightness"]. The source is practically "seen" only by the main and first side lobes of the pattern; about 30% of the energy is dissipated in the other directions. In addition, energy is lost due to tropospheric absorption, losses in the antenna (efficiency), feeder (due to mismatch) and in the circuit (in the section between the feeder and the point at which the noise generator is connected). These losses comprise another 15%.

The energy of the noise generator is lowered when it reaches the receiver input due to attenuation in the directional coupler (about 10 dB) and losses due to non-ideal matching of the hot tube and the circuit. Considering these losses, the amplitude of the recording of the calibration signal at the receiver output corresponds to 1600°K. Since the amplitude of the Solar recording is accordingly 4000°K, considering the above we obtain $T_я=6700^{\circ}$ for the brightness temperature of the Sun, which agrees with previous observations [6].

Taking the radiation flux density of the Sun at $\lambda=8$ mm to be $235\cdot10^{-21}$ $w/m^2\cdot Hz$ [5], allowing for absorption in the troposphere (which is low in this case because of the dryness of the air and the high elevation above sea level), and introducing a factor which allows for the comparability of the angular dimensions of the source in the beam, we obtain a value of 9.2 m^2 for the effective antenna area. Calculation of the efficiency for the main lobe of the pattern $(2.3\cdot10^6)$ and allowing for the share of the others produces an analogous result. The utilization factor of the aperture area $kip=9.2/12.6=0.73$, while the gain $G=1.81\cdot10^6$, or 62.6 dB.

The values obtained for the area utilization factor, gain and noise temperature are preliminary and require further clarification. However, there is no reason to suppose that they will change significantly. Consequently, we can assert that the DAS-5 is a high-efficiency antenna, which provides convincing confirmation of the possibility of using a two-reflector spherical plan as the basis for building larger instruments. It must be emphasized that the value kip=0.73 which was obtained is unobtainable for fully-rotatable parabolic antennas of the same electrical dimensions. Close kip values have been obtained only for horn-parabolic antennas.

In Fig. 10b, the calibration pulse is reduced in scale. The amplitude of the Lunar recording is 150°K (the recording was made during a full Moon on 25 November 1966). Consequently, the average brightness temperature of the Moon across the disc is 240°K. An elevated brightness temperature of up to 270°K was recorded at the center of the disc.

CONCLUSION

A number of new experiments are now being undertaken to investigate the antenna parameters in detail.

Receiving equipment is also being fabricated to record planetary radiation at wavelengths of 8 mm and 4 mm.

In conclusion, the author is pleased to emphasize that the building of the DAS-5 antenna was the result of the labor of a large collective. Radio engineers and scientific colleagues Razmik Garsevanyan, Levon Nalbandyan, Grachik Arshakyan, Sergey Sarkisyan, Kima Karapetyan and others participated actively in calculating and designing the antenna, building, installing and adjusting the radio equipment and automatic control system. A leading role in developing and creating the antenna structures was played by design engineers and technologists Yuriy Simonyan, Garri Galstyan, Marlen Arakelyan, Georgiy Ter-Ovakimyan and others. A great deal of work and thought was invested in the fabrication of the antenna by master technicians Shmavon Voskanyan, Vage Minasyan, Artem Balyan, Zaven Aleksanyan and others.

Academician V.A. Ambartsumyan attended constantly to the building of the DAS-5 during all stages of work.

LITERATURE

1. Л. Д. Бахрах, И. В. Вавилова. «Радиотехника и электроника», т. VI, № 7, 1961, стр. 1146.

2. П. М. Геруни. «Радиотехника и электроника» т. IX, № 1, [illegible] 3

3. C. W. Tolbert, A. W. Straiton, L. C. Krause. — IEEE [illegible] AP-13, № 2, 1965, стр. 225

4. П. М. Геруни, Р. А. Саркисян. «Радиотехника» т. 19, [illegible] 64, стр. 34.

5. А. Д. Кузьмин, А. Е. Саломонович. Радиоастрономические измерения параметров антенн. М., «Советское радио», 1964.

6. В. В. Железняков. Радиоизлучение Солнца и планет. М., «Наука», 1964.

FLEXIBLE ELLIPTICAL WAVEGUIDES -- NEW CENTIMETER-BAND FEEDER LINES
(Review of Technical Status)

G.I. Troshin, E.F. Ykstin and V.A. Khudyakova

It is shown that elliptical waveguides are better than rectangular waveguides having the same cross-sectional perimeter with respect to attenuation. The maintenance of the polarization plane with respect to the cross section makes it preferable to a round waveguide. The flexibility of elliptical waveguides, their ability to be wound on drums, and the capability of making long (on the order of hundreds of meters) sections without flanges allows this type of feeder to be considered as basic, especially for mobile radio relay stations.

Analysis of the requirements imposed on modern centimeter-band feeder lines, as well as evaluation of the electrical, physical-mechanical and operating characteristics of these lines (coaxial cables, periscopic systems, single-conductor transmission lines, rectangular, round and elliptical waveguides) indicate that flexible elliptical waveguides are extremely promising.

An elliptical waveguide with the same cross-sectional perimeter as a square waveguide has less attenuation. The fact that the surface is corrugated makes it easy to make flexible waveguides which can be wound on drums.

The elliptical cross section makes it possible to retain the positioning of the polarization plane of the signal with respect to the cross section regardless of the manner in which the waveguide is installed, i.e., the positive feature of rectangular waveguides is retained.

Flexible elliptical waveguides provide maximum speed in setting up and dismantling mobile stations, along with low weight and the ability to deploy the equipment far away from the mast foundation.

This combination of positive qualities, together with satisfaction of the main requirements imposed on modern radio system, has brought many developers here in the USSR as well as abroad to investigate elliptical waveguides.

The matter of electromagnetic wave propagation in electrical waveguides was first resolved in 1938 by L. Chu [1]; however, practical work on elliptical waveguides has been underway only for the last 10-15 years.

This has been promoted especially by the development of mills for welding and corrugating long tubes from metal strips.

France, Germany and the U.S. have now developed and are producing a series of flexible corrugated elliptical waveguides for feeder systems operating in the 3000-12,000 MHz band. They are made of hollow round corrugated copper tubing fabricated from copper strips by welding and corrugating on machines specially built by the Hackethal company [5].

Electric-arc welding in an inert gas medium (argon-arc welding) is used. In this welding method, the two edges of the metal strip are melted by the electric arc and then fused together in an argon medium, forming a seam which is free of any significant rolls. The Hackethal company has developed three types of machines for argon-arc welding and corrugating round metal tubes of different diameters, some technical data on which are presented in Table 1.

Table 1

Machine indicators	Machine type		
	Minivema small machine	Univema universal machine	Grovema large machine
welded tube diameter, mm	up to 25.4	15.2-78.8	58.5-118
wall thickness, mm	0.2-0.4	0.3-0.6	0.5-0.7
output, m/min	6-24	3-15	2.4-9
machine length and width, m^2	5.5x2.1	9.6x2.4	12.6x3.0

All three machines use the same principle, which is shown schematically in Fig. 1. The machine consists of the following four basic assemblies [5]:

I. Assembly which forms tube from strip.
II. Tube welding section.
III. Belt traction assembly.
IV Tube corrugation assembly.

The shaping assembly consists of a cleaning (etching) tank, cutting and straightening rollers and tube shaping rollers.

The welding assembly is in the middle of the machine. The position of the welding head is adjusted by means of a special device. The end of the electrode and welding arc are observed through a system of lenses and light filters. A nozzle near the end of the electrode directs argon around the welding arc and the section of melted metal at the edges of the welded strip.

The traction device pulls the welded tubing through the machine at a uniform rate. Clamps fastened to the belt grip the tube without damaging it and keeping it from turning, and eliminates the torque produced by the corrugating device. The tube is corrugated by a wheel which turns in a medium of lubricating and cooling emulsions. Radial movement of the turning wheel sets the required corrugation depth, while the spacing is determined by the linear rate of movement of the tube and the speed of rotation of the wheel.

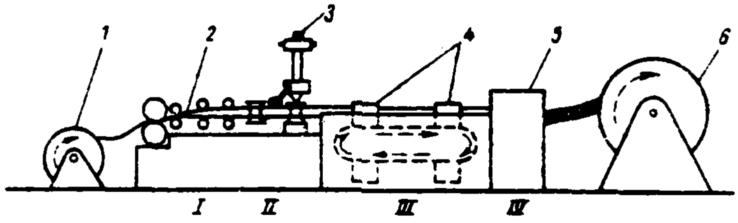

Fig. 1.

Key: 1 -- metal strip feed; 2 -- tube formation device; 3 -- welding head; 4 -- traction device with clamps; 5 -- corrugating device; 6 -- take-up drum; I -- shaping assembly; II -- welding assembly; III -- belt-type traction device; IV -- corrugating device.

The machines are equipped with a number of auxiliary devices which make it easy to obtain tubes with the required dimensions. These devices include tape thickness and width monitoring instruments, solution recovery devices, strip cleaning devices, metal strip feed devices, corrugated tube take-up devices, etc.

The argon-arc seam welding method has a number of advantages over other methods:

1. The welding operation is continuous and moves rather rapidly (3-19 m/min).

2. The method can be used for a number of metals (steel, aluminum, copper).

3. The method can be used successfully for welding strips between 0.2 and 2.5 mm thick.

4. No rolling occurs along the seam.

5. The concentrated but limited heating ensures uniform melting of the edges of the strip.

6. Limited heating area.

7. The argon protects the melted metal from oxidation during welding.

8. Hollow tubes can be welded without inserting a special tool.

In order to make flexible elliptical waveguides, the argon-arc welding and corrugating machine is augmented with a dye which is installed between the corrugation and take-up devices which converts the round cylinder into an elliptical one.

The initial experiments conducted in Germany to make elliptical waveguides used the outside conductor of type 14/42 and 10/30 coaxial cables [2]. The corrugated coaxial cable outside conductor, which had an inside diameter of 42 mm, was deformed into an ellipse with a long axis 2a=49 mm long and a small axis of 2b=35 mm (eccentricity e=0.7).

Deformation of the outside conductor of 10/30 coaxial cable produced an ellipse with dimensions of 2a=34.3 mm (long axis) and 2b=22 mm (short axis). The eccentricity of this ellipse was 0.765. The attenuation in the 4.4-5.5 GHz frequency band was measured for an elliptical waveguide (2a=49 mm and 2b=35 mm). Figure 2 shows the relationship which was found. Also shown is a comparison between the experimental findings and the results of measuring and calculating the attenuation in a brand R48 rectangular waveguide (made of copper with inside dimensions of 47.6x22.2 mm). It is apparent from the figure that the attenuation of the elliptical waveguide is 0.05-0.3 dB/m in the 4.4-5.4 GHz band, and is comparable with the attenuation of a standard rectangular waveguide in the same frequency band. The arithmetic mean of the coefficient of reflection in an elliptical waveguide 50 meters long did not exceed 0.075 in the 4.4-5 GHz band, while the maximum value was 0.19.

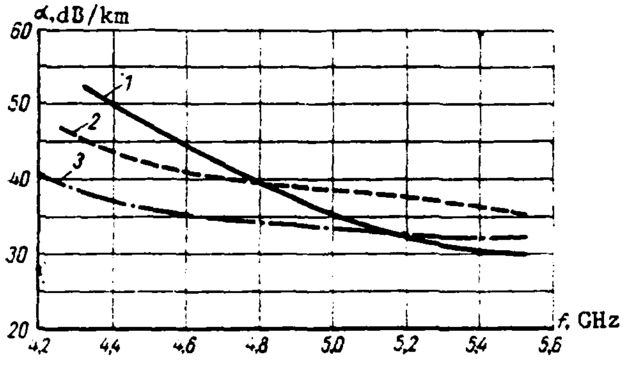

Fig. 2.

Key: 1 -- elliptical waveguide at 5 GHz (experiment); 2 -- R48 (experiment); 3 -- R48 (calculated).

Figure 3 shows the attenuation in an elliptical waveguide with dimensions of 2a=34.3 mm and 2b=22 mm as a function of frequency, found experimentally, in comparison with an R70 rectangular waveguide (made of copper, with inside dimensions of 34.8x15.8 mm). It is apparent from the figure that the attenuation of the elliptical waveguide between 6.5 and 8 GHz exceeds that in a standard rectangular waveguide by approximately 20%, amounting to 0.06-0.09 dB/m. The mean value of the coefficient of reflection for that waveguide, as determined for a segment 40 meters long, was 0.04; the maximum value was 0.07.

The flexibility of the elliptical waveguides was checked [4] by rewinding the waveguide in "S" fashion from one drum (0.1 m in diameter) to another while monitoring the waveguide performance with respect to coefficient of reflection after a particular number of rewindings. A slight increase in

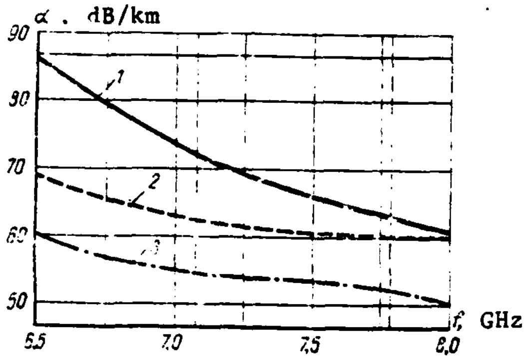

Fig. 3.

Key: 1 -- corrugated elliptical waveguide at 7.0 GHz (experiment); 2 -- R70 (experiment); 3 -- R70 (calculated).

coefficient of reflection was noted after 300 rewindings for a large-diameter waveguide (2a=49 mm, 2b=35 mm), and 200 rewindings for a smaller waveguide (2a=34.3 mm, 2b=22 mm), and some fine cracks (marks) were detected on the surface of the outside casing.

The initial experiments on constructing elliptical waveguides were thus promising.

A series of brand EN (where N is the center frequency of the band in hundreds of megahertz) of corrugated copper waveguides has been developed in Germany [3].

Table 2 presents the basic technical characteristics of this series of corrugated copper elliptical waveguides[1].

---

[1] According to data from the Telefunken Company.

Table 2

Марка эллиптического волновода (1)	Рабочий диапазон частот, МГц (2)	Наружные размеры эллипса по защитной оболочке (3)		Затухание, дБ/м, в средней части рабочего диапазона (4)	[illegible] (5)	(6)
		2a, мм	2b, мм			
E 40	3600÷4200	74	47	0,029	400	1,6
E 48	4400÷5000	57	43	0,043	400	1,3
E 62	5900÷6500	50	33	0,0477	400	1,07
E 68	6400÷7150	47	31	0,056	300	0,93
E 75	7100÷7800	40	29	0,069	300	0,78
E 84	7700÷8600	37	26	0,0898	300	[illegible]
E 100	8500÷10000	35	24	0,0977	300	0,54
E 120	10000÷12400	29	20	0,15	300	[illegible]

Key: (1) elliptical waveguide brand; (2) operating frequency range, MHz; (3) outside dimensions of ellipse measured across protective casing; (4) attenuation, dB/m, in center of working band; (5) minimum radius of curvature for a single bend in electrical plane, mm; (6) weight, kg/m.

The elliptical waveguides indicated in the table are made from a copper strip with composition close to that of domestic brand M1 copper with thickness of the order of 0.5 mm. An anticorrosive bitumen-based composition coats the outside surface of the corrugated elliptical tube. The protective casing is made of pigmented polyethylene with a radial thickness of 2-2.5 mm.

Elliptical waveguides of all dimensions are transported in long lengths wound on a drum 1200 mm in diameter and are delivered with end adapters which are square in shape, making it possible to hook up to any equipment. The elliptical waveguides are manufactured with high precision, and make possible a mean coefficient of reflection in the working frequency band of less than 0.05.

Since elliptical waveguides can be used successfully in mobile technical devices where great mobility is required, their mechanical characteristics are of great importance (maximum acceptable stretching force, number of acceptable bends, resistance to radial pressure, acceptable excess pressure within waveguide cavity, etc.). Because of the contradictory requirements imposed on the electrical and mechanical characteristics of the waveguide, and because of their variety, compromises must be made in the selection of their basic geometric dimensions. For example, flexibility and resistance to radial pressure will be the better, the deeper the corrugation and more closely it is spaced. However, from the viewpoint of resistance to axial stretching forces, a wide, shallow corrugation is desirable. The choice of waveguide cross section is analogous: while an elliptical cross section is required from the electrical viewpoint, a round shape is preferable mechanically.

Some investigations have been made of the mechanical characteristics of brand E48 flexible corrugated elliptical waveguides [4] (internal ellipse axes $2a_1=47.1$ mm, $2b_1=31.5$ mm; external ellipse axes $2a_2=53.4$ mm, $2b_2=38.1$ mm), as well as brand E75 (internal ellipse axes $2a_1=33.1$ mm, $2b_1=19.5$ mm, external ellipse axes $2a_2=37.4$ mm, $2b_2=24.1$ mm). We know that when the waveguide is removed from the drum and hoisted onto the antenna tower, or when the waveguide is suspended freely, axial stretching forces arise which cause stretching of the waveguide along the longitudinal axis and compression of the short axis of the ellipse.

The investigations of both types of waveguides indicated, depending upon the axial stretching force, that they operate within the elastic deformation limits up to a defined load magnitude. This load is 70 kg for the E48, and 100 kg for the E75. When the load is increased beyond these values the process becomes irreversible, and residual stretching occurs. For example, if a flexible E75 waveguide is subjected to an axial stretching force of 215 kg, the stretching under load amount to 0.435%, with residual stretching of 0.1%.

The experiments indicated that the maximum tolerable stretching load is about 143 kg for the E48 waveguides, and 124 kg for the E75, with residual stretching not exceeding 0.02%. The acceptability of this load from the viewpoint of electrical characteristics depends upon the acceptable deformation of the axes of the ellipse. For example, when an axial load of 138 kg is applied to a flexible E75 waveguide, the short axis shrinks by 0.056 mm, with residual reduction of that axis of 0.023 mm after the load is removed. The research showed that a reduction of the length of the short axis of the ellipse of 0.044 is tolerable from the viewpoint of electrical characteristics. Based on this, it was established that the flexible E48 waveguide can withstand a stretching force of up to 100 kg, and an E75 -- up to 110 kg. With the 1.3 kg/m running weight of the E48 waveguide and 0.78 kg/m of the E75 this means that a suspended E48 waveguide can span 77 meters, and an E75 -- 141 meter. Under these circumstances, there is no danger of residual deformation of the short axis exceeding 0.04 mm. Experiments conducted to determine the destruction loads indicated that the E48 waveguide breaks under a stretching force of 1870 kg, and the residual stretching amounts to 29%. These values are smaller for the E75 waveguide, equalling 1190 kg and 18%.

In order to find the acceptable loading along the axis of the ellipse when it is fastened in place using clamps, experiments were conducted to compress the waveguides between two parallel steel plates which created a linearly distributed load acting along the short axis of the ellipse. If we use an acceptable deformation of the short axis of the ellipse of 0.04 mm, the tolerable load for the E48 waveguide is 34 kg, and 26 5 kg for the E75. Comparative testing of standard R48 rectangular waveguides under analogous conditions (with the load applied along the center line) indicated that the rectangular waveguide has lower resistance to compression under a linear load of 12.5 kg. The latter confirms the strength of the shape of the corrugated elliptical waveguide.

The acceptable load along the long axis for the E48 waveguide is 36.5 kg, and 31 kg for the E75, with acceptable short-axis deformation of 0.04 mm.

The above experiments to determine the acceptable loads as a function of the direction of application (short or long axis) were conducted on waveguide specimens 100 mm long.

Since under actual operating conditions elliptical waveguides are held at a slight positive internal gas pressure (nitrogen or "dry" air), in order to avoid condensation of moisture on the inside surface of the waveguide experiments were conducted to determine the deformation of the waveguides for various amounts of positive pressure. It was found that in both types of waveguides only a change in the short axis as a function of the amount of internal pressure is noticeable. If we use 0.04 mm as the acceptable deformation of the short axis, the waveguide can withstand 2.75 atm over a long period, or 6 atm briefly. These values are 1.55 atm and 5 atm, respectively, for the E75 waveguide. The experiments also showed that the waveguide can withstand excess pressure of 10 atm for many hours without destruction, but the residual deformation of the short axis exceeds the acceptable value.

Elliptical waveguides are subject to bending under production and operating conditions. The waveguide undergoes bending forces when wound on the drum. When it is bent around the drum, the waveguide is compressed on the inside at the point of the bend and stretched on the outside. The amount of these deformations depends upon the cross section of the waveguide and the radius of the bend.

Experiments have shown [4] that when a waveguide is wound around a drum 1200 mm in diameter (maximum radius of curvature 600 mm), the deformation along the long axis of the ellipse for the E48 waveguide was 2.7%, and 1.75% for the E75. However, these numbers contradict the requirements that the necessary rigidity be maintained in the axial directions. It is necessary to make an optimal decision from the viewpoint of waveguide rigidity as well as its flexibility, which is facilitated by the appropriate choice of the corrugation depth and spacing. For example, with a deep corrugation in which the ratio of the equivalent outside diameter of the corrugated tube to the equivalent inside diameter of the tube was $\frac{\text{Д}_{\text{нар}}}{\text{Д}_{\text{вн}}} = 1.25$ [Translator's note: Russian $\text{Д}_{\text{нар}}$

denotes outside diameter; Russian $Д_{ВН}$ denotes inside diameter], the waveguide was highly bend-resistant, but not sufficiently resistant to stretching forces. With shallow corrugation, when $\frac{Д_{нар}}{Д_{ВН}}$ =1.05, the waveguide could not withstand bending. A ratio of $\frac{Д_{нар}}{Д_{ВН}}$ =1.12 was recognized optimal [5]. The flexibility of the waveguides was checked by rewinding the waveguide from one drum onto another drum of a particular diameter [3]. The supply drum was braked in doing this in order to create the necessary stretching force. The rewinding was done so that the waveguide was bent at one end in a "C" shape, and in an "S" shape on the other side. The number of rewinding cycles before damage occurs is four times greater for a "C"-shaped bend than for an "S"-shaped bend.

The corrugation parameters selected provided the required rigidity and flexibility for 600 "C" rewindings, or 150 "S" rewindings, without damage to the material.

X-ray pictures of the structure of the E75 waveguide material for a selected corrugation shape which had undergone 320 "S"-rewindings showed the presence of narrow, shapeless cracks in the valleys of the corrugation. Investigation of the waveguide after 150 "S" rewindings showed no cracks. The presence of deformations in the cross section of the waveguides was monitored by measuring the coefficient of reflection before and after the rewinding. The measurements indicated that the waveguides were suitable for use after the tests described above were made. Measurements of the coefficient of reflection of the elliptical waveguides developed by the Telefunken Company (E40-E120) indicated that the maximum coefficient of reflection is 0.05 for a line approximately 40 meters long, and that the mean coefficient of reflection does not exceed 0.03 [3]. The measurements indicated that the coefficient of reflection increases as the depth and spacing of the corrugation increases.

It follows from the published data that the spacing of the corrugation for the entire series of elliptical waveguides varies between 6 and 12 mm.

The Andre Corporation (U.S.) produces flexible elliptical waveguides for the 3700-13,200 MHz band with a mean standing wave ratio of 1.05-1.06, with occasional overshoot reaching 1.15-1.20 [6].

Based on research done on the electrical and mechanical characteristics of their series of elliptical corrugated waveguides, the Telefunken Company guarantees the following·

1. Attenuation values close to those of rectangular waveguides in the corresponding frequency ranges.

2. Average reflectivity measured in an elliptical waveguide 40 meters long along with its adapters of 0.03-0.05 (depending upon waveguide brand), with occasional overshoot of up to 0.07-0.1.

3. Operation on mobile radio devices using a drum at least 1200 mm in diameter with no more than 300 rewinding operations.

4. Stationary operation in radio devices with a minimum radius of curvature (for one bend) in the electrical plane of 300-400 mm.

5. Maximum acceptable amount of stretching force of 100 kg.

6. Maximum acceptable linear distributed load acting along the axes of the ellipse of 10 kg/cm.

7. Acceptable internal operating pressure of 1500 g/cm^2.

The data on elliptical waveguides provided in messages and catalogs do not make it possible to establish precise geometric relationships for the dimensions of their cavity (for the long and short axes of the ellipse), which would make it possible to determine the acceptable operating frequency bands most precisely for individual brands of waveguides. However, based on the dimensions of the E48 and E75 waveguides, as well as the average axis lengths for E84 and E100 waveguides plus the outside dimensions of all types of waveguides, the internal dimensions for all types of E-series waveguides can be determined accurately enough for a preliminary estimate. Based on general theoretical premises, these dimensions can be used to obtain the acceptable working bands of individual brands of waveguides and the losses occurring therein as compared with standard rectangular waveguides.

Based on these conditions, the following internal cavity dimensions and basic geometric characteristics of the ellipse cross section should be used for the E-series waveguides. These dimensions are presented in Table 3.

As can be seen from the table, eccentricity of the order of 0.75-0.85 is characteristic for E-series waveguides (developed by the Telefunken Company).

In order to estimate the maximum operating frequencies and the range covered, we note, as is accepted in international practice, the lowest operating frequency for an elliptical waveguide must be approximately 1.2 of the critical frequency (frequency at which even oscillations of type ${}_cH_{11}$ occur), and the upper frequency must be correspondingly 0.95 of the maximum frequency) frequency at which even oscillations of type ${}_cE_{01}$ or odd ${}_sH_{11}$ occur).

The elliptical waveguide in this case is a single-wave transmission line operating at a wavelength of ${}_cH_{11}$. The general solutions for the transverse-electrical and transverse-magnetic field components are expressed through Mathieu's function [1,7]. In order to determine the phase coefficient (critical wavelength), it is assumed that the tangential components of the electrical field become zero at the wall of the waveguide. This requirement leads to the condition that the corresponding Mathieu functions become zero.

Table 3

waveguide brand	Internal cavity long axis 2a, mm	 short axis 2b, mm	coefficient of compression	eccentricity
E40	62.5	34.2	0.547	0.837
E48	47.1	31 5	0 668	0.745
E62	41.6	23.9	0.575	0.821
E68	39.1	21.3	0.545	0.84
E75	33.1	19.5	0.589	0.809
E84	28.8	17.8	0.618	0.787
E100	26.6	15.6	0.586	0.81
E120	23.6	12.6	0.534	0.847

For a wave ${}_cH_{11}$

$$R'_{c1}({}_cp'_{11};\ u_a) = 0, \qquad (1)$$

and for a wave ${}_cE_{01}$

$$R_{c0}({}_cp_{01};\ u_a) = 0. \qquad (2)$$

In expressions (1) and (2)

$R'_{c1}({}_cP'_{11};\ u_a)$ is the derivative of a modified first-order Mathieu function;

$R_{c0}({}_cP_{01};\ u_a)$ is a modified zero-order Mathieu function;

${}_cp'_{11}$, ${}_cP'_{11}$, ${}_cP_{01}$ and ch $u_a = \frac{1}{e}$ are the first parametric roots of the Mathieu functions determined from conditions (1) and (2).

The critical wavelength is determined by the formula

$$(\lambda_{\text{к}})_{mn}=\frac{\pi a e}{\sqrt{p_{mn}}}, \qquad (3)$$

where e is the eccentricity of the internal cavity of the elliptical waveguide, a is one-half the long axis of the internal cavity of the waveguide, p_{mn} is the parametric root of the Mathieu function determined from equations (1) and (2), $(\lambda_k)_{mn}$ is the critical length of the E_{mn} or H_{mn} waves.

Figure 4 shows the characteristics of the ratio of the critical and limiting wavelengths to the length of the long axis of an elliptical waveguide as a function of eccentricity [7]. Based on these data and the data in Table 3, Table 4 shows the results of calculating the critical, limiting, upper and lower working frequency for series-E waveguides.

Table 4

Brand of elliptical waveguide	λ_k, mm	$\lambda_{\text{пред}}$, mm	f_k, MHz	$f_{\text{пред}}$, MHz	operating band, MHz	
					$f_{\text{н}}=1.2f_{\text{кр}}$	$f_{\text{в}}=0.95f_{\text{пред}}$
E40	104.5	56.4	2872	5410	3446	5141
E48	79.3	47.4	3783	6328	4540	6012
E62	70.0	38.0	4289	7901	5147	7705
E68	65.6	34.5	4574	8686	5489	8251
E75	55.5	30.9	5402	9706	6482	9220
E84	48.2	27.8	6219	10810	7469	10270
E100	44.7	24.8	6714	12106	8057	11501
E120	36.6	20.6	8194	14598	9833	13808

[Translator's Note: The subscripts пред , н , кр and в above indicate limiting, lower, critical and upper, respectively.]

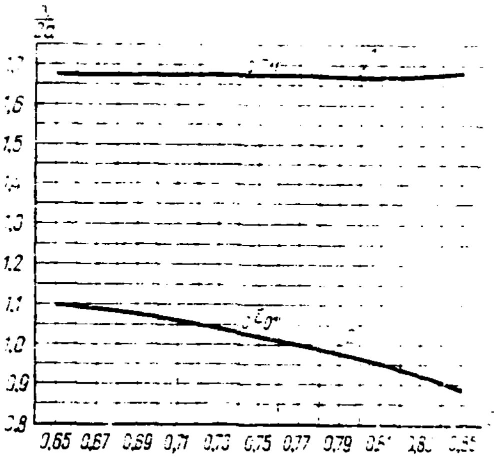

Fig. 4.

Key: 1 -- to determine critical wavelength in elliptical waveguide,
2 -- to determine limiting wavelength.

Figure 5 shows a diagram of the coverage of the 3000-15,000 MHz frequency range series-E waveguides and the corresponding series-R rectangular waveguides. The critical wavelength in the rectangular waveguides is taken to be 2 в (в -- size of wide wall), while the limiting wavelength is taken as в (if the ratio of the wide wall to the narrow wall is equal to or greater than 2). The lowest frequency in the operating band $f_{\text{Н}}$ =1.25 $f_{\text{К}}$, while the top frequency $f_{\text{В}}$ =0.95 $f_{\text{пред}}$. It is apparent from the figure that frequency coverage of elliptical waveguides is satisfactory, comprising more than 500 MHz for series E.

The frequency range coverage of rectangular waveguides within the working band (ratio of top frequency to bottom frequency in working band) is 1.52. For elliptical waveguides with eccentricity of 0.7 and 0.8 this value is slightly less, equalling 1.25 and 1.40, respectively. It should be noted that in a round cylindrical waveguide the ratio of the top and bottom frequencies of the working band is still smaller, amounting to only 1.155, i.e., the round waveguide has narrower bandwidth. (For cylindrical waveguides values of $f_{\text{И}}$ =1.1 f_k, $f_{\text{Г}}$ = =0.975 $f_{\text{пред}}$ are used.)

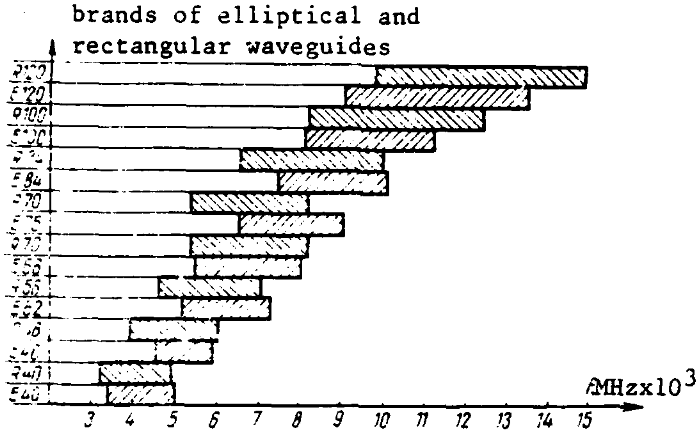

Fig. 5.

Figure 6 shows the amounts of losses for series-E and -R waveguides according to data from the Telefunken Company. Determination of the parameters of the internal cavity and their relationship for elliptical and rectangular waveguides, as well as the relationship between the losses in these waveguides, allow the following conclusions:

1. With a rectangular and elliptical waveguide perimeter ratio of approximately 1.12 (perimeter ratios for R_{40}/E_{40}; R_{84}/E_{84}; R_{48}/E_{48}), loss ratios of approximately 1, 0.95 and 0.88, respectively, are observed. The respective eccentricity is 0.84, 0.79 and 0.75. Thus, if the perimeter of a rectangular waveguide is approximately 10% larger than that of an elliptical waveguide, their losses are approximately the same (ellipse eccentricity E=0.84). The losses in an elliptical waveguide for the case in question will be 5-10% greater when the eccentricity is reduced to 0.79-0.75.

2. If the ratio of the perimeters of elliptical and rectangular waveguides is approximately 1 (for R_{100}/E_{100}), with an ellipse eccentricity of 0.81 the losses in a brand E100 waveguide are approximately 30% lower than in a corresponding rectangular waveguide.

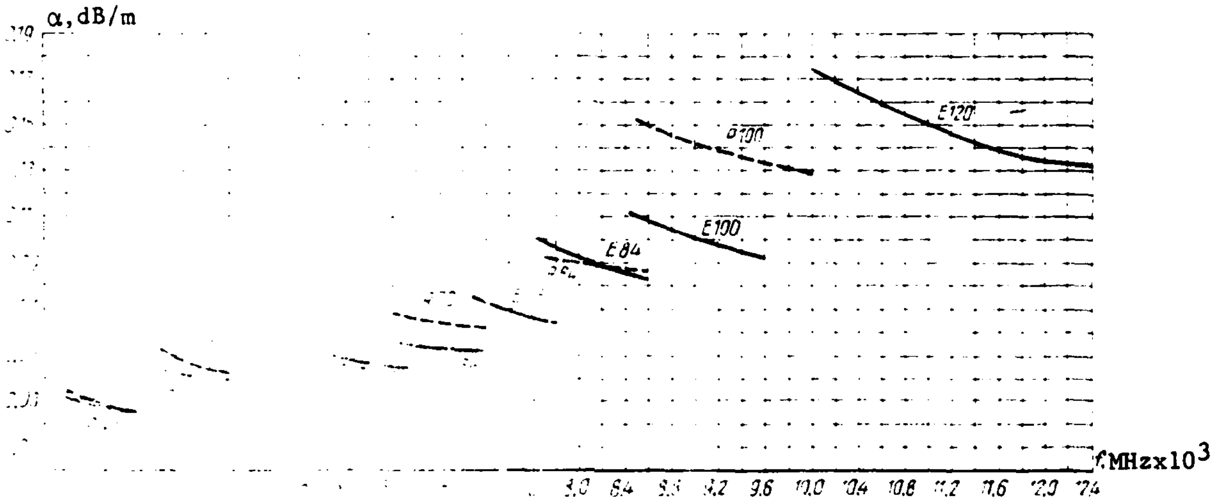

Fig. 6.

The materials presented above concerning the amount of attenuation, frequency range covered, and physical-mechanical characteristics of elliptical waveguides confirm the promise of their utilization in the centimeter band for both stationary and mobile radio installations.

LITERATURE

1. L. J. Chu. «Электромагнитные волны в эллиптических полых трубах из металла». «Journal of Applied Physics. 9, 583, 1938.

2. W. Krank и E. Schüttlöffel. «Гофрированный гибкий волновод с эллиптическим поперечным сечением для сверхвысоких частот. Telefunken Zeitung 35 (июнь, 1962), тетрадь 136, стр. 112—116.

3. W. Krank и E. Schüttlöffel. «Гибкий эллиптический фидер с малыми потерями». Nachrichtentechnische Zeitschrift, 18 (октябрь, 1965), № 10, стр. 607—615.

4. G. Herberts. «Механические характеристики гибкого волновода некруглого сечения». Nachrichtentechnische Zeitschrift 18 (ноябрь, 1965) № 11, стр. 637—642.

5. G. Möhring. «Изготовление гофрированных кабельных оболочек круглого и эллиптического сечения, стойких к деформациям» Nachrichtentechnische Zeitschrift (декабрь, 1965), № 12.

6. «Эллиптический волновод экономит время, снижает стоимость». Communications news, март, 1966.

7. G. Piefke. «Характеристика передачи эллиптического волновода». Archiv der electrische Übertragung. 18 (1964). № 4, 255—267

BEAM ROCKING IN MIKAELYAN LENS

Ye.G. Zelkin, V.A. Andreyev

This article considers the question of beam rocking in a nonuniform Mikaelyan lens, and analyzes the phase of the field and maximum amount of distortion of the phase front within the aperture of that lens

INTRODUCTION

This article examines the question of the possibility of using a nonuniform Mikaelyan lens in antenna devices which require beam rocking.

In principle, a Mikaelyan lens is a focusing non-aplanatic system. However, we know that any optical system permits practically undistorted beam rocking within some limited angular sector with the radiation source moving along the focal surface. Such systems include, for example, parabolic reflector antennas.

The field phase and maximum phase front distortion in the aperture of a Mikaelyan lens are calculated below, as is the angle of deviation of the beam from the axis when the radiation source moves out-of-focus along the y coordinate

(Fig. 1), in order to determine the sector of practically undistorted beam rocking

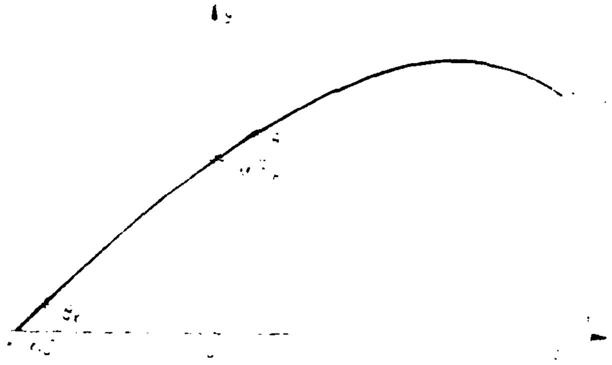

Fig. 1.

A plane problem is considered, i.e., *it is assumed that* the index of refraction of the lens is a function only of the y coordinate and is independent of the x and z coordinates:

$$n=f(y).$$

The radiation source in such a lens must be a linear feeder.

Calculation of Field Phase Within Lens Aperture

As we know [1], the curve of the beam propagation in a Mikaelyan lens is described by the following equation:

$$\cos\frac{\pi x}{2b}=\cot\Theta_x \sinh\frac{\pi y}{2b}, \tag{1}$$

where Θ_x is the angle between the x axis and the tangent to the beam at the point of intersection of the beam and the ordinate, b is the thickness of the lens.

The index of refraction in a Mikaelyan lens changes according to the principle

$$n(y)=\frac{n_0}{\cosh\frac{\pi y}{2b}}, \qquad (2)$$

where n_0 is the index of refraction at the axis of the lens.

Since the index of refraction is independent of the x coordinate, we shall use the following equation instead of expression (1):

$$\sin\frac{\pi(X-x)}{2b}=\cot\Theta_x \sinh\frac{\pi y}{2b}. \qquad (3)$$

We are easily convinced that this equation covers all cases of beam propagation in a medium with these parameters. Furthermore, the distances from the point at which the beam trajectory intersects the x axis to the coordinate origin are determined by the quantity X, and the angle between the tangent to the beam trajectory and the x axis is Θ_x.

We shall position the lens with respect to the coordinate system as is shown in Fig. 1, i.e., so that the lens aperture coincides with the x=b plane, and the feeder is located at the point M(0;R).

For further analysis, we shall consider the bundle of beams exiting the feeder to be a bundle of curves passing through point M (Fig. 1).

The optical length of the path along the beam from the point (0;R), where the feeder is located, to the point (b;y_2) in the aperture of the lens can be found from the following expression

$$S=\int_{t_1}^{t_2} n(y)\sqrt{\left(\frac{d(X-x)}{dt}\right)^2-\left(\frac{dy}{dt}\right)^2}\,dt \qquad (4)$$

for the case in which the curve is written in parametric form. Here $t_1(0;R)$

and $t_2(b;y_2)$ are the points on the trajectory of the beam in question, n(y) is the index of refraction, which varies according to (2). We shall introduce the designation $a = \cot \Theta_x$ to equation (3)

$$\sin\frac{\pi(X-x)}{2b} = a\sinh\frac{\pi y}{2b} \tag{5}$$

and write this expression in parametric form:

$$\sin\frac{\pi(X-x)}{2b} = t;\ a\sinh\frac{\pi y}{2b} = t. \tag{6}$$

$$\text{Hence}\quad (X-x) = \frac{2b}{\pi}\arcsin t;\quad y = \frac{2b}{\pi}\operatorname{arcsinh}\frac{t}{a} \tag{7}$$

$$\text{and}\ \frac{d(X-x)}{dt} = \frac{2b}{\pi}\frac{1}{\sqrt{1-t^2}};\quad \frac{dy}{dt} = \frac{2b}{a\pi}\frac{1}{\sqrt{1+\left(\frac{t}{a}\right)^2}} \tag{8}$$

Substituting the value for y from (7) in (2), we obtain

$$n(y) = \frac{n_0}{\sqrt{1+\left(\frac{t}{a}\right)^2}}. \tag{9}$$

Substituting the values of n(y), dy/dt and d(X-x)/dt in expression (4),

$$S = \int_{t_1}^{t_2}\frac{n_0}{\sqrt{1+\left(\frac{t}{a}\right)^2}}\sqrt{\left(\frac{2b}{\pi}\frac{1}{\sqrt{1-t^2}}\right)^2+\left(\frac{2b}{a\pi}\frac{1}{\sqrt{1+\left(\frac{t}{a}\right)^2}}\right)^2} \tag{10}$$

After some simple transformations

$$S = n_0\frac{2b}{\pi}a\sqrt{a^2+1}\int_{t_1}^{t_2}\frac{dt}{(a^2+t^2)\sqrt{1-t^2}} \tag{11}$$

It is easy to compute the latter integral. Substituting t= sin α, we obtain [2]

$$\int_{t_1}^{t_2} \frac{dt}{(a^2 + t^2)\sqrt{1-t^2}} = \int_{\alpha_1}^{\alpha_2} \frac{\cos\alpha \, d\alpha}{(a^2 + \sin^2\alpha)\cos\alpha} = \int_{\alpha_1}^{\alpha_2} \frac{d\alpha}{a^2 + \sin^2\alpha} =$$

$$= \frac{\tan\left(\frac{\sqrt{a^2+1}}{a}\operatorname{tg}\alpha\right)}{a\sqrt{a^2+1}}\Bigg|_{\alpha_1}^{\alpha_2}.$$

$$S = n_0 \frac{2b}{\pi}\left[\arctan\left(\frac{\sqrt{a^2+1}}{a}\operatorname{tg}\alpha_2\right) - \arctan\left(\frac{\sqrt{a^2+1}}{a}\tan_{\alpha_1}\right)\right]. \tag{12}$$

Since $t = \sin\alpha = \sin\frac{\pi(X-x)}{2b}$,

TO $\alpha = \frac{\pi(X-x)}{2b} + 2n\pi$

and (12) can be written as

$$S = n_0 \frac{2b}{\pi}\arctan\left\{\frac{\sqrt{a^2+1}\left[\tan\frac{\pi(X-b)}{2b} + \tan\frac{\pi X}{2b}\right]}{a\left[1-\left(1+\frac{1}{a^2}\right)\tan\frac{\pi(X-b)}{2b}\tan\frac{\pi X}{2b}\right]}\right\}. \tag{13}$$

But

$$\tan\frac{\pi(x-b)}{2b} = -\cot\frac{\pi X}{2b},$$

whence, in turn, it follows that

$$\tan\frac{\pi(X-b)}{2b}\tan\frac{\pi X}{2b} = -1, \tag{14}$$

$$\tan\frac{\pi(X-b)}{2b} + \tan\frac{\pi X}{2b} = -\frac{1}{\sin\frac{\pi X}{2b}\cos\frac{\pi X}{2b}}. \tag{15}$$

Substituting (14) and (15) in (13), we obtain

$$S = n_0 \frac{2b}{\pi}\operatorname{arc\,tan}\frac{a\sqrt{a^2+1}}{\sin\frac{\pi X}{2b}\cos\frac{\pi X}{2b}}. \tag{16}$$

Expression (16) yields the value of the electrical length of the curve with parameters a and X on the segment between the planes x=0 and x=b.

We now eliminate the parameter X from (16). Since

$$\sin\frac{\pi X}{2b}=a\sinh\frac{\pi R}{2b}, \tag{17}$$

$$S=n_0\frac{2b}{\pi}\arctan\frac{\sqrt{a^2+1}}{\sinh\frac{\pi R}{2b}\sqrt{1-a^2\sinh^2\frac{\pi R}{2b}}} \tag{18}$$

Here $a=\cot\Theta_x$ is the parameter which defines the beam in question within the bundle of beams passing through the point M; (0;R) is the locus of the feeder.

Varying Θ_x, and correspondingly parameter a, within some selected range of values, we can obtain the electrical length of the path along any beam between the planes x=0 and x=b.

However, for practical purposes it is of interest to calculate the electrical length of the path along the beam in the sector bounded by the aforementioned planes as a function of the parameter y_2 -- the distance from the axis of the lens to the point at which the beam in question intersects the lens aperture. Let us make the following transformations as well.

By analogy with (17), we have the following for the point with the coordinates $(b;y_2)$

$$\sin\frac{\pi(X-b)}{2b}=a\sinh\frac{\pi y_2}{2b}, \tag{19}$$

where a is naturally the same parameter as in (17) for the same value of X. From (17)

$$x = \frac{2b}{\pi} \arcsin\left(a \sinh \frac{\pi R}{2b}\right) \tag{20}$$

Substituting (20) in (19),

$$\sin \frac{\pi}{2b}\left[\frac{2b}{\pi} \arcsin\left(a \sinh \frac{\pi R}{2b}\right) - b\right] = a \sinh \frac{\pi y_2}{2b}$$

whence it follows that

$$1 - a^2 \sinh^2 \frac{\pi R}{2b} = a^2 \sinh^2 \frac{\pi y_2}{2b}$$

then

$$a = \sqrt{\frac{1}{\sinh^2 \frac{\pi R}{2b} + \sinh^2 \frac{\pi y_2}{2b}}} \tag{21}$$

Substituting (21) in (18), we obtain the following convenient expression for determining the optical length of the path along the beam from the point (0;R) -- the point at which the feeder is located -- to the point $(b;y_2)$ -- the point on the aperture of the lens -- as a function of the parameter y_2:

$$S = n_0 \frac{2b}{\pi} \arctan \sqrt{\frac{1 - v^2 - u^2}{v^2 u^2}}$$

where

$$v = \sinh \frac{\pi R}{2b}; \quad u = \sinh \frac{\pi y_2}{2b}. \tag{22}$$

It should be noted that we are not mainly interested in the length of the optical path, but rather its deviation from average value, e.g., the value of the optical path along the beam which intersects the lens aperture at the point (b;0). Substituting $y_2 = 0$ in (22), we are easily convinced that the length of the optical path along the beam in question

$$S_0 = n_0 b. \tag{23}$$

Incidentally, we note that the tangent to that beam at the point (0;R) will be parallel to the x axis.

We shall designate ΔS the deviation of the optical length of the path of the beam from the value S_0; it is the case that

$$\Delta S = S - S_0 .$$

Substituting the values from (22) and (23) in (24), we obtain

$$\Delta S = n_0 \frac{2b}{\pi} \left(\arctan \sqrt{\frac{1 + \rho^2 + u^2}{\rho^2 u^2}} - \frac{\pi}{2} \right),$$

whence it follows that

$$\Delta S = n_0 \frac{2b}{\pi} \arctan \sqrt{\frac{\rho^2 u^2}{1 + \rho^2 + u^2}} . \qquad (25)$$

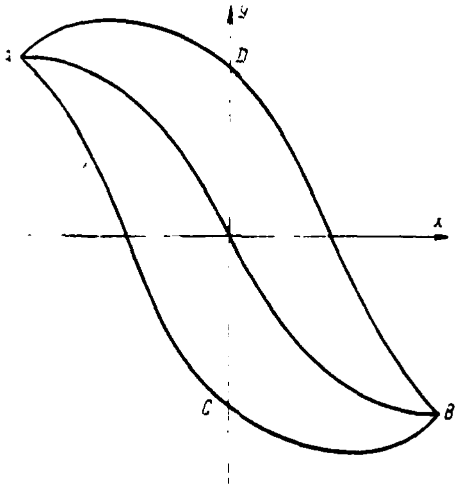

Fig. 2.

It is easy to show that the deviation of the wave front from being in phase will be antisymmetrical with respect to the center of the aperture. It is apparent from Fig. 2 that all beams originating at point A intersect at point B, which is located antisymmetrically to point A, with respect to the lens aperture. Consequently, the optical lengths of all of the paths along the beams from point A to point B have the same value, namely $2n_0b$. It follows from this that the sum of the optical paths from point a to the aperture of the lens along the two beams which intersect the aperture at points equidistant from the X axis, e.g., D and C, is also $2n_0b$. It is the case that

$$S_{AD}+S_{DB}=2n_0b$$

and $$S_{DB}=S_{AC};$$

consequently, $$S_{AD}+S_{AC}=2n_0b.$$

The latter expression shows that the curve of the deviation of the optical paths as a function of y_2 will be antisymmetrical with respect to the x axis.

In some practical cases, it may be inconvenient to have the value n_0 in expression (28), since it may be that the phase distortions in the lens aperture are being calculated for the purpose of selecting n_0 based on conditions of minimum distortions.

We know from [1] that

$$n_0=n_r \cosh \frac{\pi R_{\text{л}}}{2b}. \tag{26}$$

where n_r is the index of refraction at the point $y=R_{\text{л}}$, $2R_{\text{л}}$ is the size of the lens aperture [Translator's Note: The subscript л denotes "lens"].

If we set $x=b$ and $y=R_{\text{л}}$ in expression (3), then

$$\tan \Theta_{max}=\sinh \frac{\pi R_{\text{л}}}{2b}. \tag{27}$$

where Θ_{max} is the aperture angle of the radiator if the letter is located at the focus of the lens.

It follows from (27) that

$$\frac{R_{\pi}}{b} \quad \frac{2}{\pi}\,\mathrm{arcsinh}(\tan\Theta_{max}). \qquad (28)$$

We substitute (28) in (26), and assuming $n_r=1$, we obtain

$$n_0=\cosh\,\mathrm{arcsinh}(\tan\Theta_{max})=\frac{1}{\cos\Theta_{max}} \qquad (29)$$

We substitute the value obtained for n_0 in (25). Then we finally obtain

$$\Delta S=\frac{2b}{\pi\cos\Theta_{max}}\arctan\sqrt{\frac{\text{[illegible]}\,u^2}{1\,\text{[illegible]}}}, \qquad (30)$$

where

$$\eta=\sinh\frac{\pi R}{2b};\ u=\sinh\frac{\pi y}{2b}.$$

Formula (30) was used to calculate the value of ΔS for various values of R -- the distance between the feeder and the focus of the lens. The results of the calculation are shown in Fig. 3 as a series of curves. It is apparent from the figure that when the value of R increases, the slope of the phase front increases and its distortion grows as well.

PHASE DISTORTIONS IN LENS APERTURE

Let us estimate the phase nonlinearity in the lens aperture. In order to do this, we expand (30) into a series with respect to y. Limiting ourselves to the first three terms of the expansion, we obtain

$$S=\frac{\eta}{\cos\Theta_{max}\sqrt{1+\eta^2}}\left[y-\frac{(2-\eta^2)\pi^2}{24(1-\eta)b^2}y^3+\frac{(25\eta^4-28\eta^2+16)\pi^4}{1920b^4}y^5\right]. \qquad (31)$$

Using the least-squares method, we find the slope of a plane front equivalent to the front in question. In order to do this, we define the coefficient α which characterizes the slope of the equivalent plane front using the expression

$$\int_{-R_c}^{+R_c}\left[\frac{\partial}{\partial \alpha}(\Delta S-\alpha y)^2\right]dy=0, \qquad (32)$$

where R_c is half the utilized lens aperture, which is less than or equal to $R_Л$ -- half the calculated lens diameter.

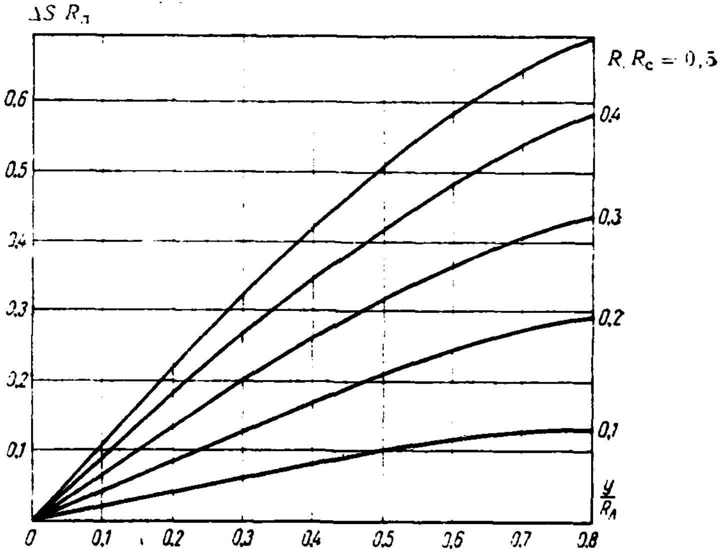

Fig. 3.

We note that in speaking of using part of the aperture of a lens with radius R_c, we are of course assuming that a lens with diameter $2R_c$ is the actual implemented part of the calculated lens with diameter $2R_Л$, where the dimension $R_Л$ is the distance from the axis of the lens to the point at which n=1, and R_c is selected on the basis of the tolerable distortion for the case in question.

Accordingly, the aperture angle of the feeder of a lens with $2R_c$ will be smaller than the angle Θ_{max} and must be calculated separately for each value R_c.

Substituting (31) in (32) and performing the appropriate calculations, we obtain

$$\alpha=\tan\psi=\frac{\vartheta}{\cos\theta_{\max}\sqrt{1+\vartheta^2}}\left(1-\frac{\pi^2(2+\vartheta^2)}{40(1+\vartheta^2)}\frac{R_c^2}{b^2}\right). \tag{33}$$

where ψ is the angle of inclination of the equivalent plane front.

Substituting the value of ϑ in (33) in accordance with (22), in solving (33) for ψ, we obtain the following final formula for determining the angle of deviation of the directivity pattern of the lens antenna

$$\psi=\operatorname{arctan}\frac{\sinh\frac{\pi R}{2b}}{\cos\theta_{\max}\sqrt{1+\sinh^2\frac{\pi R}{2b}}}\left(1-\frac{\pi^2\left(2+\sinh^2\frac{\pi R}{2b}\right)R_c^2}{40\left(1+\sinh^2\frac{\pi R}{2b}\right)b^2}\right) \tag{34}$$

where R -- distance between feeder and focus of lens;

Θ_{max} -- aperture angle of total-lens feeder;

b -- lens thickness;

R_c -- radius of utilized portion of lens.

The difference between the optical paths between the actual phase front and its equivalent plane front at the distance of R_c from the x axis is

$$\Delta S_{\text{кр}}=\Delta S_{R_c}-\tan\psi\, R_c. \tag{35}$$

Substituting the values of ΔS and tan ψ in (35) and limiting ourselves to terms below y^5, we obtain the following expression for the quantity ΔS_{KP} :

$$\Delta S_{\text{кр}}=\frac{\pi^2\vartheta(2+\vartheta^2)}{60b^2\cos\Theta_{\text{макс}}\sqrt{(1+\vartheta^2)^3}}R_c^3. \tag{36}$$

Formula (36) can also be written in the following form:

$$\frac{\Delta S_{KP}}{\lambda} = \frac{R_c}{\lambda}\left(\frac{R_c}{b}\right)^2 \frac{\pi^2 \vartheta (2+\vartheta^2)}{60\cos\theta_{\max}\sqrt{(1+\vartheta^2)^3}} \tag{37}$$

This notation is more convenient, since the quantity R_c/b is a determining parameter of the lens, while the quantity $\Delta S_{KP}/\lambda$ is a determining parameter for the distortions in the aperture in fractions of a wavelength. Substituting the value of ϑ in (37), we obtain the following final expression for determining the quantity $\Delta S_{KP}/\lambda$:

$$\frac{\Delta S_{KP}}{\lambda} = \frac{R_c}{\lambda}\left(\frac{R_c}{b}\right)^2 \frac{\pi^2 \sinh\frac{\pi R}{2b}\left(2+\sinh^2\frac{\pi R}{2b}\right)}{60\cos\theta_{\max}\sqrt{\left(1+\sinh^2\frac{\pi R}{2b}\right)^3}}. \tag{38}$$

Formula (34) and (38) are basic for calculating phase distortions in the lens aperture during beam rocking. Formula (34) can be used to determine the angle of deviation of the directivity pattern, while formula (38) can be used to find the phase front distortions at the edge of the lens aperture.

It should be considered that these formulas produce correct results only for $R_c<0.6$, since only for these values are the quantities R_c valid in the expansion we have done.

Formulas (34) and (38) were used to calculate the values of $\Delta S_{KP}/\lambda$ and ψ as functions of the distance from the feeder to the axis of the lens for two values of R_c. The calculation was done for a lens with the following calculated parameters[1]:

$n_0=2$ -- index of refraction on lens axis;
$n_r=1$ -- index of refraction at edge of lens;

---

[1] The values of b, $R_Л$ and R_c are given in relative units.

$b=1.2$ -- lens thickness;

$2R_{Л}=2$ -- lens diameter;

Θ_{max} -- aperture angle of feeder for lens with diameter of 2;

$R_{c1}=0.5$ -- utilized portion of aperture;

$R_{c2}=2.6$ -- utilized portion of aperture.

The results of the calculation are shown in Figs. 4, 5 and 6 as a group of curves.

Figure 4 shows the angle of deviation of the beam as a function of the distance of the radiator from focus.

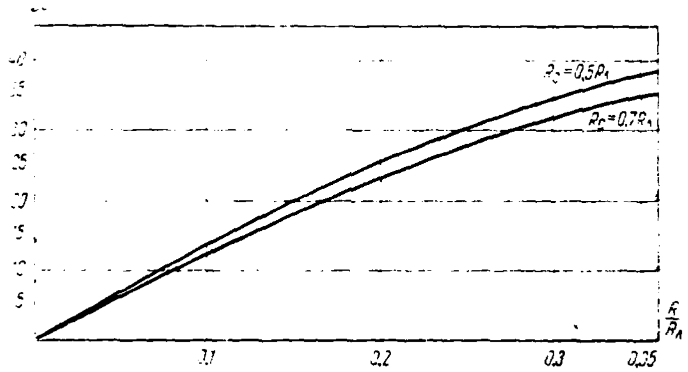

Fig. 4.

Figures 5 and 6 show the amounts of phase distortions in the lens aperture with various angles of deviation and various relative aperture dimensions in beam wavelength. In Fig. 5 $R_{c1}=0.5$; in Fig. 6 $R_{c2}=0.6$. The curves are constructed only for $S_{KP} \leq \lambda/4$. As can be seen from Figs. 5 and 6, the Mikaelyan lens allows the beam to be rocked over a fairly wide sector with practically acceptable phase front distortions.

It is easy to note that if we limit ourselves to distortions not exceeding λ/8, the beam can deviate by several directivity pattern widths.

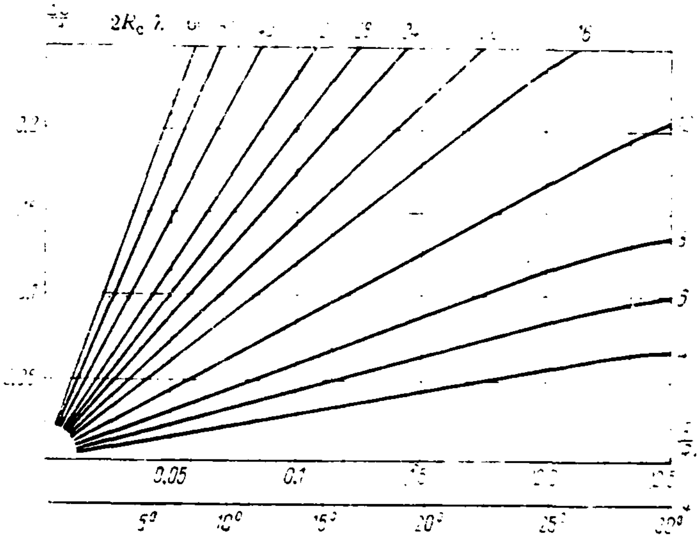

Fig. 5.

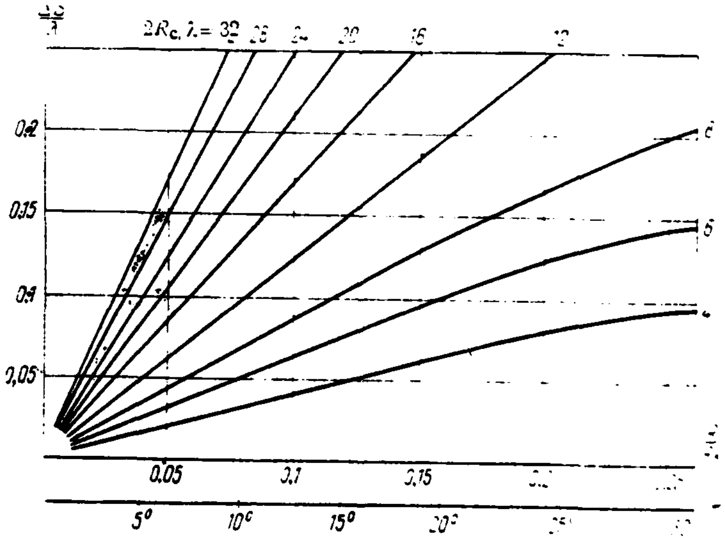

Fig. 6.

LITERATURE

1. [illegible] Н. Ф[illegible] [illegible] Б[illegible] [illegible]
Часть II, изд. ВВИА им. Жуковского, [illegible].
2. И. С. Градштейн и И. М. Рыжик. Таблицы [illegible]
рядов и произведений. Госиздат Физико-математической литературы, М., [illegible]

SYNTHESIS OF RADIATOR CROSS-COUPLING COMPENSATION CIRCUIT IN PHASED ANTENNA ARRAY

O.G. Vendik, L.V. Ryzhkova

The general method is proposed for synthesizing a cross-coupling compensation circuit in a phased array. If each isolated radiator is matched, in order to determine the parameters of the compensation circuit it is sufficient to know only the normalized mutual impedances of the radiators. A cross-coupling compensation circuit for two antennas is calculated as an example.

INTRODUCTION

As we know, a significant cross-coupling effect between individual radiators is observed in phased antenna arrays consisting of a large number of omnidirectional radiators placed close together.

The antenna characteristics are influenced by cross-coupling in three basic directions:

1. The matching between each individual radiator and the feeder line is disrupted during operation in the system, which reduces the antenna gain.

2. Energy leakage into adjacent channels can change the amplitude-phase distribution assigned by the control system significantly, and consequently reduce the beam-setting accuracy and increase the side lobe level.

3. Scattering by each aperture of the energy reaching it from the other apertures due to cross-coupling, sometimes called re-radiation, also changes the directivity pattern of the antenna

We can state with certainty that reducing the harmful influence of cross-coupling between radiators on the antenna parameters is now one of the most urgent problems for the developers of phased arrays.

One method which is extremely interesting in this connection is that proposed in 1963 by Hannan [1] for matching the impedances of phased arrays in a wide scanning angle based on creating artificial coupling between the radiators which compensate for reflections occurring due to cross-coupling in the system. That article cites experimental data which provide evidence that the use of the proposed matching method reduces energy losses in the system significantly.

However, introducing artificial coupling between the feeder lines which compensates for the coupling which exists between the radiating apertures in an array makes it possible to reduce mismatch between the radiators and their own feeders as well as to achieve the individual channel decoupling which is necessary to independent control of each radiator.

A general method for synthesizing a compensating circuit is proposed; special attention will be devoted to compensating for waves which leak into adjacent channels, i.e., those which disturb the amplitude-phase distribution assigned by the control system.

SETTING UP COMPENSATION EQUATION

We shall consider an antenna system consisting of N radiating elements. Such an antenna can be represented as a multi-port network [2] with N pairs of input terminals and an infinite number of output terminals (corresponding to representing the antenna field as a spherical wave sum). However, if we ignore the directivity pattern formed by the antenna and consider only what happens at the input of such a system, it is more convenient to represent the system as a system of N connected waveguides working into unmatched loads. When this is done, we can ignore all of the output terminals and consider the antenna as a multi-port network having a total of N pairs of terminals. Leakage of energy from one channel to another, as well as reflection of the energy at the system inputs, are fully defined by the impedance matrix of the aperture system

$$Z_A = \begin{bmatrix} z_{11}, & z_{12} & \dots & z_{1N} \\ z_{21} & & \cdot & \vdots \\ \vdots & & & \vdots \\ z_{N1} & & & z_{NN} \end{bmatrix}.$$

where z_{ii} is the inherent radiation impedance of the element, z_{ik} is the cross-impedance of two radiators.

If the elements in the impedance matrix are measured or calculated [3], the following formula can be used to define the scattering matrix of the multi-port network:

$$S_A=(Z_A-1)(Z_A+1)^{-1}, \qquad (1)$$

where 1 is an Nth-order identity matrix. The matrix S_A, as usual, interconnects the column vectors of the incident and reflected waves

$$(b_A)=S_A(a_A). \qquad (2)$$

It can be shown that if a system is mutual and the radiators in the system are alike, the scattering matrix of the array system appears as:

$$S_A = \begin{bmatrix} s_1 & s_2 & \dots & s_N \\ s_2 & & & \vdots \\ \vdots & & & \vdots \\ s_N & & & s_1 \end{bmatrix}.$$

Now let the cross-coupling compensation circuit be a multi-port waveguide network connected between the controlled system and the system of radiating apertures. Obviously, this multi-port must have N pairs of input and N pairs of output terminals (Fig. 1).

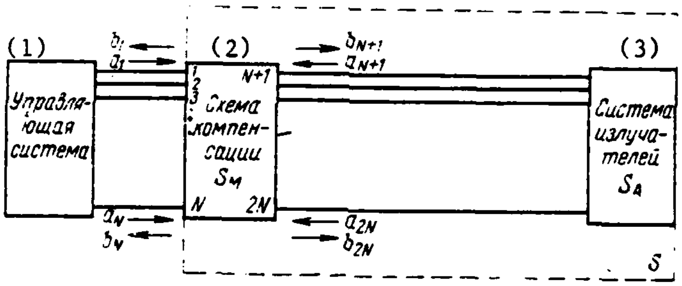

Fig. 1.

Key: (1) control system; (2) compensation circuit; (3) radiator system.

The systems of incident and reflected waves at the terminals of the compensation circuit are connected by the scattering matrix S_M:

$$\begin{pmatrix} b_1 \\ b_2 \\ \vdots \\ b_{2N} \end{pmatrix} = S_M \begin{pmatrix} a_1 \\ a_2 \\ \vdots \\ a_{2N} \end{pmatrix}. \qquad (3)$$

It is easy to see that the waves reaching the output terminals of the compensation circuit are reflected from the aperture system, and conversely, i.e.,

$$a_N = \begin{pmatrix} b_{N+1} \\ b_{N+2} \\ \vdots \\ b_{2N} \end{pmatrix}; \quad b_N = \begin{pmatrix} a_{N+1} \\ a_{N+2} \\ \vdots \\ a_{2N} \end{pmatrix}. \tag{4}$$

If we substitute equation (4) in (2), we obtain the following connection between the incident and reflected waves at the output terminals of the compensation circuit:

$$\begin{pmatrix} a_{N+1} \\ a_{N+2} \\ \vdots \\ a_{2N} \end{pmatrix} = S_N \begin{pmatrix} b_{N+1} \\ b_{N+2} \\ \vdots \\ b_{2N} \end{pmatrix}. \tag{5}$$

Let us now consider a new multi-port representing a cascaded connection of a compensation circuit and system of apertures. Its terminals coincide with the first N pairs of terminals of the compensation circuit, and the scattering matrix connects the incident and reflected waves at the input terminals of the compensation circuit.

$$\begin{pmatrix} b_1 \\ b_2 \\ \vdots \\ b_N \end{pmatrix} = S \begin{pmatrix} a_1 \\ a_2 \\ \vdots \\ a_N \end{pmatrix}. \tag{6}$$

Simultaneous solution of systems of equations (3) and (5) makes it possible to define the scattering matrix S of the multi-port network. In order to operate with matrices of the same order, we must do some transformations.

We divide the matrix S_M into four blocks:

$$S_M = \begin{vmatrix} S_{II} & S_{I\,II} \\ \hline S_{II\,I} & S_{II\,II} \end{vmatrix} .$$

In addition, we introduce the following notation:

$$\begin{pmatrix} a_1 \\ a_2 \\ \vdots \\ a_N \end{pmatrix} = a_I ; \quad \begin{pmatrix} b_1 \\ b_2 \\ \vdots \\ b_N \end{pmatrix} = b_I ; \quad \begin{pmatrix} a_{N+1} \\ a_{N+2} \\ \vdots \\ a_{2N} \end{pmatrix} = a_{II} ; \quad \begin{pmatrix} b_{N+1} \\ b_{N+2} \\ \vdots \\ b_{2N} \end{pmatrix} = b_{II} .$$

Then equation (3) appears as

$$b_I = S_{I\,I} a_I + S_{I\,II} a_{II} ; \tag{7}$$

$$b_{II} = S_{II\,I} a_I + S_{II\,II} a_{II} . \tag{8}$$

Instead of (5) and (6), we can write:

$$a_{II} = S_A b_{II} ; \tag{9}$$

$$b_I = S a_I . \tag{10}$$

Solving equations (7), (8) and (9) simultaneously, we obtain

$$b_I = S_{II} a_I - [S_{I\,II} (1 - S_A S_{II\,II})^{-1} S_A S_{II\,I}] a_I . \tag{11}$$

It follows from (10) and (11) that

$$S = S_{II} - S_{I\,II} (1 - S_A S_{II\,II})^{-1} S_A S_{II\,I} . \tag{12}$$

It is easy to show that all of the elements of the matrix $S_A S_{II\ II}$ are significantly less than unity; therefore, the matrix $(1-S_A S_{II\ II})$ is not always singular and consequently has an inverse. One exception is the case, of no practical interest, in which the system in question is severely mismatched.

We have thus obtained the sought connection between the incident and reflected waves at the input terminals of the compensation circuit under the condition that its output terminals are loaded to a system of coupled apertures.

As follows from the synthesis problem formulated above, the combined scattering matrix obtained for a system with cross-coupling compensation must be diagonal. This assertion allows us to setup the following compensation equations:

$$s_{ik}=0; \quad i \neq k; \quad i,\ k=1,\ 2\ \ldots\ N, \tag{13}$$

where s_{ik} are elements of matrix S.

If the primary task of the investigation is not to obtain substantial channel decoupling, i.e., precise maintenance of the amplitude-phase distributions on the antenna assigned by the control devices, but rather to match each individual channel, it then follows, conversely, to zero the diagonal elements of the matrix S:

$$s_{ii}=0; \quad i=1,\ 2,\ \ldots\ N. \tag{14}$$

When this is done, the mismatch between each radiator and its feeder line occurring in the antenna array due to coupling between the radiators can be fully eliminated.

The solution to system of equations (13) with respect to the elements of matrix S_M defines the sought parameters of the compensation circuit with respect to the known values of the scattering matrix of the system of apertures S_A defined by equation (1) from the impedance matrix.

As will be shown below, under defined conditions the inherent radiation impedance of the elements can be ignored; then it is sufficient to know only the normalized mutual impedances of the radiators in order to determine the parameters of the compensation circuit.

DETERMINATION OF PARAMETERS OF COMPENSATION CIRCUIT FOR CROSS-COUPLING OF TWO RADIATORS

The problem of synthesizing a cross-coupling compensation circuit for two antennas is of interest in order to illustrate the general methodology presented above; it is also of independent practical value, e.g., in single-pulse systems. This problem can be formulated as follows: let it be required to determine the parameters of a waveguide circuit connecting the feeder line of two antennas such that the existing coupling between the radiating apertures is compensated.

Let there be a system of two antennas for which the elements of the impedance matrix are calculated or measured:

$$Z_A = \begin{vmatrix} z_{11} & z_{12} \\ z_{21} & z_{22} \end{vmatrix},$$

where

$$z_{KK} = \left.\frac{U_K}{I_K}\right|_{I_i=0},$$

$$z_{iK} = \left.\frac{U_i}{I_K}\right|_{I_i=0}$$

If the system is mutual ($z_{12}=z_{21}$) and the antennas are identical ($z_{11}=z_{22}$), then

$$Z_A = \begin{vmatrix} z_{11} & z_{12} \\ z_{12} & z_{11} \end{vmatrix}.$$

We use formula (1) to define the scattering matrix

$$S_A = \begin{vmatrix} \dfrac{z_{11}^2 - z_{12}^2 - 1}{(z_{11} - 1)^2 - z_{12}^2} & \dfrac{2z_{12}}{(z_{11} - 1)^2 - z_{12}^2} \\ \dfrac{2z_{12}}{(z_{11} - 1) - z_{12}^2} & \dfrac{z_{11}^2 - z_{12}^2 - 1}{(z_{11} - 1)^2 - z_{12}^2} \end{vmatrix}.$$

If the antennas were not coupled, the scattering matrix would appear as follows:

$$S'_A = \begin{vmatrix} \dfrac{z_{11}^2 - 1}{(z_{11} - 1)^2} & 0 \\ 0 & \dfrac{z_{11}^2 - 1}{(z_{11} - 1)^2} \end{vmatrix}.$$

We shall assume that each radiator taken separately is matched. Then S'_A is obviously a null matrix. It follows directly from this that $z_{11}=1$.

We then obtain the following formula for the scattering matrix of the system of apertures

$$S_A = \begin{vmatrix} s_1 & s_2 \\ s_2 & s_1 \end{vmatrix},$$

where:

$$s_1 = -\frac{z_{12}^2}{4 - z_{12}^2}; \quad s_2 = \frac{2z_{12}}{4 - z_{12}^2}. \qquad (15)$$

Let us now set up the compensation equations. Let the compensation circuit represent a mutual four-port waveguide network which is symmetrical with respect to two relatively perpendicular axes. Then, as we know

$$S_M = \left[\begin{array}{cc|cc} s_{11} & s_{12} & s_{13} & s_{14} \\ s_{12} & s_{11} & s_{14} & s_{13} \\ \hline s_{13} & s_{14} & s_{11} & s_{12} \\ s_{14} & s_{13} & s_{12} & s_{11} \end{array}\right].$$

Substituting the elements of matrices S_A and S_M in formula (12), we obtain the combined system scattering matrix S. The compensation condition (diagonality of matrix S) has the following appearance in expanded form:

$$\begin{gathered} s_{12}\left[(1 - s_1 s_{11} - s_2 s_{12})^2 - (s_2 s_{11} + s_1 s_{12})^2\right] + s_{13}\left[(1 - s_1 s_{11} - s_2 s_{12})\cdot\right. \\ \cdot\left.(s_2 s_{13} + s_1 s_{14}) - (s_2 s_{11} - s_1 s_{12})(s_2 s_{14} + s_1 s_{13})\right] - s_{14}\left[(1 - s_2 s_{12} - s_1 s_{11})\cdot\right. \\ \left.(s_2 s_{14} - s_1 s_{13}) - (s_2 s_{11} - s_1 s_{12})(s_2 s_{13} - s_1 s_{14})\right] = 0, \end{gathered} \tag{16}$$

where s_1, s_2 -- are the elements of matrix S_A,
s_{11}, s_{12}, s_{13}, s_{14} -- are the elements of matrix S_M.

We shall implement the compensation circuit as a system of two waveguides connected via a coupling port as is shown in Fig. 2.

Here 1,2,3,4 are the terminal numbers of the multi-port waveguide network.

The scattering matrix can be written as follows:

$$S_M = e^{i\theta}\begin{vmatrix} -\Gamma & \frac{i\chi}{\sqrt{2}} & \sqrt{1-\Gamma^2-\chi^2} & \frac{i\chi}{\sqrt{2}} \\ \frac{i\chi}{\sqrt{2}} & -\Gamma & \frac{i\chi}{\sqrt{2}} & \sqrt{1-\Gamma^2-\chi^2} \\ \sqrt{1-\Gamma^2-\chi^2} & \frac{i\chi}{\sqrt{2}} & -\Gamma & \frac{i\chi}{\sqrt{2}} \\ \frac{i\chi}{\sqrt{2}} & \sqrt{1-\Gamma^2-\chi^2} & \frac{i\chi}{\sqrt{2}} & -\Gamma \end{vmatrix}.$$

where Γ is the coefficient of reflection from the section containing the coupling port, α is the gain of the coupling port. (The diameter of the port is assumed to be fairly small, and the port itself is considered to be a waveguide which passes only frequencies above those of the coupled waveguides.)

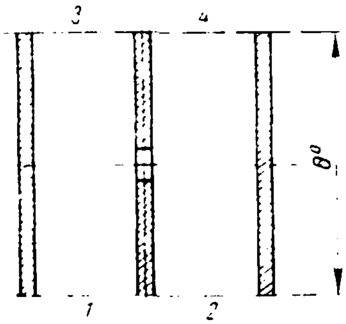

Fig. 2.

As we know, the condition that there be no active losses in the circuit requires that the scattering matrix be unitary. It is easy to show that a matrix is unitary if $\alpha^2 = 2\Gamma(1-\Gamma)$. Substituting the elements of S_M in equation (16), we obtain

$$[illegible]\; s_2 \,\big]\, \frac{\sqrt{1-\Gamma}}{\Gamma} e^{i\Theta} - i\,2s_1\, e^{i\Theta} \; [illegible]\; s_2\, e^{-i\Theta} \; [illegible]$$

The elements of the scattering matrix of the aperture system can either be measured directly [4], or calculated using formulas (15). In the latter case, the solution for the electrical length of the bridge appears as follows:

$$\tan\Theta = \frac{bc \cdot \frac{4a}{r^2 - x^2}\sqrt{1-r^2}}{a^2 - c^2}.$$

where $a = 2r;\; r - ix = z_{12};$

$$b = 2r - \frac{4r}{r^2 - x^2};$$

$$c = \frac{4x}{r^2 - x^2}.$$

Since $r^2<1$, there are always two real solutions for tan Θ which coincide when $r=0$; accordingly, there are two solutions for the coefficient of reflection Γ or the gain α.

We thus obtain two systems of parameters for the circuit which compensates a wave passing from one channel to another because of cross coupling due to the wave which enters that channel via the coupling port.

It is clear that both the radiators and the compensation circuit produce some reflection at the input of the system. Obviously, with the appropriate phase relationships these two reflected waves can be at least partially compensated. Therefore, of the two solutions obtained for (16) above, the one for which $|S_I|$ has the smallest value should be selected; then the antenna system with total compensation of energy leakage from one channel to another will have the least possible reflection at the input.

An example of the calculation follows.

The following two solutions were obtained for the compensation equation for coupling impedance $z_{12}=-0.13--i0.44$:

$$\Theta_1 = 19^\circ 30'; \quad \Theta_2 = 13^\circ 04';$$
$$\Gamma_1 = 0{,}050; \quad \Gamma_2 = 0{,}035;$$
$$z_1 = 0{,}308; \quad z_2 = 0{,}26.$$

(It is easy to show that two different solutions occur for Γ and Θ because of the mismatch between each radiator and its feeder line when operating in the system.)

Substitution of the solutions obtained in the formula for S_I produce the following results:

$$|S_I|_1 = 0{,}218; \quad |S_I|_2 = 0{,}0199.$$

Obviously, the second solution is preferable, since it provides partial cross-compensation for reflected waves, as a result of which a 2% coefficient of reflection is obtained at the input of the entire system with total channel decoupling.

CONCLUSION

The phenomenon of leakage of electromagnetic energy from the aperture of one radiator to the input of another, sometimes called "backward" cross-coupling, produces variation in the amplitude-phase distribution in the antenna assigned by the contol system.

The method proposed in the present work makes it possible to determine the parameters of a waveguide connection which compensates for "backward" cross-coupling.

Further development of this method will make it possible to compensate for "forward" cross-coupling, which causes distortion of the directivity pattern of a radiator in a system.

LITERATURE

1. Hannan P. W., Lerner D. S., Knittel G. H. Impedance Matching a Phased Array Antenna over wide Scan Angles by Connecting Circuits. I.E.E.E. Transactions on Antennas and Propagation, 1965, v. AP-13, № 1.
2. Теория линий передачи сверхвысоких частот, ч. II. «Советское радио», 1951 (перевод с англ.).
3. О. Г. Вендик. Антенны с немеханическим движением луча. «Советское радио», 1965.
4. А. З. Фрадин, С. В. Рыжков. Измерение параметров антенн. Связьиздат, 1962.

METHODS FOR CALCULATING EDGE EFFECTS IN PHASE DIPOLE ARRAY

L.A. Cherches

Iterative computational methods are used to determine the distribution of currents over the elements of an array. The convergence of the iterative processes is investigated. Examples of the variation in the impedance and gain of the elements as a function of their position in the array are presented.

Interaction between the elements in antenna arrays produces significant variation in the input impedance, directivity pattern and gain of the elements as compared with isolated radiators. However, practically all of the literature on this matter is devoted to the characteristics of antennas with few elements or the central elements in multi-element arrays. In the latter case, the parameters are examined for an infinite array. As concerns the parameters of the edge radiators of multi-element arrays, there is not enough information concerning them in the literature. An approximate examination of special cases is given in [1,2]; [3] notes the complexity of the problem. The present work investigates methods for calculating edge effects in an active array (in which each element is driven by a separate oscillator or loaded to a receiver). For simplicity we shall assume that all of the radiators and oscillators (receivers) are the same. The phase in each element of the array can be adjusted.

It is most difficult to calculate the current distribution across the elements of an array with a large but finite number of radiators (or in a semi-infinite array).

The current distribution is found from the following system of linear algebraic equations:

$$I_m + \frac{1}{Z_0 + Z_H} \sum_{p=1}^{\prime} Z_{mp} I_p = I_{m0} \qquad (1)$$

where I_{m0} is the current from the mth element in the absence of cross-coupling between elements; N is the number of elements in the array, Z_0 is the inherent impedance of the element, Z_H is the load impedance referred to the element input, Z_{mp} is the impedance produced by the pth element on the mth; the prime next to the summation symbol designates that the term in which p=m is missing. In thin dipoles (with electrical radius ρ=kr of the order of, or less than, 0.1) which are not located too close together (with an electrical distance between the centers of adjacent elements of t>1) and which are near-resonant (half-wave), the lengthwise current distribution is close to the sinusoidal distribution used in the approximate theory [4]; we use the induced emf method to determine the induced impedances.

Direct methods of solving system (1) for multi-element arrays are difficult even when computers are used. It is more convenient to use iterative methods.

According to a simple iterative process (method of sequential approximation) [5],

$$I_m^{(n)} = I_{m0} - \frac{1}{Z_0 + Z_H} \sum_{p=1}^{N}{}' Z_{mp} I_p^{(n-1)} . \qquad (2)$$

We can use

$$I_m^{(0)} = I_{m0}.$$

as the initial approximation. We shall estimate the convergence region of the iterative process based on the condition, rigorously valid for an infinite array, that

$$|Z_{\text{нав}}| < |Z_{11} \quad Z_{\text{н}}|, \tag{3}$$

where Z_{HBB} is the impedance induced on the element by other elements.

The rate of convergence of the iterative process from the convergence factor magnitude

$$q = \left| \frac{Z_{\text{нав}}}{Z_{11} \quad Z_{\text{н}}} \right|$$

corresponds to a geometric progression.

Figure 1 shows the convergence regions for parallel half-wave dipoles with various load impedances:

$Z_H = \bar{Z}_0$ -- matching between isolated dipole and load,
$Z_H \to 0$ -- short-circuiting of dipole,
$Z_H = \bar{Z}_\infty$ -- matching between dipole and load in infinite phased array.

Here $\bar{Z}$ is the quantity complex conjugate with Z.

The iterative process can be caused to diverge by the reduced spacing which results from increased cross-coupling between elements, by the direction of the primary radiation approaching the plane of the array, and by reduction in the load impedance resulting in weakening of condition (3), and by approaching the zone in which the secondary diffraction beam appears. The latter produces a drop in the directional gain, and consequently an increase in the impedance of the dipole due to increased induced impedance. As a result, the absolute value of the induced impedance increases, which degrades condition (3).

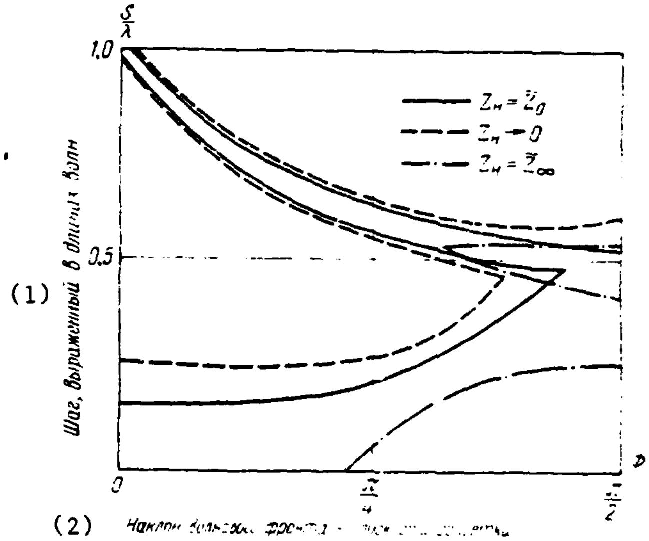

Fig. 1.

Key: (1) spacing, expressed in wavelengths; (2) inclination of wave front to array plane.

In the most important case of matching dipoles in the center of a phase multi-element array ($\bar{Z}_H \approx Z_\infty$), the convergence region is large and includes the most interesting values of array spacing and wave front slope. As the load impedance drops, the convergence region becomes significantly smaller. The following examples are given for the worst case of convergence ($Z_H \to 0$).

Figure 2 shows convergence regions for shielded arrays (in which a metal shield is placed in front of the dipole plane). With small distances from the shield d the interval s/λ which provides the convergence varies little from an angle of inclination of the wave front to the array plane ϕ, and is wider than without the shield. When there is a substantial difference between the array plane and the shield, the contour of the convergence region is analogous to that when there is no shield (with a "tongue" in the area of occurrence of the secondary diffraction beam).

Figure 3 shows the convergence factor as a function of the angle of inclination of the wave front for beam rocking in different planes [H, E, diagonal (D)] for a two-dimensional array of half-wave dipoles with elements arranged in a square (with spacing in the H plane the same as the spacing in the E plane) with a typical distance from the shield of $d=\lambda/4$. Figure 4 shows the convergence factor for beam rocking in the E plane for various spacing. These curves characterize the convergence region ($q<1$) and rate of convergence, which increases as q drops.

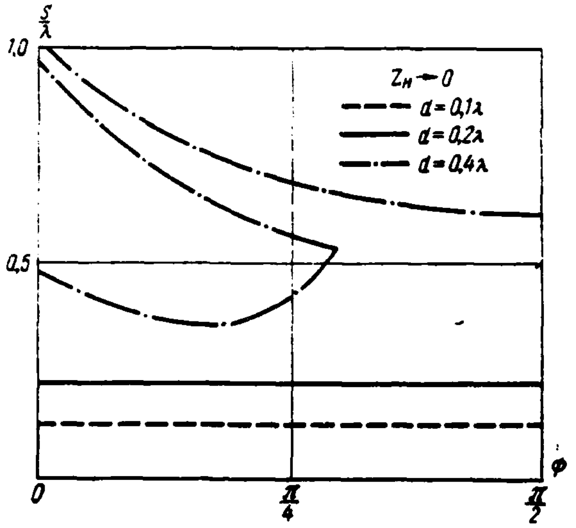

Fig. 2.

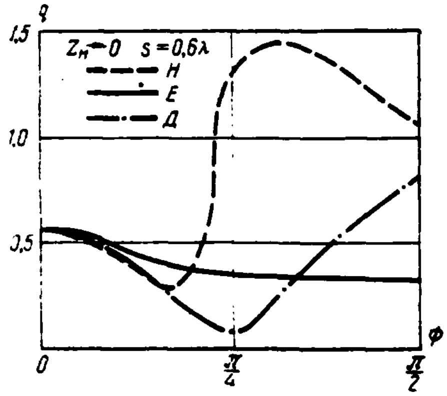

Fig. 3.

It is not difficult to calculate the current distribution allowing for edge effects for a linear array, but the same calculation for a two-dimensional array is extremely cumbersome. In many cases (for example when studying edge effect in the H plane) a quasi-two dimensional array model (unbounded in the E plane) is useful [1]. It is convenient to do the preliminary analysis for an array of conductors [1] with uniform current distribution. The introduction of a conductor to the discussion is the same as considering only the constant components of the actual current distribution along the vibrator column line. The interaction among the higher harmonics of the currents is weaker: a rapidly converging iterative algorithm can be constructed which uses the solution for a conductor array.

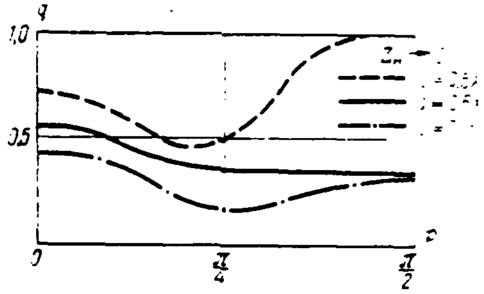

Fig. 4.

Let us consider a system of conductors in more detail. In this case, referring all of the impedance to a conductor section one wavelength long, according to [1] we have the following for thin dipoles:

$$Z_0 = 60\pi^2 H_0^{(2)}(\rho),$$
$$Z_{mp} = 60\pi^2 H_0^{(2)}(|m-p|t).$$

where $H_0^{(2)}(x)$ is a Henkel function of the second sort. For phased excitation along the conductor with uniform phase distribution of the emf between the conductors, the current distribution is determined by the following system of equations:

$$I_m + \frac{1}{60\pi^2 H_0^{(2)}(\rho) + Z_n} \sum_{p=1}^{N}{}' 60\pi^2 H_0^{(2)}(|m-p|t) I_p = e^{imt\sin\Phi}. \qquad (4)$$

Here Z_H is the load impedance for a conductor segment with length λ.

Using the sequential approximation method

$$I_m^{(n)} = e^{i\,mt\sin\phi} - \frac{1}{H_0^{(2)}(t) + \frac{Z_H}{60\pi^2}} \sum_{p=1}^{N}{}' H_0^{(2)}(|m-p|t)\, I_p^{(n-1)}$$

For the null approximation we can, for example, use

$$I_m^{(0)} = e^{imt\sin\phi}.$$

The convergence region of the iterative process can be estimated on the basis of an array which is unbounded on both sides. For a phased array the convergence condition

$$\left|\sum_{p=1}^{\infty} H_0^{(2)}(pt)\right| < \left|\frac{H_0^{(2)}(t)}{2} + \frac{Z_H}{120\pi^2}\right|. \tag{5}$$

For t<2π

$$\sum_{p=1}^{\infty} H_0^{(2)}(pt) = -\frac{1}{2} + \frac{1}{t} - i\left[-\frac{1}{\pi}\left(C - \ln\frac{4\pi}{t}\right) - \right.$$

$$\left. -2\sum_{l=1}^{\infty}\left(\frac{1}{\sqrt{(2\pi l)^2 - t^2}} - \frac{1}{2\pi l}\right)\right];$$

for $t \ll 2\pi$

$$\sum_{p=1}^{\infty} H_0^{(2)}(pt) \simeq -\frac{1}{2} - \frac{1}{t} + \frac{i}{\pi}\left(C - \ln\frac{4\pi}{t}\right),$$

where C is Euler's constant.

Figure 5 presents a diagram of the coefficient of convergence. With close spacing, on the order of a wavelength, with which a secondary diffraction lobe occurs directed along the array, the iterative process diverges.

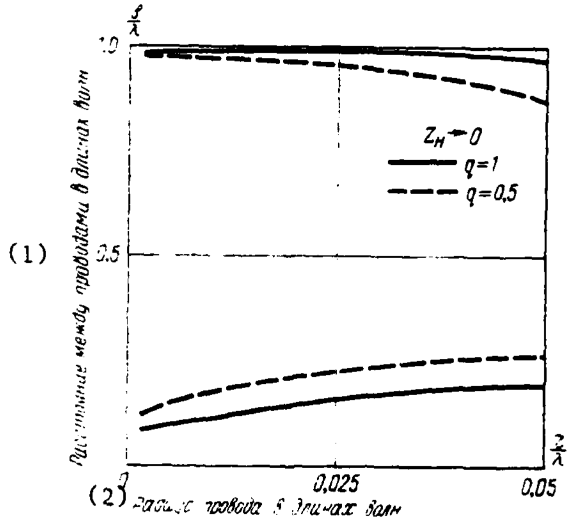

Fig. 5.

Key: (1) distance between conductors, wavelengths; (2) conductor radius, wavelength.

These few examples explain that a simple iterative process is usually suitable (converges rapidly). However, in a number of cases, for example when the spacing is close, a simple iterative process (and analogous processes) either converges slowly or even diverges. In these cases, it is necessary to construct more complicated iterative algorithms which converge rapidly. Here is an example of such an iterative process for matrix equation (4).

Let us consider the standard integral equation

$$I'(m) - \frac{60\pi^2}{Z_0 + Z_H} \int' H_0^{(2)}(|m-x|t)\, I'(x)\, dx = e^{i\, mt \sin\Phi} \qquad (6)$$

Here the symbol $\int'$ means $\int\limits_{0,5}^{m-0,5} + \int\limits_{m+0,5}^{N+0,5}$. Equations (4) and (6) can be considered as functional equations with operators which are close in some space. The iterative algorithm used to solve (4) on the basis of (6) appears as follows:

$$I_m^0 \quad I(m) \quad \frac{60\pi^2}{(\overline{Z}_0 \quad \overline{Z}_H)} \sum' H(m \quad n)I_n^0 \; - \; \text{[illegible]}$$

$$- \; x\rho I'(x)dx \quad \frac{60\pi^2}{(\overline{Z}_0 \quad \overline{Z}_H)} \int \Bigg| \sum H(\;z \quad \text{[illegible]} \quad I_z^0$$

$$\int H(\;z \quad x\rho\, I(x)dx \Bigg| \Gamma(m,\; z)dz \;. \tag{7}$$

Here Γ is the resolvent of the standard equation.

Let us consider the solution of the standard equation for N→∞ (for a semi-infinite array). An asymptotic solution can be devised for large finite N. We designate u=mt, u'=xt and I(u) -- the function complex conjugate with I'(u). Then

$$\overline{I}(u) - \frac{60\pi^2}{(\overline{Z}_0 - \overline{Z}_H)t} \int^{u} H_0^{(1)}(u - u')\overline{I}(u')du' \quad e^{\text{[illegible]}}$$

Here

$$\int^{u} \cdot \int_{0}^{m-0.5t} \quad \int^{\infty} \text{[illegible]} \;.$$

$$\beta \; \frac{\pi}{2} \; -\Phi,$$

$$\overline{Z}_0 = 60\pi^2 H_0^{(1)}(\rho), \quad \overline{Z}_H \quad \text{[illegible]}$$

We introduce the following equation with a close integration domain

$$\tilde{I}(u) - \frac{60\pi^2}{(\overline{Z}_0 - \overline{Z}_H)t} \int_0^{\infty} H_0^{(1)}(\beta|u - u'|)I(u')du' \; = e^{\text{[illegible]}} . \tag{8}$$

This is a nonuniform equation of the Weiner-Hopf-Foch second sort. Using the familiar factorization [6], we have

$$\tilde{I}(u) \; [illegible] \sin\beta \Bigg| \; [illegible] \; \Bigg| \qquad (9)$$

where

$$\psi(i\cos\tau) \; [illegible] \; \exp\left([illegible] \right)$$

Here

$$\sin\sigma = -\frac{120\pi^2}{(\bar{Z}_0 - \bar{Z}_н)\,t}.$$

Then we find I(u) using the iterative algorithm for solving an integral equation based on an equation with a close kernel [7]. Variation in the integration domain in the equation for I(u) rather than the equation for I(u) can be considered as replacing the kernel

$$K = H_0^{(1)}(|u-u'|)$$

with the close kernel

$$K' = \begin{cases} H_0^{(1)}(|u-u'|) - \ldots (0{,}5t[m-0{,}5])\,t \text{ и } ([m+0{,}5]\,t,\ \infty) \\ 0 \qquad - \ldots (0;\ 0{,}5t) \text{ и } ([m-0{,}5]\,t,\ [m+0{,}5]\,t). \end{cases}$$

As a result

$$\bar{I}^{(n)}(u) = \tilde{I}(u) + \frac{60\pi^2}{(\bar{Z}_0 - \bar{Z}_н)\,t} \int^{*} K^{*}\, \bar{I}^{(n-1)}(u')\,du',$$

where

$$\int^{*} = -\int_0^{0{,}5t} - \int_{(m-0{,}5)t}^{(m+0{,}5)t}, \qquad (10)$$

$$K^{*} = H_0^{(1)}(|u-u'|) - \int_0^{\infty} \tilde{\Gamma}(u,\ v)\, H_0^{(1)}(|u-u'|)\,dv.$$

Here Γ is the resolvant [8] of equation (8);

$$\tilde{\Gamma}(u,v)=\gamma(u-v,0)-\int_0^\infty \gamma(u-w,0)\gamma(v-w,0)\,dw,$$

$$0\leqslant u,\ v<\infty,$$

where

$$\gamma(u,0)=-i\,\frac{\sin\vartheta}{\pi}\int_0^\infty \frac{e^{iu\,\mathrm{ch}\,x}(\mathrm{ch}^2x-1)\,dx}{\psi(i\,\mathrm{ch}\,x)(\mathrm{ch}^2x-\cos^2\vartheta)}.$$

Let us examine the error of approximate solution using the example of an unbounded phased array of conductors. In this case the solution of a matrix equation of type (4) appears as

$$I=\frac{1}{1-\dfrac{120\pi^2}{60\pi^2 H_0^{(2)}(\rho)-Z_H}\displaystyle\sum_{p=1}^{\infty}H_0^{(2)}(pt)},$$

and the approximate solution (solution of standard equation)

$$I'=\frac{1}{1-\dfrac{120\pi^2}{t\,(60\pi^2 H_0^{(2)}(\rho)-Z_H)}\displaystyle\int_{0.5t}^{\infty}H_0^{(2)}(u')\,du'}.$$

It is not difficult to determine the relative error of the approximate solution

$$\delta I=\frac{I'-I}{I}$$

Considering

$$\int_{0.5t}^{\infty}H_0^{(2)}(u')\,du'=1-\frac{\pi}{4}t\left\{S_0(0.5t)H_1^{(2)}(0.5t)+\left[\frac{2}{\pi}-S_1(0.5t)\right]H_0^{(2)}(0.5t)\right\}$$

where $S_{0,1}(x)$ are zero- and first-order Struve functions, respectively; $H_1^{(2)}(x)$ is a first-order Henkel function of the second sort. For example, when t=1, ρ=0.01, $Z_H \rightarrow 0, |\delta I| \approx 0.05$.

In many cases, the solution to the standard equation is closer to the currents being determined than a substantial sequence of simple iterations (not to mention that the standard-equation method is sometimes applicable when a simple iterative process diverges). Iterative algorithm (7) can be used to increase accuracy.

With the usual distance between the plane of the array and the shield $d \simeq \lambda/4$ and spacing $s = \lambda/2$, a simple iterative process for a system of conductors is satisfactory with any wave front slope. The coefficient of convergence

$$q = \frac{\sum_{n=1} \text{[illegible]}}{\text{[illegible]}} \qquad (11)$$

where $T = 2kd$ is the electrical distance between the conductor and its image on the shield.

Figure 6 shows the coefficient of convergence as a function of scanning angle.

We have dealt with the computational aspect of determining the currents in so much detail because this calculation is the most difficult and serves as the key to research allowing for the edge effect of the remaining characteristics (array directivity pattern, input impedance, element directivity pattern and gain). The formulas needed for an unbounded array are contained in [9]. Without dwelling on these standard (for predefined currents) calculations, we now present some numerical findings to illustrate the nature of the edge effect.

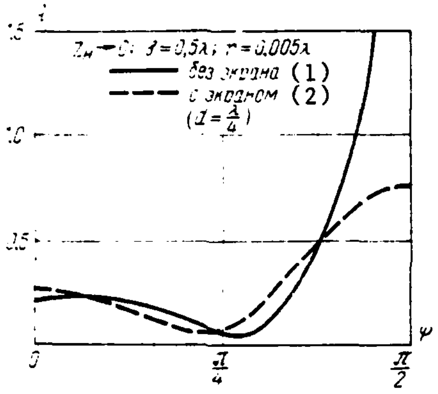

Fig. 6.

Key: (1) without shield; (2) with shield.

Figure 7 shows the odd component, with respect to the middle of the array, of the variation in the phase of the current due to cross-coupling for edge elements. (The odd component is of more interest than the even one because it produces asymmetry in the array directivity pattern.) Although the results shown in Fig. 7 are calculated for a system of conductors (with load impedance corresponding to matching in a phased unbounded array), the nature of the relationships remains essentially unchanged for linear and two-dimensional half-wave parallel dipoles as well.

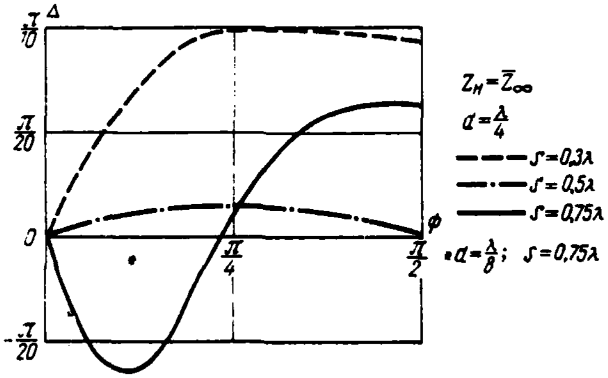

Fig. 7.

The diagram in Figs. 8 and 9 show the input impedance and gain of the elements G_m of phased semi-infinite arrays of collinear and parallel half-wave dipoles as a function of their position with respect to the edge.

The parameters of the elements near the edge differ significantly from the parameters of other elements. This is also the case for other types of multi-element arrays.

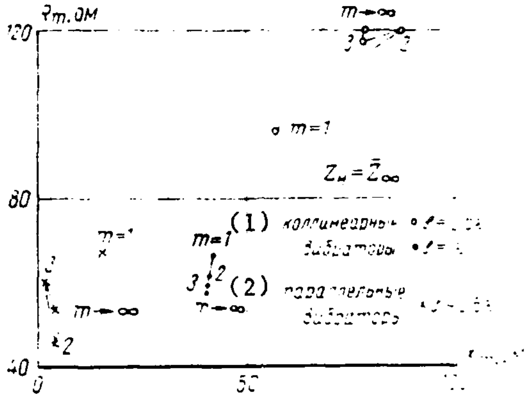

Fig. 8.

Key: (1) collinear dipoles; (2) parallel dipoles.

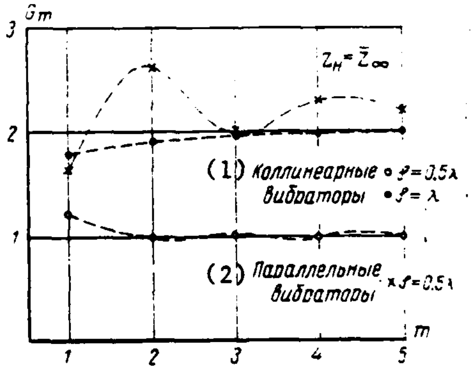

Fig. 9.

Key: (1) collinear dipoles; (2) parallel dipoles.

LITERATURE

1. Carter P. S. Mutual Impedance effects in [illegible] Beam Scann[illegible] «IRE Trans», AP-8, № 3, 1960, p. 276—287.

2. Кутузов С. М. В[illegible] ной решетке. «Электро[illegible]» № 10 [illegible]

3. Фельд Я. Н. Бе[illegible] теории антенн. Сборник [illegible] под ред. А. А. Пистолькорса [illegible]

4. King R. W. P. [illegible] Antenna [illegible] I.E.E.E.» 75, № 1, 1967, pp. 2—1[illegible]

5. Фельд Я. Н. [illegible] Изд-во Академии ВВИА [illegible] 195[illegible]

6. Г[illegible] Ф[illegible] магнитных волн. [illegible] ред. Б. А. Введенского [illegible]

7. Бельтюков Б. А. Построение [illegible] рифмов для решения интегральных уравнений [illegible] журнал», VI, № 6, 1965, стр. 1415—1419.

8. Крейн М. Г. Интегральные [illegible] сящим от разности аргументов. «У[illegible] VIII [illegible] стр. 3—120.

9. Allen J. L. Gain and Impedance Variation in S[illegible] «IRE Trans.», AP-10, № 5, 1962, pp. 566—572.

CONSIDERATION OF CROSS-EFFECT OF RADIATORS IN CYLINDRICAL SLOT ANTENNA ARRAYS

B.A. Panchenko

Analytical formulas are obtained to allow for the influence of radiator cross coupling on the admittance and energy characteristic of antenna arrays consisting of long slots on the surface of a round cylinder. Linear and ring arrays operating in phase and equiphase are examined.

INTRODUCTION

In analyzing the operation of antenna arrays, attention has recently begun to be devoted to effects occurring in antennas due to interaction of the radiators [1,2,3,4]. This interest is entirely justified, since certain array parameters depend significantly upon the amount of interaction between the radiators. Regardless of whether the array elements are driven individually or a branched feed system is used, a significant share of the interaction effect belongs to coupling of the radiators through external space. This portion of the problem must be solved for the specific type of radiators and the geometry of the external region. The solution which is obtained can then be used in estimating the parameters of an antenna system using a specific feed system. In addition, solving the external problem makes it possible to determine changes in the antenna parameters, e.g., the directional gain, caused by interaction of the elements in the external space alone.

The influence of cross-coupling of radiators in a multi-element antenna array consisting of long slots arranged on the surface of a round cylinder is investigated below.

INTERACTION OF ELEMENTS IN LINEAR ARRAY OF SLOTS ON A CYLINDER

The interaction of radiators in the form of longitudinal slots arranged in a single row on the surface of a round cylinder (Fig. 1) is examined. It is assumed that the uniform array contains a fairly large number of elements, so that the influence of "edge" effects on the overall antenna characteristics can be disregarded.

The conductivity of the nth array element, allowing for mutual effect (Y'_{nT}) is determined by the intrinsic Y_{nn} and mutual Y_{pn} conductances of the longitudinal slots on the cylinder:

$$Y'_{nn} = \sum_{p=1}^{\infty} Y_{pn} e^{-ikdp \sin\theta}, \tag{1}$$

where $\kappa = \omega\sqrt{\varepsilon\mu} = \frac{2\pi}{\lambda}$ is the wave number, θ is the angle in the direction of which the array is phased.

On the other hand, considering that the elements are arranged periodically in the array, Y'_{nn} can be considered as the intrinsic conductance of a slot which radiates into a fictive radial round waveguide with distance d between its walls in the direction of the long axis. The conductivity of a slot in such a waveguide with electrical field intensity $E_n(r)$ distributed in the port is defined by the general expression [5]

$$Y'_{nn} = \int_S E_n(\vec{r})\left(k^2 + \frac{\partial^2}{\partial z^2}\right)\int_S G(\vec{r},\vec{r}')E_n(\vec{r}')\,ds'\,ds, \tag{2}$$

where $G(\vec{r},\vec{r}')$ is the Green function of the external region of the cylinder in the presence of additional barriers which form a radial waveguide;

$$G = \frac{1}{i\omega\mu 2\pi da}\sum_{m,q=-\infty}^{\infty}\frac{H_m^{(2)}\left(a\sqrt{k^2-\left(\frac{2\pi q}{d}-k\sin\theta\right)^2}\right)}{H_m^{(2)\prime}\left(a\sqrt{k^2-\left(\frac{2\pi q}{d}-k\sin\theta\right)^2}\right)} \cdot \frac{1}{\sqrt{k^2-\left(\frac{2\pi q}{d}-k\sin\theta\right)^2}}\, e^{im(\varphi-\varphi')}\, e^{-i\left(\frac{2\pi q}{d}-k\sin\theta\right)(z-z')} \tag{3}$$

where m and q are integers; $H_m^{(2)}(x)$, $H_m^{(2)\prime}(x)$ is Henkel's function and its derivative.

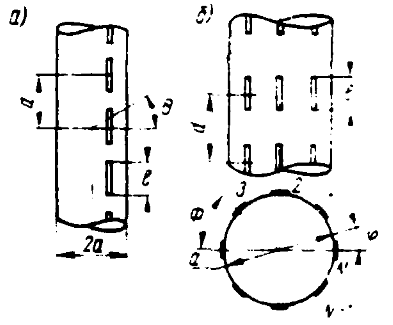

Fig. 1.

With a "waveguide" treatment of the problem, the expression for the conductivity after transformations in expression (2) takes on the form

$$Y = -\frac{2}{\pi(\kappa a)\kappa d}\left(\frac{\kappa l}{\pi}\right)^2\sqrt{\frac{\varepsilon}{\mu}}\sum_{m,q=-\infty}^{\infty}{}' \frac{H_m^{(2)}\left(\kappa a\sqrt{1-\left(\frac{2\pi q}{\kappa d}-\sin\Theta\right)^2}\right)}{H_m^{(2)\prime}\left(\kappa a\sqrt{1-\left(\frac{2\pi q}{\kappa d}-\sin\Theta\right)^2}\right)}\cdot$$

$$\sqrt{1-\left(\frac{2\pi q}{\kappa d}-\sin\Theta\right)^2}\left[\frac{\cos\left[\frac{\kappa l}{2}\left(\frac{2\pi q}{\kappa d}-\sin\Theta\right)\right]}{1-\left[\frac{\kappa l}{\pi}\left(\frac{2\pi q}{\kappa d}-\sin\Theta\right)\right]^2}\right]^2. \qquad (4)$$

This expression is complex. In the future we shall be interested primarily in the active component of the conductivity

$$G = \frac{1}{\pi^2\kappa a(\kappa a)^2}\sqrt{\frac{\varepsilon}{\mu}}\left(\frac{\kappa l}{\pi}\right)^2\sum_{m=0}^{\infty}\varepsilon_m\sum_{q=-\infty}^{+\infty}{}' \frac{1}{\left|H_m^{2}\left(\kappa a\sqrt{1-\left(\frac{2\pi q}{\kappa d}-\sin\Theta\right)^2}\right)\right|^2}\cdot \qquad (5)$$

$$\left[\frac{\cos\left(\frac{\kappa l}{2}\left(\frac{2\pi q}{\kappa d}-\sin\Theta\right)\right)}{1-\left(\frac{\kappa l}{\pi}\left(\frac{2\pi q}{\kappa d}-\sin\Theta\right)\right)^2}\right]^2 \qquad \varepsilon_m = \begin{matrix} 1 & m=0 \\ 2 & m=1,2\ldots \end{matrix}$$

The prime over the summation sign in expression (4) [sic] indicates that those members of the series for which $\left(2\pi q/\kappa d - \sin\Theta\right)\leq 1$ are considered in the summation.

1. Considering each new term of the series q is associated with the possibility of propagation of the next type of wave in the fictive waveguide. In an actual array, this corresponds to the instant of occurrence of the diffraction maxima in the directivity pattern.

Expression (5) can be simplified in some cases. For example, for an equiphase array with elements spaced $d<\lambda$ apart, only the term with $q=0$ must be considered in the second sum.

Figure 2 shows the plots calculated for the conductivity of the elements in the array as a function of the radius of the cylinder. Because of the complex relationship between the conductivity and the period of the array, the curves for different d/λ may be either above or below the limiting term for $d/\lambda \to \infty$.

In order to allow for the influence of cross-coupling on directional gain, we introduce the coefficient g which characterizes the ratio of the directional gain of the array considering cross-coupling to the directional gain of the same antenna disregarding coupling [6]. In the case of a linear array (disregarding edge effects) the coefficient g is associated very simply with the active conductance of the element:

$$g = \frac{1}{\bar{G}'} \frac{G_1}{G_0}. \tag{6}$$

where G_0 is the radiation conductance of the single slot.

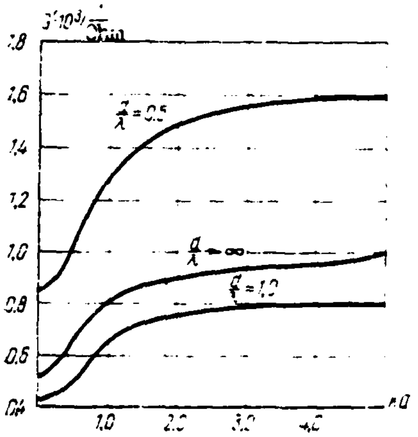

Fig. 2.

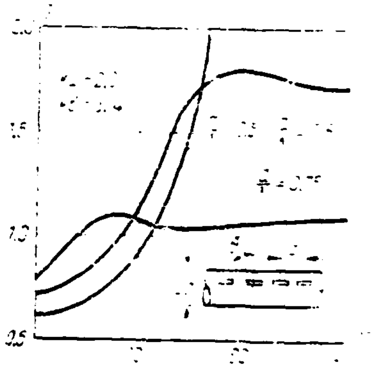

Fig. 3.

Figure 3 shows the plots of g=f(Θ) with several values of the array period for ka=2.0. The nature of the variation of g differs little from the corresponding plots for a linear array on a plane [6]; however, the numerical values for these two cases differ significantly. The calculation was done using formulas (5) and (6).

INTERACTION OF ELEMENTS IN MULTI-ROW ARRAYS

Let the array consist of N rows of regularly arranged longitudinal slots (cf. Fig. 1b). It is sometimes convenient to consider this antenna as a multi-ring antenna with N radiators in each ring. As we know, these arrays can operate in either the equiphase directional radiation mode, or the phased directional radiation mode.

The "waveguide" treatment of the problem is extremely fruitful in analyzing operation in the equiphase radiation mode; the use of this treatment will save substantial time in the calculations. The conductances of all of the elements in the array (except for the end elements in each row) are the same, and equal to the conductance of the slot which radiates into a radial sector waveguide with sector apex angle of Φ=2π/N and distance d between the plates in the direction of the long axis. With an array period of d<λ, the expression for the active conductance appears as

$$G' = \frac{4N}{\pi^2 \kappa d (\kappa a)^2}\left(\frac{l}{\pi}\right)^2 \sum_{m=0}^{\infty} \frac{\varepsilon_m}{\left|H^{(2)\prime}_{Nm}(\kappa a)\right|^2} . \tag{7}$$

In the calculations, it is sufficient in (7) to consider those members of the series in which the index of the Henkel functions are equal to or smaller than the argument of the function, i.e., m≤ka/N. Figure 4 shows the results of numerical calculations of the normalized active conductance of elements as a function of the number of radiators in a ring. The plots are oscillatory in nature. For small N the influence of adjacent elements due to surface curvature is small (with respect to the flat initial segment of the curves). With large N (a distance <0.5λ between adjacent elements in a ring), the conductance increases monotonically because of the strong coupling.

The plot of the relationship between G' and the distance between the rings has monotonic sections and brakes which correspond to the instants at which the diffraction maxima occur in the antenna directivity pattern. The influence of curvature of the shield has an effect on the numerical conductance values (Fig. 5). The calculated data are obtained for an array with a distance d'-0.5λ between the elements in the azimuthal direction.

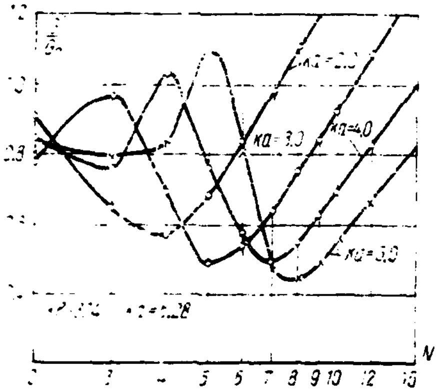

Fig. 4.

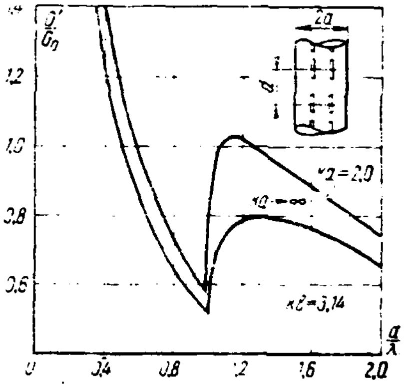

Fig. 5.

The coefficient g in this case is also defined as the inverse of the normalized value of the active conductance considering interaction (6).

Two methods were used simultaneously in analyzing the admittance and energy characteristics of multi-row phased arrays: the "waveguide" method, allowing for interaction between elements in a row and the element by element approach for a ring [3].

In order to obtain phased radiation in the direction of angles Θ, ϕ the voltage on the pth element in each ring must be

$$V_p = V_0 \Psi_p(\Theta, \varphi) = V_0 e^{-i\kappa a \sin\Theta \cos(\varphi - \varphi_p)},$$

where $\varphi_p = \frac{2\pi p}{N}$, $p = 1, 2, 3, \ldots, N$.

The conductance of the pth radiator, allowing for interaction of elements in a ring,

$$Y'_{pp} = \frac{I_p}{V_p} = \sum_{n=1}^{N} Y_{pn} \frac{V_n}{V_p} = \sum_{n=1}^{N} Y_{pn} e^{i\kappa a \sin\Theta [\cos(\varphi - \varphi_p) - \cos(\varphi - \varphi_n)]} \quad (8)$$

Here $Y_{r\Pi}$ considers the interaction of the radiators in a row:

$$Y_{pn} = \sum_{m=-\infty}^{\infty} Y_m e^{-im(\varphi_p - \varphi_n)},$$

$$Y_m = G_m + i B_m$$

$$= \frac{2}{i\pi\kappa a\kappa d} \left(\frac{\kappa l}{\pi}\right)^3 \sqrt{\text{[illegible]}} \sum_{s=-\infty}^{\infty} \frac{H_m^{(2)}\left(\kappa a \sqrt{1 - \left(\frac{2\pi s}{\kappa d}\right)^2}\right)}{H_m^{(2)\prime}\left(\kappa a \sqrt{1 - \left(\frac{2\pi s}{\kappa d}\right)^2}\right)} \quad (9)$$

$$\times \sqrt{1 - \left(\frac{2\pi s}{\kappa d}\right)^2} \left[\frac{\cos\left(\frac{\pi l s}{d}\right)}{1 - \left(\frac{2ls}{d}\right)^2}\right]^2.$$

In contrast to the cases considered above, in the directional radiation mode the conductances of the individual elements in a ring depend upon the phasing direction and the element number p=1,2,...,N.

The expression for g for the phased array takes on the appearance:

$$g = \frac{NG_0}{\sum_{p=1}^{N} \sum_{n=1}^{N} G_{pn} \Psi_n \Psi_p^*} = \frac{NG_0}{\sum_{p=1}^{N} \sum_{n=1}^{N} G_{pn} \exp\left[-i\kappa a \sin\Theta \left(\cos(\varphi - \varphi_n) - \cos(\varphi - \varphi_p)\right)\right]}. \quad (10)$$

ψ^* denotes a complex conjugate function.

Calculations using formulas (8), (9) and (10) are extremely laborious for large N. However, it is possible to represent g in a form suitable for numerical calculations with large N. In the transformations in (10), the exponents were twice expanded into a series with respect to Bessell functions $J_s(x)$

$$e^{i\kappa a\cos\Theta\cos\varphi_n} = \sum_{s=-\infty}^{\infty} (\pm 1)^s J_s(\kappa a\cos\Theta)\, e^{-is\varphi_n}$$

and the property of the sum

$$\sum_{n=1}^{N} e^{-i\frac{2\pi n}{N}(m+s)} = \begin{cases} N & \frac{s+m}{N} = 0 \pm 1 \pm 2 \ldots \\ 0 & \text{in the remaining cases.} \end{cases}$$

As a result of the transformations, we obtain

$$g = G_0 \Big\{ N \sum_{m=0}^{\infty} \sum_{s=0}^{\infty} \sum_{r=0}^{\infty} \varepsilon_m \varepsilon_s \varepsilon_r (-1)^s (-1)^r G_m \times \Big[\frac{1}{2} J_{Ns-m}(\kappa a\cos\Theta) J_{Nr-m}(\kappa a\cos\Theta) + \frac{1}{2} J_{Ns+m}(\kappa a\cos\Theta) \times J_{Nr+m}(\kappa a\cos\Theta) + (-1)^m J_{Ns+m}(\kappa a\cos\Theta) J_{Nr-m}(\kappa a\cos\Theta) \Big] \Big\}^{-1}. \tag{11}$$

The larger N, the more rapidly the series converge with respect to s and r; the number of members of the series needed with respect to m are determined by the radius of the cylinder ka.

In special cases of practical interest, expression (11) is significantly simpler. Since for d'/λ≤0.5 (d' -- distance between adjacent radiators in a ring),

$$g \approx G_0 \Big\{ N \sum_{m=0}^{\infty} \varepsilon_m G_m [J_m^2(\kappa a\cos\Theta) + J_{N-m}^2(\kappa a\cos\Theta) - (-1)^m J_m(\kappa a)\cos\Theta) J_{N-m}(\kappa a\cos\Theta)] \Big\}^{-1}. \tag{12}$$

AD-A112 088 FOREIGN TECHNOLOGY DIV WRIGHT-PATTERSON AFB OH F/G 9/5
ANTENNAS.(U)
MAR 82
UNCLASSIFIED FTD-ID(RS)T-1168-81 NL

2 of 2
AD A
112088

END
DATE
FILMED
4-82
DTIC

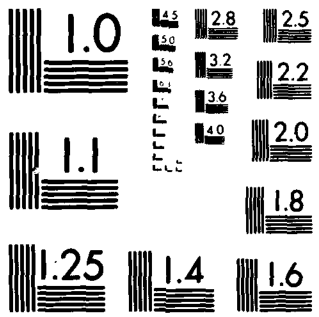

MICROCOPY RESOLUTION TEST CHART

With even smaller distances between radiators (d'/λ<0.25), we obtain

$$g \approx G_0 \left[V \sum_{m=0}^{\infty} \varepsilon_m G_m J_m^2 (\kappa a \cos \Theta) \right]^{-1}. \tag{13}$$

The coefficient G_m is determined from (9). For an array of half-wave slots with a distance between the rings of less than a wavelength

$$G_m = \frac{4}{\pi^2 \kappa d\, (\kappa a)^2} \sqrt{\frac{\varepsilon}{\mu}} \frac{1}{\left| H_m^{(2)\prime} (\kappa a) \right|^2}. \tag{14}$$

Figure 6 shows plots of g as a function of N(d'/λ). The equiphase array has an extremely favorable arrangement of elements which can provide a significant increase in the array directivity. In the phased radiation mode, these large increases in g are not observed, which is explained primarily by the different phasing of the ring elements. The drop in directional gain as (d'/λ)→0 is explained by the reduction in the dimensions of the array, and the fact that the amplitude-phase distribution used does not correspond to the super-directivity mode.

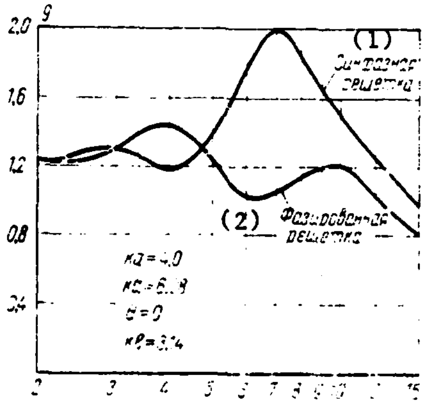

Fig. 6.

Key: (1) equiphase array; (2) phased array.

CONCLUSION

The formulas obtained make it possible to allow for the effect of external cross-coupling between radiators in multi-element arrays consisting of slots on a round cylinder. For individual elements the conductance depends upon the operating mode of the array, the distances between adjacent elements and the curvature of the shield. These relationships must be considered in selecting and designing the array feed system. Allowance for interaction of elements can introduce a significant correction to the calculated (disregarding interaction) directional gain of the system.

LITERATURE

1. S. Edelberg, A. Oliner, IRE Trans. 1960, vol. AP-8, № [illegible], 256.
2. J. Allen, IRE Trans. 1962, vol. AP-10, № 5, 566.
3. Microwave scanning antennas, vol. II, edited by R. C. Hansen, Academic Press, New Jork and London, 1966.
4. А. В. Витко, Изв. вузов. «Радиоэлектроника», 1967, X, № [illegible]
5. Б. А. Панченко, Изв. вузов. «Радиофизика», [illegible], IX, № [illegible]
6. О. Г. Вендик, Антенны с немеханическим движением [illegible] радио», 1965.

EFFECTS CAUSED BY LOAD MISMATCH IN PERIODIC SYSTEMS OF COUPLED RADIATORS

I.V. Guzeyev, A.B. Kolot

Expressions are obtained for the directivity pattern and wave amplitudes in the feeders of periodic systems of coupled radiators, assuming that the scattering matrix which allows for external cross-coupling of radiators, their partial fields (patterns) and parameters of oscillators or loads which are matched in the general case with the wave impedance of the feeder line are known.

INTRODUCTION

A substantial amount of attention has recently been devoted to investigating multi-element arrays. In these arrays, the cross-coupling between radiators can cause energy from a single driven radiator to reach the feeders of all of the other radiators and, depending upon the nature of the loads of these feeders, be either completely absorbed or cause a process of repeated reflection and re-radiation. The pattern of a single element in an array thus depends upon the scattering matrix of the array as a multi-port network, and upon the loads of the feeders of the other radiators. An analogous phenomenon occurs when a row of radiators in the system is driven simultaneously. As far as we know, phenomena caused by mismatching of the impedances of the oscillators or loads and the wave impedance of the feeder line have not been described sufficiently in the literature for systems of coupled radiators. However, it should be noted that these phenomena are important in a number of practically important cases. The present work fills this gap to some extent.

The analysis is done for periodic radiating systems which approximate the operating conditions of large arrays quite well.

FIELDS IN INFINITE PERIODIC SYSTEMS OF RADIATORS

Let us consider an infinite linear periodic array of radiators which, together with their feeders, are identical (Fig. 1). We shall assume that the feeders support only the propagation of one (basic) type of wave with forward (a_n) and reverse (b_n) wave intensity amplitudes associated as [1]:

$$b_n = \sum_{m=-\infty}^{\infty} S_{nm} a_m, \quad n = 0, \pm 1, \pm 2, \ldots, \tag{1}$$

where S_{nm} are the elements of the scattering matrix which are assumed to be known either experimentally or as a result of solving the boundary problem in electrodynamics.

Let $\vec{e}_n^{(c)}(x, y, z), \vec{h}_n^{(c)}(x, y, z)$ be dimensionless vector functions ("partial fields") of the radiators in the system, i.e., the fields created by the nth radiators when the feeders of the remaining radiators are infinite (or loaded by their wave impedances), and a wave with unit amplitude is propagating in the nth feeder toward the radiator. In this case, significant currents will be present only in the nth radiator and those close to it; therefore, at distances greater than the size of the region occupied by these radiators, the "partial patterns" $\vec{f}_n^{(c)}(\vartheta, \phi)$ correspond to the partial field $\vec{e}_n^{(c)}$, $\vec{h}_n^{(c)}$.

Since the system is periodic and satisfies the mutuality principle, the following relationships are valid for it:

$$S_{nm} = s_{|n-m|} = s_p, \quad n, m, p = 0, \pm 1, \pm 2, \ldots \tag{2a}$$

$$\left.\begin{aligned} \vec{e}_p^{(c)}(x, y, z-pd) &= \vec{e}_q^{(c)}(x, y, z-qd) \\ \vec{h}_p^{(c)}(x, y, z-pd) &= \vec{h}_q^{(c)}(x, y, z-qd) \end{aligned}\right| \tag{2b}$$

$$\vec{f}_p^{(c)}(\vartheta, \varphi) = \vec{f}_0^{(c)}(\vartheta, \varphi)\, e^{ip\kappa d \cos\vartheta}. \tag{2c}$$

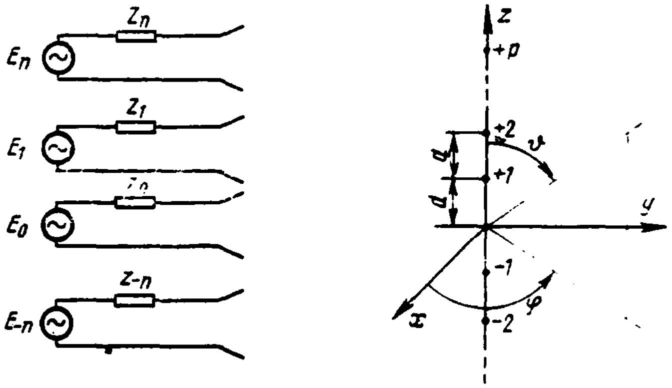

Fig. 1.

Based on the superposition principle, when waves a_p are present in all of the feeders, the resultant field or directivity pattern are:

$$E(x, y, z) = \sum_{p=-\infty}^{\infty} a_p \vec{e}_p^{(c)}(x, y, z); \ \vec{F}(\vartheta, \varphi) = \sum_{p=-\infty}^{\infty} a_p \vec{f}_p^{(c)}(\vartheta, \varphi). \tag{3}$$

We shall now introduce Fourier series consisting of the amplitudes a_p, b_p and the elements of the scattering matrix:

$$\tilde{a}(u) = \sum_{p=-\infty}^{\infty} a_p e^{ipu}; \quad \tilde{b}(u) = \sum_{p=-\infty}^{\infty} b_p e^{ipu}; \quad \tilde{s}(u) = \sum_{p=-\infty}^{\infty} s_p e^{ipu}. \tag{4}$$

Using the method in [2], it is easy to show that we can obtain the relationship

$$\tilde{b}(u) = \tilde{s}(u)\tilde{a}(u); \tag{5}$$

instead of (1); then the expression for the resultant directivity pattern is written as:

$$\vec{F}(\vartheta, \varphi) = \vec{f}_0^{(c)}(\vartheta, \varphi)\tilde{a}(\kappa d \cos\vartheta). \tag{6}$$

Analogously, for a planar array (Fig. 2), introducing dual Fourier series

$$\tilde{a}(u, v) = \sum_{n=-\infty}^{\infty} \sum_{p=-\infty}^{\infty} a_{np} e^{inu+ipv}; \quad \tilde{b}(u, v) = \sum_{n=-\infty}^{\infty} \sum_{p=-\infty}^{\infty} b_{np} e^{inu+ipv}; \tag{7}$$

$$\tilde{s}(u, v) = \sum_{n=-\infty}^{\infty} \sum_{p=-\infty}^{\infty} s_{np} e^{inu+ipv},$$

we obtain:

$$\tilde{b}(u, v) = \tilde{s}(u, v)\tilde{a}(u, v) \tag{8}$$

$$\vec{F}(\vartheta, \varphi) = \vec{f}_{00}^{(c)}(\vartheta, \varphi)\tilde{a}(\kappa d_1 \sin\vartheta \cos\varphi, \kappa d_2 \sin\vartheta \sin\varphi). \tag{9}$$

where $\vec{f}_{00}^{(c)}(\vartheta,\phi)$ is the partial pattern of the radiator located at the coordinate origin.

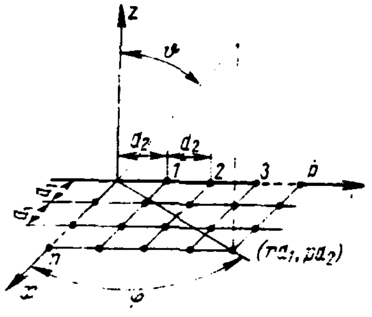

Fig. 2.

The Fourier series $\tilde{s}(u)$ and $\tilde{s}(u,v)$, comprised of the elements of the scattering matrix, will be called scattering functions below.

We note that these are even functions, since the systems in question are periodic and satisfy the mutuality principle, i.e.,

$$s_p = s_{-p} = s_{|p|}, \quad s_{n,p} = s_{-n,-p} = s_{|n|,|p|}.$$

ARRAY OF RADIATORS DRIVEN BY EMF SOURCES

In order to find the amplitudes a_p, b_p or their corresponding Fourier series $\tilde{a}(u)$, $\tilde{b}(u)$, equations (1) and (5) must be supplemented with the connection between these amplitudes and the oscillator parameters -- emf $\mathcal{E}_p$ and the coefficients of reflection Γ_p characterizing their internal impedances Z_p. This connection can be written as[1] [3]

$$a_p = c_p - \Gamma_p b_p,$$

where

$$c_p = \frac{1}{2}\kappa \; [illegible] \; (1-\Gamma_p)\,\mathcal{E}_p \tag{10}$$

---

[1] This work uses the practical MKS system of units. The time dependency is used in the form $d^{i\omega t}$.

In the case of oscillators with identical internal impedances whose emf satisfies the relationship

$$\sum_{p=-\infty}^{\infty} |\mathcal{E}_p| < \infty$$

introducing the Fourier series

$$\tilde{\mathcal{E}}(u)=\sum_{p=-\infty}^{\infty}\mathcal{E}_p e^{ipu}, \quad \tilde{c}(u) = \frac{1}{2}\kappa\sqrt{\frac{Z}{\rho}}(1-\Gamma)\tilde{\mathcal{E}}(u) \tag{11}$$

instead of (10), we obtain the following relationship:

$$\tilde{a}(u) = \tilde{c}(u) + \Gamma\tilde{b}(u). \tag{12}$$

From the system of equations (5), (12), we find:

$$\tilde{a}(u) = \frac{\tilde{c}(u)}{1-\Gamma\tilde{s}(u)}, \quad \tilde{b}(u) = \frac{\tilde{c}(u)\tilde{s}(u)}{1-\Gamma\tilde{s}(u)}. \tag{13}$$

The amplitudes a_p, b_p are obtained from (13) by the inverse Fourier transform:

$$a_p = \frac{1}{2\pi}\int_{-\pi}^{\pi}\frac{\tilde{c}(u)e^{-ipu}du}{1-\Gamma\tilde{s}(u)}; \quad b_p = \frac{1}{2\pi}\int_{-\pi}^{\pi}\frac{\tilde{c}(u)\tilde{s}(u)e^{-ipu}du}{1-\Gamma\tilde{s}(u)}. \tag{14}$$

Based on (6) and (13), the expression for the directivity pattern of a linear array takes on the appearance

$$\vec{F}(\theta, \varphi, \Gamma) = \vec{f}_0^{(e)}(\theta, \varphi)\frac{\tilde{c}(\kappa d\cos\theta)}{1-\Gamma\tilde{s}(\kappa d\cos\theta)}. \tag{15}$$

Let us consider in more detail the practically interesting special case in which only radiator is active ($\mathcal{E}_p \neq 0$ when $p=0$), while the other radiators are passive ($\mathcal{E}_p = 0$ when $p \neq 0$). In this case, we have

$$\tilde{a}(u) = \frac{c_0}{1 - \Gamma \tilde{s}(u)}, \quad \tilde{b}(u) = \frac{c_0 \tilde{s}(u)}{1 - \Gamma \tilde{s}(u)}, \tag{16a}$$

$$a_p = \frac{c_0}{2\pi} \int_{-\pi}^{\pi} \frac{e^{ipu}}{1 - \Gamma \tilde{s}(u)} du, \quad b_p = \frac{c_0}{2\pi} \int_{-\pi}^{\pi} \frac{\tilde{s}(u) e^{-ipu}}{1 - \Gamma \tilde{s}(u)} du, \tag{16b}$$

$$\vec{F}(\vartheta, \varphi, \Gamma) = c_0 \frac{\vec{f}_0^{(c)}(\vartheta, \varphi)}{1 - \Gamma \tilde{s}(\kappa d \cos \vartheta)}. \tag{16c}$$

On the basis of (16b), we obtain the following expression for the coefficient of reflection at the input of the active radiator:

$$\Gamma_{\text{вх}} = \frac{b_0}{a_0} = \frac{\displaystyle\int_{-\pi}^{\pi} \frac{\tilde{s}(u)\, du}{1 - \Gamma \tilde{s}(u)}}{\displaystyle\int_{-\pi}^{\pi} \frac{du}{1 - \Gamma \tilde{s}(u)}} = \frac{1}{\Gamma} \left\{ 1 - \frac{2\pi}{\displaystyle\int_{-\pi}^{\pi} \frac{du}{1 - \Gamma \tilde{s}(u)}} \right\}. \tag{16d}$$

By substituting $e^{iu} = z$, the integrals in expressions (14) and (16d) are transformed to contour integrals about a circle $|z|=1$ in the plane of the complex variable z, and can be calculated on the basis of the theorem of residues. The next section presents an expression for Γ_{BX} calculated using this method (cf. also Appendix).

With one active radiator, it is also easy to consider the case in which the loads in the passive channels are not equal to the internal impedance of the oscillator in the active channel ($\Gamma \neq \Gamma_0$). Actually, in this case

$$a(u)=(a_0-\Gamma b_0)-\Gamma\tilde{b}(u)=a_0(1-\Gamma\Gamma_{\text{вх}})+\Gamma\tilde{b}(u);\ a_0=c_0-\Gamma b_0;$$

$$\tilde{a}(u)=a_0\frac{1-\Gamma\Gamma_{\text{вх}}}{1-\Gamma\tilde{s}(u)};\qquad \tilde{b}(u)=a_0\frac{1-\Gamma\Gamma_{\text{вх}}}{1-\Gamma\tilde{s}(u)}\tilde{s}(u);$$

$$\vec{F}(\vartheta,\ \varphi,\ \Gamma)=a_0\frac{1-\Gamma\Gamma_{\text{вх}}}{1-\Gamma\tilde{s}(\kappa d\cos\vartheta)}\vec{f}_0^{(c)}(\vartheta,\ \varphi). \tag{17a}$$

If the oscillator is matched with the wave impedance of the feeder ($\Gamma_0=0$), a_0 is independent of the load in the feeders of the passive elements. When $a_0=1$ (volts/meter), we designate the directivity pattern corresponding to this case as

$$\vec{f}_0^{(н)}(\vartheta,\ \varphi)=\frac{1-\Gamma\Gamma_{\text{вх}}}{1-\Gamma\tilde{s}(\kappa d\cos\vartheta)}\vec{f}_0^{(c)}(\vartheta,\ \varphi). \tag{17b}$$

When $|\Gamma S(u)|<<1$, which corresponds to a system of *fairly weakly coupled* and well matched radiators ($|S_p|<<1;\ p=0,\pm 1\ldots$), or the case of near-wave loads ($|\Gamma|<<1$), instead of (16d) and (17b), we obtain approximately

$$\Gamma_{\text{вх}}\simeq s_0+2\Gamma\sum_{p=1}^{\infty}s_p^2; \tag{18a}$$

$$\vec{f}_0^{(н)}(\vartheta,\ \varphi)\simeq\vec{f}_0^{(c)}(\vartheta,\ \varphi)\ 1-\Gamma[\tilde{s}(\kappa d\cos\vartheta)-s_0]. \tag{18b}$$

As follows from expressions (18a,b), in the case of weak cross-coupling the directivity pattern of a radiator in the system $\vec{f}_0^{(H)}(\vartheta,\phi)$ and the coefficient of reflection at its input Γ_{BX} in the load function in the feeders of the passive elements are of the first and second order of smallness, respectively, with respect to the coupling coefficients.

Let us also consider the case of equal-amplitude linear phased excitation of the radiators when

$$\mathcal{E}_p = |\mathcal{E}_0| e^{-ip\Phi}, \quad p = 0, \pm 1, \pm 2, \ldots,$$

where Φ is the phase difference between adjacent radiators.

In this case

$$\tilde{\mathcal{E}}(u) = 2\pi |E_0| \delta_{2\pi}(u-\Phi); \quad \tilde{c}(u) = \pi\kappa \sqrt{\frac{2}{\rho}}(1-\Gamma)\delta_{2\pi}(u-\Phi), \tag{19}$$

where $\delta_{2\pi}(u-\Phi)$ is a periodic delta-function [2].

Substituting (19) in (14), we obtain

$$a_p = \frac{1}{2}\kappa \sqrt{\frac{2}{\rho}}(1-\Gamma)\frac{e^{-ip\Phi}}{1-\Gamma\tilde{s}(\Phi)}, \quad b_p = a_p\tilde{s}(\Phi). \tag{20}$$

As might be expected, in this case the absolute values of a_p and b_p are independent of the number.

By analogy with [4], we define the actual coefficient of reflection at the input of an element in the array in question as the ratio[1]

$$\Gamma_D^{(p)} = \frac{b_p}{a_p}.$$

---

[1] Γ_D coincides with Γ_{BX} in an active radiator when all of the other radiators are passive.

As follows from (20),

$$\Gamma_D = \tilde{s}(\Phi)$$

regardless of the radiator number.

Since $|a_p|$ and $|b_p|$ in this case are independent of the element number, the energy balance for the entire array is equivalent to the energy balance of a single radiator, i.e.,

$$\frac{|b_p|^2}{|a_p|^2} = |\tilde{s}(\Phi)|^2 \leqslant 1;$$

consequently, the elements of the scattering matrix of a linear periodic system of arbitrary radiators are such that the Fourier series comprised of them does not exceed unity in absolute value.

Let us also consider briefly the case in which the internal impedances of the oscillators are different. In this case, system (1), (10) can be solved iteratively. It is natural to use the value of a_p and b_p as the null approximation in the absence of cross-coupling:

$$a_p^{(0)} = \frac{c_p}{1 - \Gamma_p s_0}; \quad b_p^{(0)} = s_0 a_p^{(0)}.$$

When this is done, it is easy to obtain the following expressions for the values of a_p, b_p in the αth approximation:

$$a_p^{(\alpha)} = \frac{1}{1 - \Gamma_p s_0}\left[c_p + \Gamma_p \sum_{\substack{q=-\infty \\ q \neq 0}}^{\infty} s_q a_{q+p}^{(\alpha-1)}\right],$$

$$b_p^{(\alpha)} = \frac{1}{1 - \Gamma_p s_0}\left[c_p s_0 + \sum_{\substack{q=-\infty \\ q \neq 0}}^{\infty} s_q a_{q+p}^{(\alpha-1)}\right]$$

$$(\alpha = 1, 2, \ldots; \quad p = 0, \pm 1, \pm 2, \ldots).$$

Obviously, when c_p changes evenly and the cross-coupling is weak, the iterative process will convert rapidly.

In the case of a planar array, introducing the dual Fourier series:

$$\tilde{\mathcal{E}}(u,v)=\sum_{n=-\infty}^{\infty}\sum_{p=-\infty}^{\infty}\mathcal{E}_{np}e^{-inu-ipv};\quad \tilde{c}(u,v)=\frac{1}{2}k\sqrt{\frac{\pi}{\rho}}(1-\Gamma)\tilde{\mathcal{E}}(u,v),$$

we can obtain the following expressions:

$$a_{np}=\frac{1}{4\pi^2}\int_{-\pi}^{\pi}\int_{-\pi}^{\pi}\frac{\tilde{c}(u,v)e^{-i(nu+pv)}\,dudv}{1-\Gamma\tilde{s}(u,v)};$$

$$b_{np}=\frac{1}{4\pi^2}\int_{-\pi}^{\pi}\int_{-\pi}^{\pi}\frac{\tilde{c}(u,v)\tilde{s}(u,v)e^{-i(nu+pv)}\,dudv}{1-\Gamma\tilde{s}(u,v)},$$

$$\Gamma_{BX}=\frac{\displaystyle\int_{-\pi}^{\pi}\int_{-\pi}^{\pi}\frac{\tilde{s}(u,v)\,dudv}{1-\Gamma\tilde{s}(u,v)}}{\displaystyle\int_{-\pi}^{\pi}\int_{-\pi}^{\pi}\frac{dudv}{1-\Gamma\tilde{s}(u,v)}}=\frac{1}{\Gamma}\left|1-\frac{4\pi^2}{\displaystyle\int_{-\pi}^{\pi}\int_{-\pi}^{\pi}\frac{dudv}{1-\Gamma\tilde{s}(u,v)}}\right|.$$

If the emf of the oscillators in the planar array have the same amplitudes and linear phases for both coordinates, i.e.,

$$\mathcal{E}_{np}=|\mathcal{E}|e^{-in\Phi-ip\Psi},$$

then by analogy with a linear array

$$\Gamma_{BX}=\tilde{s}(\Phi,\Psi),$$

$$0\leqslant|\tilde{s}(\Phi,\Psi)|\leqslant 1.$$

DIRECTIVITY PATTERN AND COEFFICIENT OF REFLECTION AT INPUT OF RADIATOR IN LINEAR ARRAY AS FEEDER LOAD VARIES

To illustrate the relationships obtained above, let us consider a linear array of horns (Fig. 3) with a single active radiator (horns polarized perpendicular to the axis of the array); $d=\frac{5}{8\lambda}$.

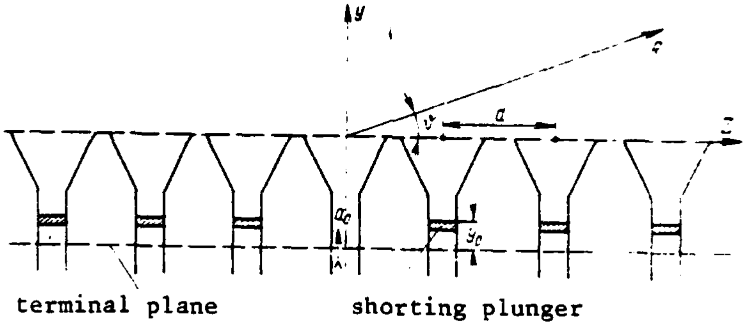

Fig. 3.

We shall use movable shorting plungers spaced at equal distances from the terminal sections as the loads in the feeders of the passive radiators. The coefficient of reflection from the loads (in the terminal section)

$$\Gamma = -e^{-i2\Psi}, \tag{21}$$

where $\Psi = \frac{2\pi y_0}{\lambda_g}$ is the electrical distance from the terminal section to the plunger. As has been established experimentally, the elements of the scattering matrix in such an array are approximated well by the relationships[1]:

$$|s_p|_{(\partial б)} = -[21+6(|p|-1)], \quad p = \pm 1, \pm 2, \ldots \tag{22a}$$

---

[1] For definition, the terminal plane is selected such that arg $s_{\pm 1}=0$.

$$\arg s_p = -(|p|-1)\kappa d, \quad p = \pm 1, \pm 2, \ldots, \tag{22b}$$

$$s_0 = 0,129\, e^{i194^\circ}. \tag{22c}$$

The scattering function $\tilde{s}(u)$ corresponding to (22a,b,c) can be represented as

$$\tilde{s}(u) = s_0 + s_1 \left\{ \frac{1}{e^{-iu} - \frac{1}{2} e^{-i\kappa d}} + \frac{1}{e^{iu} - \frac{1}{2} e^{-i\kappa d}} \right\}.$$

Figure 4 shows the representation of s(u) of the complex plane.

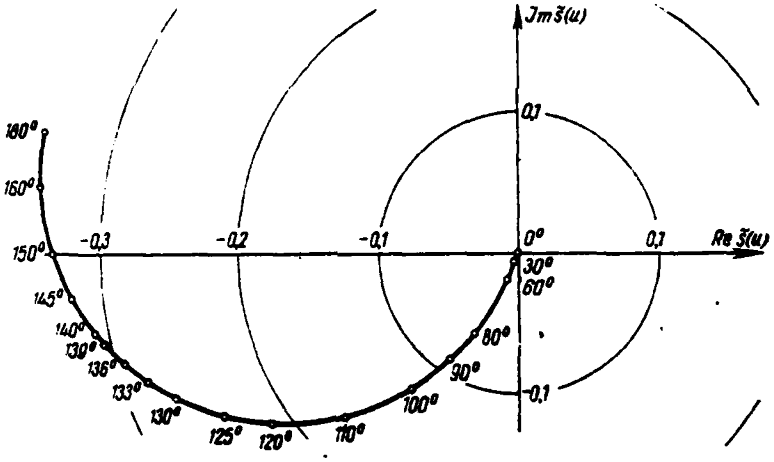

Fig. 4.

As follows from (17b), the deformation of the directivity pattern of the active radiator is characterized by the function

$$M(u, \psi) = \frac{f_0^{(\text{н})}(\vartheta, \varphi)}{f_0^{(c)}(\vartheta, \varphi)} = \frac{1 - \Gamma\Gamma_{\text{вх}}}{1 - \Gamma\tilde{s}(u)}; \quad u = \kappa d \cos\vartheta. \tag{23}$$

For the case of shorting plungers in the passive channels, we obtain the following on the basis of (21) and (23):

$$|M(u,\psi)| = \sqrt{\frac{1+|\Gamma_{вх}|^2+2|\Gamma_{вх}|\cos(2\psi+\arg\Gamma_{вх})}{1+|\tilde{s}(u)|^2+2|\tilde{s}(u)|\cos[2\psi+\arg\tilde{s}(u)]}}, \tag{24a}$$

$$\Psi(u,\psi) = \arg M(u,\psi) = \operatorname{arc\,tg}\frac{|\Gamma_{вх}|\sin(2\psi-\arg\Gamma_{вх})}{1-|\Gamma_{вх}|\cos(2\psi-\arg\Gamma_{вх})} - \operatorname{arc\,tg}\frac{|\tilde{s}(u)|\sin[2\psi-\arg\tilde{s}(u)]}{1-|\tilde{s}(u)|\cos[2\psi-\arg\tilde{s}(u)]}. \tag{24b}$$

The complex coefficient of reflection at the input of an active radiator in three-term approximation to the series (18a)

$$\Gamma_{вх}(\psi) \simeq s_0 + 2\Gamma s_1^2 = s_0 - 2s_1^2 e^{-i2\psi}. \tag{25}$$

The corresponding rigorous expression *obtained* in the Appendix reduces to the following form after a series of transformations:

$$\Gamma_{вх} = \frac{s_0 + (A-1)\frac{s_1}{z}}{1 - A\frac{\Gamma s_1}{z}}, \tag{26a}$$

where

$$A = \left[1 + 4\Gamma\left(\frac{s_1}{a-\frac{1}{z}} - \frac{s_0}{2}\right) + 4\Gamma^2\left(\frac{\frac{s_1^2}{z} - s_0 s_1}{z-\frac{1}{z}} + s_0^2\right)\right]^{-\frac{1}{2}} \tag{26b}$$

where the branch corresponding to ReA>0 should be used in the expression A.

Figures 5 and 6 show plots of the absolute value and argument of the deformation function $M(u,\psi)$ which reflect the variation in the amplitude and phase patterns while the shorting pistons are moved in the passive channels.

It is interesting to note that when $\psi=45^\circ$ and 135°, the function $|M(u,\psi)\approx 1$. so that the pattern of the radiator in an array with shorting plungers is close to the pattern of a radiator in an array with waveguide loads. This is explained by the fact that the region of maximum values of $|\tilde{s}(u)|$ corresponds to arg $\tilde{s}(u)\simeq\pi$.

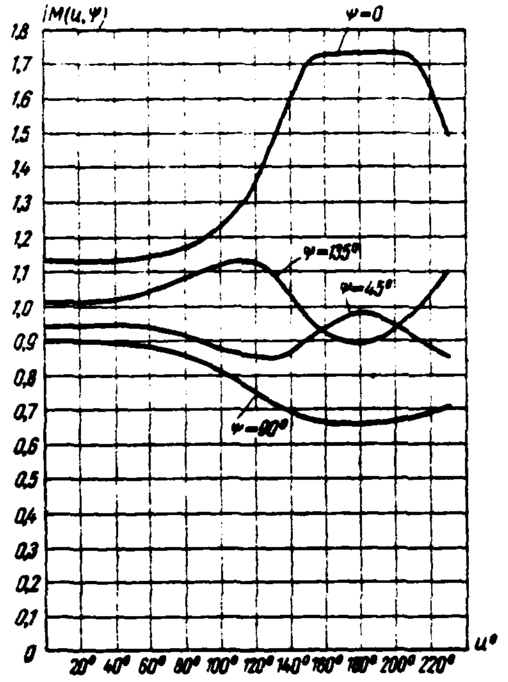

Fig. 5.

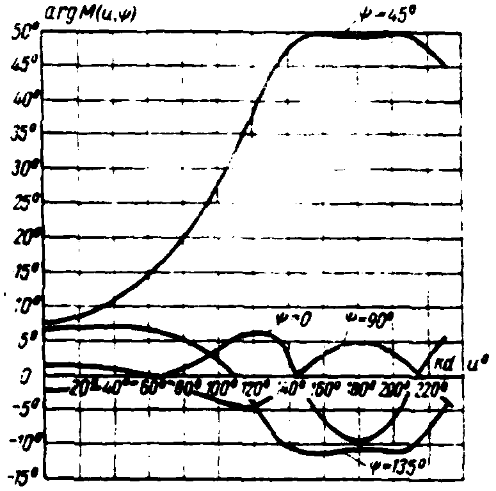

Fig. 6.

Figure 7 shows the relationships between $|\Gamma_{BX}(\psi)|$ and arg $\Gamma_{BX}(\psi)$ calculated on the basis of (22a-d), (25) and (26a,b). Their comparison with Figs. 5 and 6 shows that variation in the loads in the passive channels has a more significant influence on the directivity pattern, and has a relatively weak effect on the coefficient of reflection at the input of the active element. This fact agrees with formulas (18a and b). It should also be noted that the order of the quantities Γ_{BX} calculated by formulas (25) and (25a,b) coincides. The difference between the curves in Fig. 7 is explained by the fact that formula (26a,b) allows for the influence of the loads in the feeders of all of the radiators while formula (25) considers the influence of the loads in only

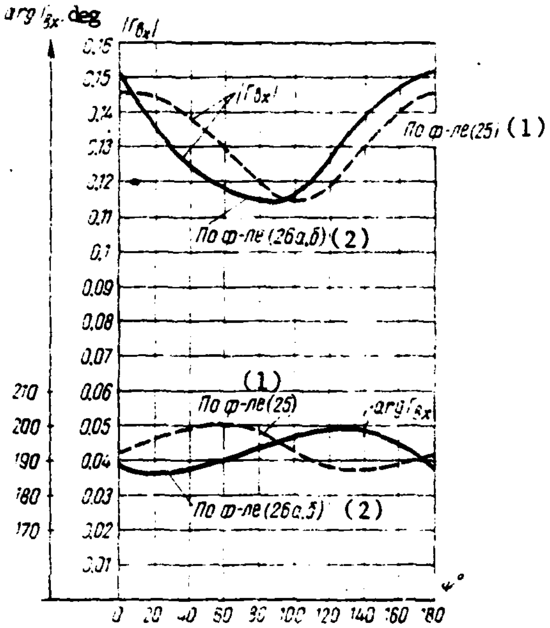

Fig. 7.

Key: (1) by formula (25); (2) by formula (26 a,b).

the feeders serving the closest ($n=\pm1$) radiators.

APPENDIX

Substituting the variable $z=e^{iu}$, we obtain

$$\tilde{s}(-i\ln z)=s(z)=s_0+s_1\left(\frac{1}{z-\varkappa}+\frac{z}{1-\varkappa z}\right),$$

where

$$\varkappa=\frac{1}{2}e^{-i\kappa d}.$$

Finding Γ_{BX} consists of calculating the contour integral

$$J(\Gamma)=\frac{1}{2\pi}\int_{-\pi}^{\pi}\frac{du}{1-\Gamma\tilde{s}(u)}=\frac{1}{2\pi i}\oint_{C}\frac{dz}{z[1-\Gamma s(z)]},$$

where C is a circle of unit radius with center at the point z=0.

Performing simple transformations and using the theory of residues, the following expressions can be obtained for J(Γ):

$$J(\Gamma) = -\left(\frac{\alpha}{\eta}\right)\left[1 - \frac{(z_1-\alpha)\left(\frac{1}{\alpha} - z_1\right)}{z_1^2 - 1}\right], \text{ if } |z_1| < 1;$$

$$J(\Gamma) = -\left(\frac{\alpha}{\eta}\right)\left[1 + \frac{(z_2-\alpha)\left(\frac{1}{\alpha} - z_2\right)}{z_2^2 - 1}\right], \text{ if } |z_2| < 1;$$

where

$$z_1 = \xi + \sqrt{\xi^2 - 1}; \quad z_2 = \xi - \sqrt{\xi^2 - 1}, \quad \xi = \frac{\gamma}{2\eta}; \quad z_1 z_2 = 1;$$

$$\gamma = 2\alpha\Gamma s_1 + (1 - \Gamma s_0)(1 - \alpha^2); \quad \eta = \Gamma(s_1 - s_0\alpha) + \alpha.$$

It can be shown that for the linear array considered in the preceding section $|z_1|<1$, so that after simple transformations we obtain

$$J(\Gamma) = z_1\left(\frac{\alpha}{\eta}\right)\left[\frac{2z_1 - \left(\alpha + \frac{1}{\alpha}\right)}{z_1^2 - 1}\right].$$

Then the expression for Γ_{BX} takes on the appearance:

$$\Gamma_{BX} = \frac{1}{\Gamma}\left[1 - \frac{1 - \Gamma\left(s_0 - \frac{s_1}{\alpha}\right)}{1 + \frac{(z_1-\alpha)\left(z_1 - \frac{1}{\alpha}\right)}{z_1^2 - 1}}\right].$$

LITERATURE

1. Справочник по волноводам. Перевод с английского под ред. Я. Н. Фельда. «Советское радио», 1952, стр. 111.

2. Фельд Я. Н. «Падение электромагнитных волн на двойные бесконечные решетки» ДАН СССР, 1956, т. 107, № 1, стр. 71.

3. Антенны сантиметровых волн. Часть I. Пер. с англ. под ред. Я. Н. Фельда. «Советское радио», 1950.

4. Hannan P. W. «The Element—Jain Paradox for a Phased—Array Antenna» IEEE Trans, v. AP-12, 1964, № 4 pp. 423—433.

EXCITATION OF SURFACE WAVES NEAR EDGE OF HOLLOW DIELECTRIC WEDGE

N.G. Khrebet

This article considers the problem of excitation of surface waves near the edge of a hollow dielectric wedge occurring when struck by a planar electromagnetic wave.

STATEMENT OF PROBLEM AND DERIVATION OF GENERAL FORMULAS

Let a hollow dielectric wedge consisting of two semi-infinite plane-parallel plates of equal thickness be struck by a plane electromagnetic wave polarized such that the electrical ($\vec{E}$) or magnetic ($\vec{H}$) field vector is parallel to the edge of the wedge. We shall assume that the edge of the wedge is not sharp, but represents the two contiguous ends of the plates comprising the wedge (Fig. 1). The surface waves are excited by the electrical and magnetic currents induced by the incident plane wave on the outside surface of the end of each wall of the wedge. Disregarding leakage of currents from one end to the other, we can reduce the problem in question to that of excitation of surface waves on a semi-infinite dielectric sheet, and write the solution for the wedge as the superimposition of the solutions for each wall.

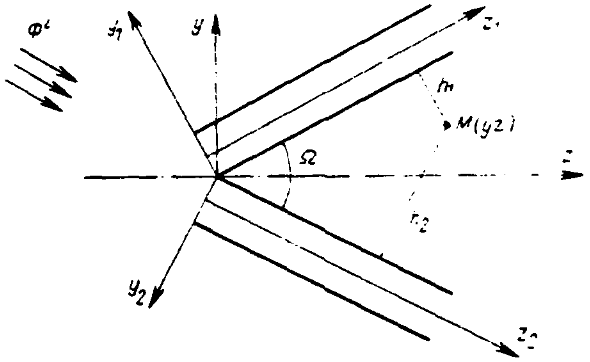

Fig. 1.

From the viewpoint of the practical applicability of the final results, this approximation is fully acceptable.

Considering the above, let us consider the problem of the excitation of surface waves on a semi-infinite dielectric plate with thickness of 2d.

In the rectangular system of coordinates shown in Fig. 2, the field of the plane wave incident on the plate is written as

$$\vec{\Phi}^i = \vec{i}_x \Phi_0^i \, e^{-i\kappa_0 (\overrightarrow{n_0 r})}, \tag{1}$$

where $\vec{\Phi}$ is the field vector parallel to the edge of the wedge. The currents induced by wave (1) on the surfaces of the plate produce a diffraction field [1], and we shall not be considering them. That portion of the currents which is induced on the inside surface of the end of the plate is the source of the surface waves. The number of types of waves excited on a plate depend upon its thickness [2]. Without losing generality, we shall limit ourselves to a plate whose thickness does not exceed one-half of a wavelength:

$$\frac{2d}{\lambda} \leqslant \frac{0.5}{\sqrt{\varepsilon - 1}}, \tag{2}$$

where ε is the dielectric permeability of the material of the plate.

Fig. 2.

Only the "primary" type of surface wave can propagate along such a plate, i.e., a wave for which there are no limitations on plate thickness (for more detail cf. [2]). The nature of the surface wave excited depends upon the polarization of the incident plane wave: a perpendicularly polarized plane wave will excite a surface H-wave, since in this case the magnetic vector $\vec{H}$ will have a z-component; analogously, a parallel polarized plane wave will excite a surface E-wave, since in this case the vector $\vec{E}$ will have the z-component.

Since the discussion and exposition are the same for calculating $\vec{H}$- and $\vec{E}$-waves, we shall limit ourselves to calculating the surfaces of an H-wave, presenting the results for the E-wave as well at the end. The currents induced on the inside surface of the end by an incident perpendicularly polarized wave will be

$$\vec{I}_e = [\vec{H}_{\text{npow}}\vec{i}_z]; \quad \vec{I}_m = -[\vec{E}_{\text{npow}}\vec{i}_z]. \tag{3}$$

where $E_{\text{прош}}$ and $H_{\text{прош}}$ are the field vectors of the plane wave passing through the end:

$$\vec{E}_{\text{прош}} = \vec{i}_x t_{\perp} E_0 e^{-ik_{д}(\vec{n}_1 \vec{r})}; \quad \vec{H}_{\text{прош}} = \frac{1}{Z_{д}} [\vec{n}_1 \vec{E}_{\text{прош}}]. \qquad (4)$$

Here $t_{\perp}$ is the Fresnel coefficient of passage (with the subscript indicating polarization);E_0 is the amplitude of the incident wave; $\vec{n}_1$ is the unit vector in the direction of propagation of the wave which has passed through; $k_{Д}$, $Z_{Д}$ are the wave number and wave impedance of the plane wave in a dielectric; $\vec{r}$ is the radius vector of the observation point ($\vec{r}=\vec{i}_y y$).

In the general case, the field of a surface wave is the superimposition of two waves propagating in opposite directions. In our case there are no conditions to generate the reverse wave. Therefore,

$$\vec{E}^h_{\text{пов}} = a^h_+ \vec{E}^h_+; \quad \vec{H}^h_{\text{пов}} = a^h_+ \vec{H}_+ \qquad (5)$$

(the superscripts h and e designate H- or E-waves, respectively). We shall use Lorenz' lemma to calculate the amplitude a^h_+:

$$\oint_S \{[\vec{E}_1 \vec{H}_2] - [\vec{E}_2 \vec{H}_1]\} d\vec{S} = \int_V \{\vec{I}_e \vec{E}_2 - \vec{I}_\mu \vec{H}_2\} dV. \qquad (6)$$

where $\vec{E}_1$ and $\vec{H}_1$ is the field generated by currents $\vec{I}_e$, $\vec{I}_\mu$; $\vec{E}_2 \vec{H}_2$ is an arbitrary auxiliary field; V is the space in which the currents are concentrated; S is a closed surface surrounding space V. We shall understand the vectors $\vec{E}_1$, $\vec{H}_1$ in equation (6) to be the field components of the sought surface wave propagating in the positive direction:$\vec{E}_1 = a_+ \vec{E}_+$;$\vec{H}_1 = a_+ \vec{H}_+$. We shall use as auxiliary vectors $\vec{E}_2$ and $\vec{H}_2$ the field vectors of the surface wave propagating in the negative direction: $\vec{E}_2 = a_- \vec{E}_-$; $\vec{H}_2 = a_- \vec{H}_-$. As a result, we obtain the following from equation (6):

$$a_-^h = \frac{\int_V \{\vec{I}_e\vec{E}_- - \vec{I}_\mu\vec{H}_-\}\, dV}{\oint_S \{[\vec{E}_+\vec{H}_-] - [\vec{E}_-\vec{H}_+]\}\, d\vec{S}} \qquad (7)$$

where the currents $\vec{I}_e$ and $\vec{I}_\mu$ are defined by (3). In our case, the currents $\vec{I}_e$ and $\vec{I}_\mu$ are surface currents which occupy a narrow band along the y axis, and an infinite band along the x axis (the end of the plate). Considering that the currents and fields are independent of the x coordinate, we obtain the linear integral $\left(\int_V \rightarrow \int_{-d}^{d}\right)$. in the numerator of expression (7) instead of a volumetric integral. We shall use as the closed surface S the plane $S_\perp$ coinciding with the end plane, and the surface S' which extends the plane $S_\perp$ to a closed surface at infinity. The integral taken over S' will be zero because of the attenuation at infinity of the surface wave. The integral taken over the plane $S_\perp$ becomes linear because the fields are independent of the x coordinate. As a result, we obtain (omitting the subscript + for amplitude)

$$a^h = \frac{\int_{-d}^{d} \{\vec{I_e E_-} - \vec{I}_\mu\vec{H}_-\} dy}{\left(\int_{-\infty}^{-d} + \int_{-d}^{d} + \int_{d}^{\infty}\right)\{[\vec{E}_+\vec{H}_-] - [\vec{E}_-\vec{H}_+]\}\vec{i}_z\, dy}. \qquad (8)$$

The integral in the denominator of (8) is separated because the structure of the surface waves inside and outside the plate is different.

In order to define this structure, we must solve the wave equation for a wave propagating along the plate using boundary conditions requiring that the tangential field components on its surfaces be equal.

These calculations are given in [2]; this is the final result:

$$\vec{E}^h_+ = \vec{i}_x E^h_+ = \vec{i}_x \begin{cases} -iC\kappa_{Д}Z_{Д}\nu\cos(\nu y)e^{-i\gamma z} - \text{inside plate,} \\ \pm iA\kappa_0 Z_0 \varkappa e^{\mp\varkappa y}e^{-i\gamma z} - \text{outside plate,} \end{cases} \tag{9}$$

$$\vec{H}^h_+ = -\vec{i}_y H_{y+} + \vec{i}_z H_{z+}, \tag{10}$$

where

$$H^h_{y+} = \begin{cases} \dfrac{\gamma}{\kappa_{Д}Z_{Д}} E^h_+ - \text{inside plate} \\ \dfrac{\gamma}{\kappa_0 Z_0} E^h_+ - \text{outside plate} \end{cases} \tag{11}$$

$$H^h_z = \begin{cases} C\nu^2\sin(\nu y)e^{-i\gamma z} - \text{inside plate;} \\ \mp A\varkappa e^{\mp\varkappa y}e^{-i\gamma z} - \text{outside plate.} \end{cases} \tag{12}$$

The fields $\vec{E}^h_-$ and $\vec{H}^h_-$ are obtained by changing the sign in the exponent in formulas (9) and (10). The following notation is introduced in formulas (9)-(12):

$$\varkappa = \sqrt{\gamma^2 - \kappa_0^2}, \quad \nu = \sqrt{\kappa_{Д}^2 - \gamma^2}, \tag{13}$$

where γ is the propagation constant of the surface wave calculated from the transcendental equation

$$\varkappa = \nu\,\mathrm{tg}(\nu d). \tag{14}$$

A and C are coefficients which are related by the following condition which follows from the boundary conditions on the surfaces of the plane:

$$\frac{A}{C} = -\frac{\nu^2}{\varkappa}\sin(\nu d)\,e^{\varkappa d} \tag{15}$$

The upper symbol in formulas (9)-(12) refers to the upper half-space (y>d), while the lower refers to the lower half-space (y<-d).

Substituting the currents (3) and fields (9)-(12) in formula (8), after the necessary transformations we obtain the following expression for the sought amplitude:

$$a = -\frac{i\,e^{\text{[illegible]}}}{Z_0 k\,\text{[illegible]}}\,q\,\text{[illegible]} \qquad (16)$$

where

$$q_0 = t_{\perp} E_0 \frac{\text{[illegible]}}{2\frac{\sin \gamma d}{\gamma d}\,\text{[illegible]}} \qquad (17)$$

$$\xi = d(\gamma - k_0 \sin \Theta'),$$
$$\xi' = d(\gamma + k_0 \sin \Theta')$$

(Θ' -- angle of incidence of plane wave on end counting from its normal).

Analogous calculations for a surface E-wave produce the following result:

$$a = \frac{-i Z_0}{4 k_0\,\text{[illegible]}}\, e^{\text{[illegible]}}\, q_{0\parallel}. \qquad (18)$$

where $q_{0\parallel}$ is obtained from formula (17) by substituting $t_{\perp} \rightarrow t_{\parallel}$; $E_0 \rightarrow H_0$ ($t_{\parallel}$ Fresnel coefficient of passage for parallel polarization), and the propagation constant γ is found from the equation

$$\varepsilon\varkappa = \gamma\,\mathrm{tg}(\gamma d). \qquad (19)$$

Figure 3 shows plots of the relative propagation constant γ/k_0 as a function of plate thickness for different ε calculated using formulas (14) and (19). Substituting in the first expression in (5) the value found for the amplitude (16) and the value of the field vector E_+^h from (9), considering equations (14) and (15), we obtain the following expression for the electrical field of the surface H-wave:

$$\vec{E}^h_{\Gamma B} = a^h \vec{E}^h_+ = \vec{i}_x \left| \begin{array}{l} q_0 \dfrac{e^{-\varkappa|y|}}{e^{-\varkappa d}} e^{-i\gamma z} \text{— outside plate,} \\ q_0 \dfrac{\cos(\nu y)}{\cos(\nu d)} e^{-i\gamma z} \text{— inside plate.} \end{array} \right. \qquad (20)$$

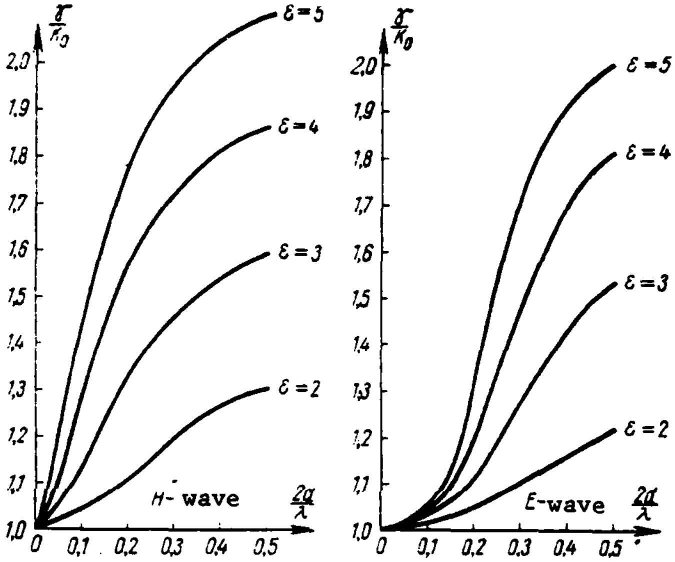

Fig. 3

We can also obtain expressions for the magnetic vector component of the H-wave from formulas (11), (12) and (16). In particular, we obtain the following from (11) for the y-component (which we will need below):

$$H_y^h = a^h H_{y+}^h = \left\{ \begin{array}{l} q_{0\perp} \dfrac{\gamma}{\kappa_0 Z_0} \dfrac{e^{-\varkappa|y|}}{e^{-\varkappa d}} e^{-i\gamma z} \text{— outside plate,} \\ q_{0\perp} \dfrac{\gamma}{\kappa_д Z_д} \dfrac{\cos(\nu y)}{\cos(\nu y)} e^{-i\gamma z} \text{— outside plate.} \end{array} \right. \qquad (21)$$

Expressions for the field components of the surface E-wave (excited by parallel polarized plane wave) can be obtained from formulas (20) and (21) by substituting

$$\vec{E}^{h}_{\text{пов}} \rightarrow \vec{H}^{e}_{\text{пов}}\ ;\quad H^{h}_{y} \rightarrow E^{e}_{y};\ q_{0\perp} \rightarrow q_{0\parallel};\ Z_0 \rightarrow \frac{1}{Z_0};\ Z_{\text{Д}} \rightarrow \frac{1}{Z_2}\ .$$

As a result, we obtain

$$\vec{H}^{e}_{\text{пов}} = \vec{i}_x \begin{cases} q_{0\parallel}\, \dfrac{e^{-\kappa y}}{e^{-\kappa d}}\, e^{-\gamma z} \text{ — outside plate,} \\ q_{0\parallel}\, \dfrac{\cos(gy)}{\cos(gd)}\, e^{-\gamma z} \text{ — inside plate,} \end{cases} \tag{22}$$

$$E^{e}_{y} = -\begin{cases} q_{0\parallel}\, \dfrac{\gamma}{\varepsilon_1} Z_0\, \dfrac{e^{-\kappa y}}{e^{-\kappa d}}\, e^{-\gamma z} \text{ — outside plate,} \\ q_{0\parallel}\, \dfrac{\gamma}{\varepsilon_2} Z_2\, \dfrac{\cos(gy)}{\cos(gd)}\, e^{-\gamma z} \text{ — inside plate.} \end{cases} \tag{23}$$

We recall that the expression for the excitation amplitude $q_{0\parallel}$ can be obtained from formula (17) by substituting $t_\perp \rightarrow t_\parallel$; $E_0 \rightarrow H_0$. the expression for the Fresnel passage coefficients $t_\perp$ and $t_\parallel$ is presented in [3]. It follows from formulas (20)-(23) that a surface wave propagating outside the plate attenuates along the y axis with attenuation constant $\kappa = k_0\sqrt{(\gamma/k_0)^2 - 1}$. Figure 4 shows the calculated curves, which indicate the distance from the plate $\frac{y'}{\lambda}$ at which the wave is attenuated by a factor of 10.

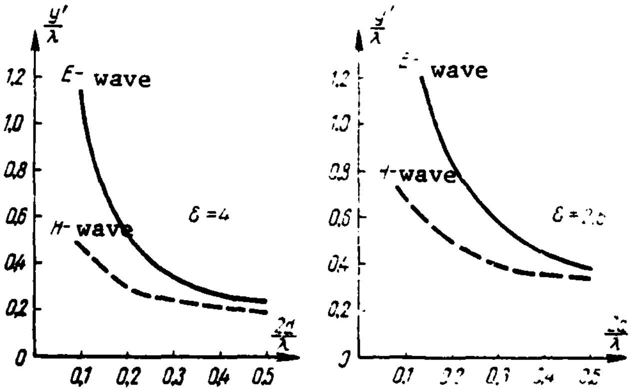

Fig. 4.

The nature of the relationship between the excitation amplitudes $q_{0\perp}$ and $q_{0\parallel}$ and the plate thickness, dielectric permeability ε and angle of incidence of the plane wave Θ'_0 on the end is illustrated by the curves in Figs. 5 and 6 which are calculated using formula (17) (the amplitude of the incident wave was taken to be unity in the calculations). It is apparent from these figures, in particular, that the amplitude of excitation is a strong function of the angle of incidence of the plane wave on the end of the plate: it is maximum for normal incidence on the end ($\Theta_0=\pi/2$), and minimum with normal incidence on the surface of the plate ($\Theta=0^\circ$). It should be noted that, as the experiments indicated, a surface wave, albeit very weak (approximately 2-3 orders of magnitude less than for $\Theta_0=\pi/2$) is also excited in the latter case. This divergence is a consequence of the fact that our calculations ignored leakage of surface currents from the surfaces of the plate to its end.

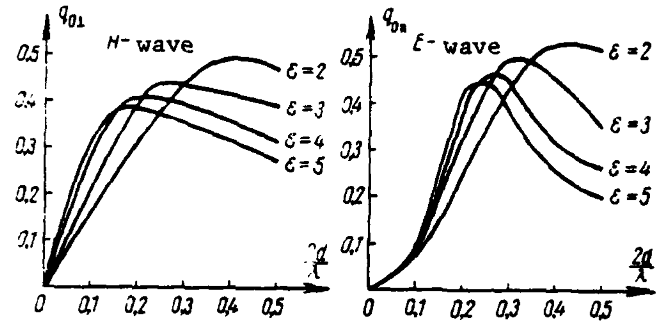

Fig. 5.

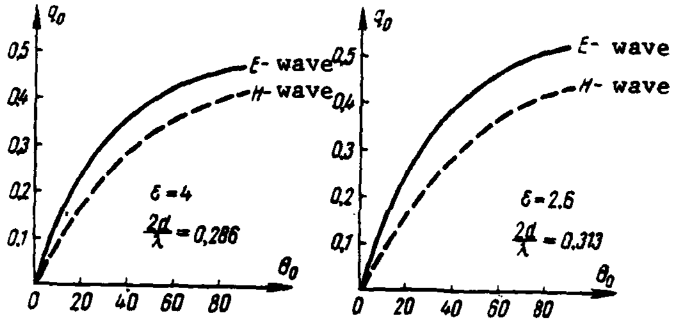

Fig. 6.

CONSIDERATION OF OHMIC LOSSES

The dielectrics which are used in practice have ohmic losses characterized by the imaginary part of the complex dielectric permeability $\varepsilon'=\varepsilon(1-i \tan \delta)$, where $\tan \delta$ is the tangent of the loss angle. Because of this, the surface wave propagation constant γ found from equations (14) and (19) will also be a complex quantity, the imaginary part of which will characterize the degree of attenuation of surface waves along the z axis. This part can be obtained from the aforementioned equations if we consider that the dielectric permeability which enters in is a complex quantity. Corresponding calculations (allowing for the smallness of $\tan \delta$) produce the following result:

$$\mathrm{Jm}\,(\gamma/\kappa_0)^e = \frac{\left(1-\frac{\sin x}{x}\right)\frac{\varepsilon}{2} + \frac{\sin x}{x}\,[\mathrm{Re}\,(\gamma/\kappa_0)]^2}{[\mathrm{Re}\,(\gamma/\kappa_0)]\left\{1-\frac{\sin x}{x}\,\frac{\varepsilon-1}{[\mathrm{Re}\,(\gamma/\kappa_0)]^2-1}\right\}}\tan\delta = \beta^e \tan\delta, \qquad (24)$$

$$\mathrm{Jm}\,(\gamma/\kappa_0)^h = \frac{\left(1+\frac{\sin x}{x}\right)\frac{\varepsilon}{2}}{[\mathrm{Re}\,(\gamma/\kappa_0)]\left\{1+\frac{\sin x}{x}\,\frac{\varepsilon-1}{[\mathrm{Re}\,(\gamma/\kappa_0)]^2-1}\right\}}\tan\delta = \beta^h \tan\delta, \qquad (25)$$

where $x=2\,\mathrm{Re}(\nu d)$; the superscripts e and h designate E- and H-waves, respectively. Figure 7 shows the curves calculated for the coefficients β^e and β^h as a function of the plate parameters. We are easily convinced that in the limiting cases ($d\to 0$ and $d\to\infty$), formulas (24) and (25) produce physically obvious results; when $d\to 0$ $\mathrm{Jm}(\gamma/k_0)\to 0$; when $d\to\infty$ $\mathrm{Jm}(\gamma/k_0)\to\frac{\sqrt{\varepsilon}}{2}\tan\delta$.

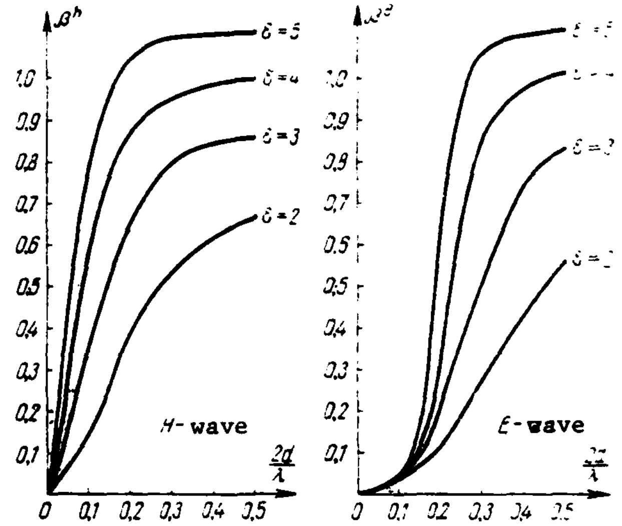

Fig. 7.

POWER TRANSFERRED BY SURFACE WAVE

Besides the change in the structure of the field near the plate surfaces, the influence of surface waves is also manifested in that part of the energy of the incident field is consumed in exciting them which, e.g., in the case of pointed barriers, results in a further reduction of their efficiency. Obviously, the portion of the energy lost in exciting surface waves is the same as the power which those waves carry.

Since in the present case the system is infinite along the x axis, we shall do the calculation for a band with unit dimension along this coordinate and infinite dimensions along the y coordinate. As we know, the power flux carried by an electromagnetic wave is characterized by the Umov-Poynting vector

$$\vec{S}=\frac{1}{2}\left[\vec{E}\vec{H}^{*}\right]. \qquad (26)$$

The power carried within the band we have selected

$$P_{\text{пов}} = \frac{1}{2}\int_{-\infty}^{\infty} (\vec{E}_{\text{пов}}\vec{H}^{*}_{\text{пов}})\,\vec{i}_z\,dy,$$

whence we obtain (27)

$$P^{h,e} = \frac{1}{2}\int_{-\infty}^{\infty} (E_{x,y}H^{*}_{y,x})\,dy.$$

where the first superscript refers to the H-wave, and the second *to the* E-wave. We shall limit ourselves to presenting the calculation for the H-wave, and present the results for the E-wave at the end as well.

Since the expressions for the field components of a surface wave are different inside and outside the plate, we shall calculate the integral in (27) separately for free space and for the dielectric:

$$P^{h} = P^{h}_{1} - P^{h}_{2} = \left[\int_{-\infty}^{-d} - \int_{d}^{\infty}\right](E_xH^{*}_{y})\,dy - \int_{-d}^{d}(E_xH^{*}_{y})\,dy. \tag{28}$$

Substituting in (28) the corresponding values of the fields E_x and H_y from (20) and (21), and introducing the coefficient $\eta^h = P_2/P_1$, which is equal to the power ratio inside and outside the plate, we obtain:

$$P^{h} = P^{h}_{1}(1 + \eta^{h}), \tag{29a}$$

where

$$P^{h}_{1} = \frac{1}{2}\frac{\gamma}{\kappa_0 Z_0 \varkappa}(q_{0-})^{2}, \tag{29b}$$

$$\eta^{h} = \left(\frac{\varkappa}{\gamma}\right)^{2}\frac{2\gamma d + \sin 2\gamma d}{2\sin^{2}\gamma d}. \tag{29c}$$

Analogous calculations for the E-wave produce

$$P^e = P_i^e(1 - \gamma_i^e)\,, \tag{30a}$$

where

$$P_i^e = \frac{1}{2}\,\frac{\gamma Z_0}{\varkappa_0 \gamma}\,(q_{011})^2; \tag{30b}$$

$$\gamma_i^e = 2\left(\frac{\varkappa}{\gamma}\right)^2 \frac{2\gamma d - \sin 2\gamma d}{2\sin^2 \gamma d}\,. \tag{30c}$$

Expressions (29) and (30) still do not give a clear representation of the energy lost in exciting the surface wave. We shall estimate this loss below while considering surface waves near a wedge.

CALCULATION OF SURFACE WAVE WITHIN HOLLOW WEDGE

We shall select a rectangular system of coordinates such that the x axis coincides with the touching ends of the plates forming the wedge and the z axis is directed along the bisector of the wedge (Fig. 1). Obviously, the field of the surface wave at a point M(y,z) lying within the wedge is the superimposition of the surface fields propagating along each of the walls of the wedge:

$$\vec{\Phi}(y,\,z) = \vec{\Phi}_1(h_1,z_1) + \vec{\Phi}_2(h_2,\,z_2). \tag{30}$$

where h_1 and h_2 represent the distance from the observation point to the corresponding wall along the normal to it, and z_1 and z_2 represent the distance along the surface of the wall from the end to the point at which the normal intersects the wall surface:

$$\begin{aligned} h_1 &= z\sin\Omega/2 - y\cos\Omega/2; \quad h_2 = z\sin\Omega/2 + y\cos\Omega/2, \\ z_1 &= z\cos\Omega/2 + y\sin\Omega/2; \quad z_2 = z\cos\Omega/2 - y\sin\Omega/2. \end{aligned} \tag{31}$$

where Ω is the angle of the wedge.

In particular, we shall have the following for the electrical vector of the H-wave [cf. formula (20)]:

$$E_x^h(y, z) =$$ [illegible] (32)

Let us estimate the portion of the energy consumed in exciting surface waves. In order to do this, we place a receiving antenna inside the wedge which has one linear dimension of 2a (along the y axis), with the other being a unit dimension (along the x axis). We shall compare the power carried by the surface waves with the power received by this antenna in the absence of the wedge. For simplicity, we shall assume that the incident plane wave propagates along the wedge bisector. Then the powers carried along each wall will be the same:

$$P^{\kappa\pi}_{\text{пов}} = 2P^{e,h}_{\text{пов}}.$$

The power received by the antenna when the plane wave strikes it is, as we know:

$$P_A = |\vec{S}|\frac{\lambda_0^2}{4\pi}G_0, \tag{33}$$

where $|\vec{S}|$ is the absolute value of Umov-Poynting vector (26), $G_0 = K\frac{4\pi}{\lambda^2}(2a \cdot 1)$ is the antenna gain, K is the reflector utilization factor. Substituting the values of $|\vec{S}|$ and G_0 in (33) and taking the ratio $P^{\text{КП}}_{\text{ПОВ}}/P_A$, we obtain

$$\frac{P^{e,h}_{\text{пов}}}{P_A} = \frac{2\gamma}{\gamma\kappa 2\pi\frac{2a}{\lambda}}\begin{cases}(q_{0\parallel})^2(1+\gamma_1^e),\\(q_{0\perp})^2(1+\gamma_1^h).\end{cases} \tag{34}$$

For a wedge with an apex angle of $\Omega=30^{\circ}$ and walls $2d/\lambda=0.286$ thick . dielectric permeability $\varepsilon=4$, expression (34) takes on the following numerical values for an E-wave:

$$\frac{P^{\text{n.i}\,e}_{103}}{P_A} \approx \begin{cases} 4\% \text{ for } 2d/\lambda=15;\ K=0.6, \\ 12\% \text{ for } 2d/\lambda=5;\ K=0.6. \end{cases}$$

Thus, the portion of the plane wave energy lost in exciting surface waves can in certain cases be considerable.

COMPARISON WITH EXPERIMENT

The formulas obtained for surface waves were checked experimentally by using a dipole to measure the electromagnetic field near the surface of a plane dielectric sheet with a plane electromagnetic wave incident upon it. The transmitting antenna (horn) and dipole were stationary with respect to one another. A vertical sheet of acrylic plastic was placed near the dipole and oriented so that the wave struck its end at an angle of $\Theta'=15^{\circ}$. A picture of the field was taken (with respect to power) immediately next to the surface of the sheet while the latter was moved evenly in a horizontal direction in the vertical plane such that the angle of incidence of the wave on the end and the distance from the dipole to the surface of the sheet remained constant. The variable quantity was thus the distance z from the end of the sheet to the dipole.

The dotted line in Fig. 8 shows the experimental curve. The field received by the dipole in the *absence of the sheet* was taken to be unity.

The solid line in the same figure shows the calculated curve for the total field allowing for diffraction (1) and the surface H-wave (in the experiments, the electrical vector of the incident wave field was parallel to the end):

$$|E_{\text{полн}}|^2 = |E_{\text{дифф}} - q_0 \; e^{-i\gamma z}|^2. \qquad (35)$$

The dot-and-dash line in Fig. 8 shows the calculated curve of the diffraction field $|E_{\text{дифр}}|^2$ disregarding the surface wave. It follows from comparing these curves that surface waves have a significant influence on the nature of the field near the sheet.

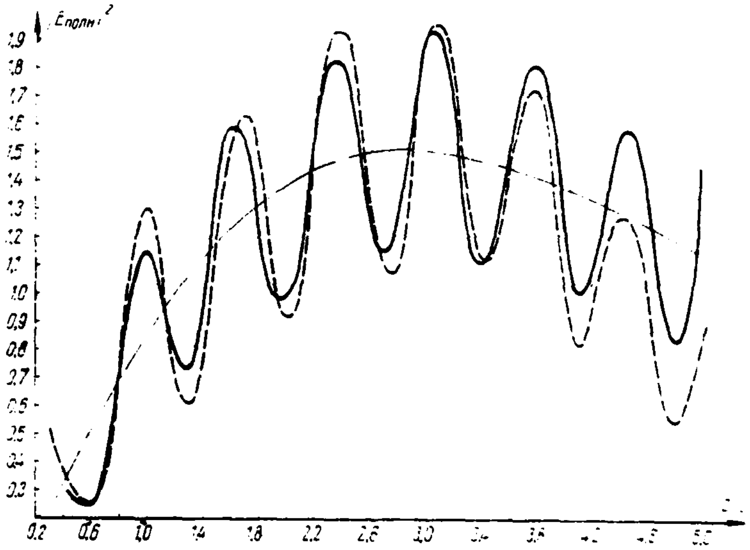

Fig. 8.

The good agreement between the experimental and calculated data indicate the validity of the surface wave formulas obtained in the present work.

LITERATURE

1. Пистолькорс А. А., Каплун В. А., Князев Л. Б. «Радиотехника и электроника», 1959, т. 4, вып. 6, стр. 911–912.

2. Фельд Я. Н., Бененсон Л. С. «Антенны сантиметровых и дециметровых волн». Часть II. Изд-во ВВИА им. Жуковского, 1959.

3. Обтекатели антенн. Пер. с англ. под редакцией А. И. Шпунтова. М., «Советское радио», 1950.

RADIATION OF ELECTRICAL DIPOLE LOCATED NEAR AN ELONGATED IDEALLY CONDUCTING SPHEROID ON AND PERPENDICULAR TO ITS LONG AXIS

D.A. Duplenkov, A.N. Kovalenko

The eigenfunction method is used to find a rigorous solution to the simplest problem of asymmetrical excitation of an elongated ideally conducting spheroid. A number of characteristics of the radiation are calculated for the secondary and total fields for the case of several spheroids with the same interfocal distance and different radial surface coordinates with different distances between the spheroid and the dipole. A solution regarding plane-wave diffraction is obtained for the special case of an infinite distance between the spheroid and the dipole.

INTRODUCTION

The problem of excitation of a body in the form of an elongated spheroid has in recent decades attracted the attention of many investigators interested in boundary problems in electrodynamics. This interest is understandable, since a system of elongated spheroidal coordinates makes it possible to isolate the variables in a scalar wave equation, consequently making it possible to use the eigenfunction method to solve the problem. On the other hand, a body in the form of an elongated spheroid has a significantly more complex form than a sphere or cylinder, for which solutions were obtained previously The articles which have been devoted to the problem of excitation of a body in the form of an elongated spheroid are numerous, and can be divided conditionally into two groups. The first group includes a number of fundamental works on the theory of spheroidal functions. This is mainly [1]-[4], as well as a number of other articles which consider more special problems of the theory of radial and angular spheroidal functions.

The second group includes the series of articles [5]-[16], which are devoted to solving various special cases of excitation. The basic work in this group is [5], which formulates in general form the solution to the problem of asymmetrical excitation of an elongated spheroidal body. The other articles examine the solution of narrower questions. However, except for [8], [9], all of these works, which consider the problem of diffraction of a plane wave incident on a spheroid along the long axis, involve the symmetrical method of excitation. Because of their complexity, problems of asymmetrical excitation have thus far remained practically unsolved even in the simplest special cases.

The present article is the first attempt to attain numerical results for the simple problem of asymmetrical excitation of an elongated ideally conducting spheroid. Excitation is done by means of an elementary electrical dipole placed on the long axis of the spheroid. The axes of the dipole and the spheroid are perpendicular to one another. The distance between the spheroid and the dipole may vary. In the special case for an infinite distance, a solution is obtained for the diffraction of a plane wave incident on the spheroid along its long axis.

SOLUTION

In [5], the problem of excitation of a body in the form of an elongated ideally conducting spheroid is solved in general form. It is shown that for an arbitrary system of exciting currents (for an arbitrary primary field), the problem of finding the coefficients of expansion of the secondary field into a series with respect to spheroidal functions reduces to solving an infinite system of algebraic equations.

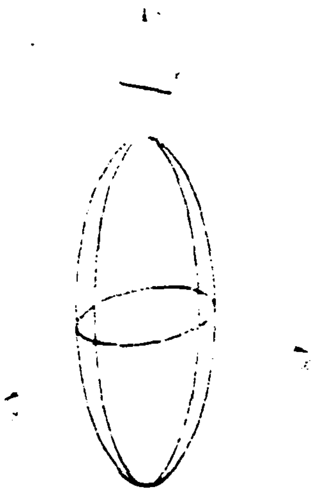

Fig. 1.

In solving the present special problem of excitation, in which a spheroidal body is excited by an elementary electrical dipole (Fig. 1), we shall use the general methodology developed in [5] as a basis. Since we are considering a special case of the general problem, it becomes possible to simplify significantly the mathematical apparatus.

First of all, the possibility for this simplification comes from specifying the field of the primary source. Therefore, we shall first consider the primary field of the dipole in a spheroidal coordinate system. The dipole is displaced from the coordinate origin, and located on the axis of the system with the axis of the dipole perpendicular to the axis of the system.

Since the Green function of the scalar equation is known [4], [14], the intensity of the source magnetic field can be calculated by the following formula [5]:

$$\bar{H} = \int \bar{j} \times \operatorname{grad}_q G \, dv \tag{1}$$

Here j is the volumetric density of the electrical current of the source.

$$G = \frac{1}{4\pi} \frac{e^{i\kappa r}}{r} = \frac{\kappa}{2\pi i} \sum_{m=0}^{\infty} \sum_{l=m}^{\infty} \frac{\varepsilon_m}{N_{ml}} S_{ml}(h, \eta) S_{ml}(h, \eta') \cos m(\varphi - \varphi') \times$$

$$\times \begin{cases} je_{ml}(h, \xi)\, he_{ml}^{(2)}(h, \xi') & \text{for } \xi < \xi' \\ he_{ml}^{(2)}(h, \xi)\, je_{ml}(h, \xi') & \text{for } \xi > \xi' \end{cases}$$ — Green function,

$S_{ml}(h, \eta)$ — angular spheroidal coordinates,

$je_{ml}(h, \xi)$ — radial spheroidal functions of the first sort,

$he(h, \xi)_{ml}^{(2)}$ — radial spheroidal frunctions of the fourth sort,

$N_{ml} = \int_{-1}^{+1} S_{ml}^2(h, \eta)\, d\eta$ — angular function standard,

$$\varepsilon_m = \begin{cases} 1 & \text{for } m = 0, \\ 2 & \text{for } m = 1, 2, 3, \ldots, \end{cases}$$

$h = \frac{\kappa d}{2}$ — parametric characterizing interfocal distance,

d — interfocal distance.

The symbol q *denotes* differentiation over the source points whose coordinates are designated with primes. The integration in expression (1) is done over the source points.

Substituting in expression (1) the expansion for Green's function and making a series of transformations, we obtain the following expressions for the Cartesian components of the magnetic field

$$H_\xi = \frac{\kappa}{2\pi i} \sum_{m=0}^{\infty} \sum_{l=m}^{\infty} \frac{\varepsilon_m}{N_{ml}} S_{ml}(h, \eta)\, h\, e^{(2)}_{ml}(h, \xi) \{a^1_{ml} \cos m\varphi + a^2_{ml} \sin m\varphi\},$$

$$H_\eta = \frac{\kappa}{2\pi i} \sum_{m=0}^{\infty} \sum_{l=m}^{\infty} \frac{\varepsilon_m}{N_{ml}} S_{ml}(h, \eta)\, h\, e^{(2)}_{ml}(h, \xi) \{b^1_{ml} \cos m\varphi - b^2_{ml} \sin m\varphi\}, \tag{2}$$

$$H_\varphi = \frac{\kappa}{2\pi i} \sum_{m=0}^{\infty} \sum_{l=m}^{\infty} \frac{\varepsilon_m}{N_{ml}} S_{ml}(h, \eta)\, h\, e^{(2)}_{ml}(h, \xi) \{c^1_{ml} \cos m\varphi + c^2_{ml} \sin m\varphi\}.$$

If we consider that in this case the outside electrical current has only an η-component and is assigned in the form of a δ-function, i.e., the volumetric current density can be expressed by the equation

$$j^э_\eta = \frac{I^э_\eta l_э \delta(\xi - \xi_э) \delta(\eta - 1) \delta(\varphi - 0)}{h_1 h_2 h_3}, \tag{3}$$

where $\xi = \xi_э$, $\eta = 1$, $\phi = 0$ are the dipole coordinates, the values of the coefficients entering into (2) are represented by the following formulas:

$$a^1_{ml} = \int_{v'} [j^э_\eta \operatorname{grad}\{S_{ml}(h, \eta')\, j\, e_{ml}(h, \xi') \cos m\varphi'\}]_x\, dv',$$

$$a^2_{ml} = \int_{v'} [j^э_\eta \operatorname{grad}\{S_{ml}(h, \eta')\, j\, e_{ml}(h, \xi') \sin m\varphi'\}]_x\, dv',$$

$$b^1_{ml} = \int_{v'} [j^э_\eta \operatorname{grad}\{S_{ml}(h, \eta')\, j\, e_{ml}(h, \xi') \cos m\varphi'\}]_y\, dv',$$

$$b^2_{ml} = \int_{v'} [j^э_\eta \operatorname{grad}\{S_{ml}(h, \eta')\, j\, e_{ml}(h, \xi') \sin m\varphi'\}]_y\, dv', \tag{4}$$

$$c^1_{ml} = \int_{v'} [j^э_\eta \operatorname{grad}\{S_{ml}(h, \eta')\, j\, e_{ml}(h, \xi') \cos m\varphi'\}]_z\, dv',$$

$$c^2_{ml} = \int_{v'} [j^э_\eta \operatorname{grad}\{S_{ml}(h, \eta')\, j\, e_{ml}(h, \xi') \cos m\varphi'\}]_z\, dv'.$$

When formulas (4) are used to calculate the coefficients $a^{1,2}_{m\ell}$, $b^{1,2}_{m\ell}$, $c^{1,2}_{m\ell}$, they all turn out to be zero except for $b^1_{0\ell}$ and $c^2_{1\ell}$. Substituting these values in formulas (2) and using the connection between the Cartesian and spheroidal components of the vector, we write the following expressions for the spheroidal components of the magnetic field of the dipole:

$$H_\xi = \frac{\kappa}{2\pi i}\frac{2l_\eta^3 l_\theta}{d}\sin\varphi\left\{-\frac{\xi\sqrt{1-\eta^2}}{\sqrt{\xi^2-\eta^2}}\sum_{l=0}^{\infty}\frac{\varepsilon_0}{N_{0l}}S_{0l}(h,\eta)\right.$$

$$\times\begin{vmatrix} h\,e_{0l}^{(2)}(h,\xi)\dfrac{\partial}{\partial\xi'}[j\,e_{0l}(h,\xi')]|_{\xi'=\xi_0} \\ j\,e_{0l}(h,\xi)\dfrac{\partial}{\partial\xi'}[h\,e_{0l}^{(2)}(h,\xi')]|_{\xi'=\xi_0}\end{vmatrix}$$

$$\left.-\frac{\eta\sqrt{\xi^2-1}}{\sqrt{\xi^2-\eta^2}}\frac{1}{\sqrt{\xi_0^2-1}}\sum_{l=1}^{\infty}\frac{\varepsilon_1}{N_{1l}}S_{1l}(h,\eta)\frac{l(l+1)}{2}\begin{vmatrix} h\,e_{1l}^{(2)}(h,\xi)j\,e_{1l}(h,\xi_0) \\ j\,e_{1l}(h,\xi)h\,e_{1l}^{(2)}(h,\xi_0)\end{vmatrix}\right\}, \qquad (5)$$

$$H_\eta = \frac{\kappa}{2\pi i}\frac{2l_\eta^3 l_\theta}{d}\sin\varphi\left\{\frac{\eta\sqrt{\xi^2-1}}{\sqrt{\xi^2-\eta^2}}\sum_{l=0}^{\infty}\frac{\varepsilon_0}{N_{0l}}S_{0l}(h,\eta)\right.$$

$$\times\begin{vmatrix} h^{(2)}e_{0l}(h,\xi)\dfrac{\partial}{\partial\xi'}[j\,e_{0l}(h,\xi')]|_{\xi'=\xi_0} \\ j\,e_{0l}(h,\xi)\dfrac{\partial}{\partial\xi'}[h\,e_{0l}^{(2)}(h,\xi')]|_{\xi'=\xi_0}\end{vmatrix} -$$

$$\left.+\frac{1}{\sqrt{\xi_0^2-1}}\frac{\xi\sqrt{1-\eta^2}}{\sqrt{\xi^2-\eta^2}}\sum_{l=1}^{\infty}\frac{\varepsilon_1}{N_{1l}}S_{1l}(h,\eta)\frac{l(l+1)}{2}\begin{Bmatrix} h\,e_{1l}^{(2)}(h,\xi)j\,e_{1l}(h,\xi_0) \\ j\,e_{1l}(h,\xi)h\,e_{1l}^{(2)}(h,\xi_0)\end{Bmatrix}\right\},$$

$$H_\varphi = -\frac{\kappa}{2\pi i}\frac{2l_\eta^3 l_b}{d}\cos\varphi\sum_{l=0}^{\infty}\frac{\varepsilon_0}{N_{0l}}S_{0l}(h,\eta)\begin{cases} h e_{0l}^{(2)}(h,\xi)\dfrac{\partial}{\partial\xi'}[j\,e_{0l}(h,\xi')]_{\xi'=\xi_0} \\ j\,e_{0l}(h,\xi)\dfrac{\partial}{\partial\xi'}[h\,e_{0l}^{(2)}(h_1\,\xi')]_{\xi'=\xi_0}.\end{cases}$$

The first line of the radial spheroidal functions in these formulas corresponds to the region $\xi>\xi_0$, and the second to $\xi<\xi_0$. We have thus solved the first part of the problem, which concerns finding the field of an elementary electrical dipole located at the point with coordinates $\xi=\xi_0$, $\eta=1$, $\phi=0$, i.e., we have found the primary field of the source. The expressions for the components of the primary field are characterized by a simple relationship with the coordinate ϕ , which significantly simplifies the solution to the second part of the problem, namely finding the coefficients of expansion of the secondary field, i.e., the field of the currents induced on the spheroid.

The field of the currents induced on an ideally conducting spheroid is represented in general field by expansions (2) as well, since these expansions were obtained for an arbitrary system of currents. In the special case, these may be surface currents on the spheroid. However, the coefficients a,b and c in this case are not defined by equations (4). They are unknown and must be defined from the boundary conditions on the surface of the spheroid [5]. The problem becomes that of solving an infinite system of algebraic equations for the sought coefficients. We note that the simple relationship between the primary field and the coordinate ϕ simplifies the problem significantly. Analysis shows that the only non-zero coefficients of expansion in expressions (2) will be b_{ok}^1, c_{1k}^2, a_{2k}^2 and b_{2k}^1 of the secondary field, where $a_{2k}^2=-b_{2k}^1$. The numerical values of these coefficients are determined from the following infinite system of algebraic equations, which is significantly simpler than that written in [5]:

$$2h^{(2)} e_{2\kappa}(h, \xi_0)\, \xi_0 a_{2\kappa}^2 - \sum_{l=0}^{\infty} \frac{1}{N_{0l}} h e_{0l}^{(2)}(h, \xi_0)\, b_{0l}^1 C_{l\kappa}^1$$

$$+ \sum_{l=1}^{\infty} \frac{2c_{1l}^2}{N_{1l}} h e_{1l}^{(2)}(h, \xi_0) \sqrt{\xi_0^2 - 1}\, A_{l\kappa}^1 =$$

$$= \frac{I_\eta^2 \kappa l_n}{h} \left[\sum_{l=0}^{\infty} \xi_0 \frac{1}{N_{0l}} j e_{0l}(h, \xi_0) \frac{\partial}{\partial \xi'} [h e_{0l}^{(2)}(h, \xi')]_{\xi' = \xi_0} C_{l\kappa}^1 - \right.$$

$$\left. - \sum_{l=1}^{\infty} \frac{1}{N_{1l}} \frac{\sqrt{\xi_0^2 - 1}}{\sqrt{\xi_0^2 - 1}} j e_{1l}(h, \xi_0)\, l(l+1)\, h e_{1l}^{(2)}(h, \xi_0) A_{l\kappa}^1 \right]; \qquad (6)$$

$$2 \frac{\partial}{\partial \xi} [\sqrt{\xi^2 - 1}\, h e_{2\kappa}^{(2)}(h, \xi)]|_{\xi = \xi_0} a_{2\kappa}^2 + \sum_{l=0}^{\infty} \frac{1}{N_{0l}} \frac{\partial}{\partial \xi} [\sqrt{\xi^2 - 1} \cdot$$

$$\times h e_{0l}^{(2)}(h, \xi)]_{\xi = \xi_0} b_{0l}^1 C_{l\kappa}^1 - \sum_{l=1}^{\infty} \frac{2c_{1l}^2}{N_{1l}} \frac{\partial}{\partial \xi} [\xi h e_{1l}^{(2)}(h, \xi)]_{\xi = \xi_0} B_{l\kappa}^1 =$$

$$= \frac{I_\eta^2 \kappa l_n}{h} \left\{ \sum_{l=0}^{\infty} \frac{1}{N_{0l}} \frac{\partial}{\partial \xi} [\sqrt{\xi^2 - 1}\, j e_{0l}(h, \xi)]_{\xi = \xi_0} \frac{\partial}{\partial \xi'} [h^{(2)} e_{0l}(h, \xi')]_{\xi' = \xi_0} C_{l\kappa}^1 + \right.$$

$$\left. + \sum_{l=1}^{\infty} \frac{1}{N_{1l}} \frac{1}{\sqrt{\xi_0^2 - 1}} \frac{\partial}{\partial \xi} [\xi j e_{1l}(h, \xi)]_{\xi = \xi_0} l(l+1)\, h e_{1l}^{(2)}(h, \xi_0) B_{l\kappa}^1 \right\};$$

$$-2\frac{\partial}{\partial\xi}\left[\sqrt{\xi^2-1}\,h^{(2)}e_{2\kappa}(h,\xi)\right]\Big|_{\xi=\xi_0} a^2_{2\kappa}-$$

$$+\sum_{l=0}^{\infty}\frac{1}{N_{0l}}\frac{\partial}{\partial\xi}\left[\sqrt{\xi^2-1}\,h\,e^{(2)}_{0l}(h,\xi)\right]\Big|_{\xi=\xi_0} b^1_{0l}C^1_{l\kappa}=$$

$$=\frac{I^3_\eta\,\kappa l_y}{h}\sum_{l=0}^{\infty}\frac{1}{N_{0l}}\frac{\partial}{\partial\xi}\left[\sqrt{\xi^2-1}\,j\,e_{0l}(h,\xi)\right]\Big|_{\xi=\xi_0}\frac{\partial}{\partial\xi'}\left[h e^{(2)}_{0l}(h,\xi')\right]\Big|_{\xi'=\xi_0}C^1_{l\kappa}\,.$$

The following notation is used here:

$$\begin{aligned}
A^1_{l\kappa}&=\int_{-1}^{+1}S_{1l}(h,\eta)\,S_{2\kappa}(h,\eta)\frac{\eta}{\sqrt{1-\eta^2}}\,d\eta,\\
B^1_{l\kappa}&=\int_{-1}^{+1}S_{1l}(h,\eta)\,S_{2\kappa}(h,\eta)\frac{\sqrt{1-\eta^2}}{\eta}\,d\eta,\\
C^1_{l\kappa}&=\int_{-1}^{+1}S_{0l}(h,\eta)\,S_{2\kappa}(h,\eta)\,d\eta
\end{aligned}\tag{7}$$

The expansions themselves for the field in this case (for the region $\xi>\xi_0$) take on the following form:

$$\begin{aligned}
H^{\text{вт}}_{\eta}&=\frac{I^3_x\,l\kappa^2}{2\pi\,ih}\sin\varphi\left\{-\frac{\eta\sqrt{\xi^2-1}}{\sqrt{\xi^2-\eta^2}}\sum_{l=2}^{\infty}\frac{2}{N_{2l}}S_{2l}(h,\eta)\,h\,e^{(2)}_{2l}(h,\xi)\,a^2_{2l}-\right.\\
&-\frac{\eta\sqrt{\xi^2-1}}{\sqrt{\xi^2-\eta^2}}\sum_{l=0}^{\infty}\frac{1}{N_{0l}}S_{0l}(h,\eta)\,h\,e^{(2)}_{1l}(h,\xi)\,b^1_{0l}+\\
&\left.+\frac{\xi\sqrt{1-\eta^2}}{\sqrt{\xi^2-\eta^2}}\sum_{l=1}^{\infty}\frac{2}{N_{1l}}S_{1l}(h,\eta)\,h\,e^{(2)}_{1l}(h,\xi)\,C^2_{1l}\right\},\\
H^{\text{вт}}_{\varphi}&=\frac{I^3_x\,l\kappa^2}{2\pi\,ih}\cos\varphi\left\{-\sum_{l=2}^{\infty}\frac{2}{N_{2l}}S_{2l}(h,\eta)\,h\,e^{(2)}_{2l}(h,\xi)\,a^2_{2l}+\right.\\
&\left.+\sum_{l=0}^{\infty}\frac{1}{N_{0l}}S_{0l}(h,\eta)\,h\,e^{(2)}_{0l}(h,\xi)\,b^1_{0l}\right\}.
\end{aligned}\tag{8}$$

Investigating the field in the far zone, i.e., where $\xi \to \infty$, we can simplify expressions (8). In order to do this, we use certain asymptotic representations for the radial spheroidal functions and assume that the spheroidal system of coordinates becomes spherical in this case. The final expressions for the summary field in the far zone take on the following form:

$$
\begin{aligned}
H_{\Theta}^{\text{сумм}} &= \frac{I_x^{э} l^{\kappa}}{4\pi i} \sin\varphi \frac{e^{-i\kappa r}}{r} \Bigg\{ e^{ih\xi_{g}\cos\Theta} - \frac{2}{h} \Bigg\{ -\cos\Theta \Bigg[\sum_{l=2}^{\infty} \frac{2}{N_{2l}} \times \\
&\times S_{2l}(h, \eta_l)\, e^{\frac{i(l+1)\pi}{2}} + \sum_{l=0}^{\infty} \frac{1}{N_{0l}} S_{0l}(h, \eta_l)\, e^{\frac{i(l+1)\pi}{2}} b_{0l}^{1} \Bigg] + \\
&+ \sin\Theta \sum_{l=1}^{\infty} \frac{2}{N_{1l}} S_{1l}(h, \eta_l)\, e^{\frac{i(l+1)\pi}{2}} c_{1l}^{2} \Bigg\} \\
H_{\varphi}^{\text{сумм}} &= \frac{I_x^{э} l^{\kappa}}{4\pi i} \cos\varphi \frac{e^{-i\kappa r}}{r} \Bigg\{ \cos\Theta\, e^{ih\xi_b \cos\Theta} + \\
&+ \frac{2}{h} \Bigg\{ - \sum_{l=2}^{\infty} \frac{2}{N_{2l}} S_{2l}(h, \eta_l)\, e^{\frac{i(l+1)\pi}{2}} a_{0l}^{2} \Bigg\} + \\
&+ \sum_{l=0}^{\infty} \frac{1}{N_{0l}} S_{0l}(h, \eta_l)\, e^{\frac{i(l+1)\pi}{2}} b_{0l}^{1} \Bigg\}.
\end{aligned}
\tag{9}
$$

The problem is thus in principle solved completely, since all of the necessary relationships have been obtained.

CALCULATION OF DIRECTIVITY PATTERNS

The calculation of directivity patterns using the formulas obtained above is divided naturally into several stages.

In the first stage, all of the functions which enter into system of algebraic equations (6) must be calculated. We are talking primarily about the spheroidal functions and their derivatives. This problem can be solved most simply by using tables of the coefficients of expansion of angular and radial functions with respect to adjoint Legendre polynomials and spherical Bessell and Neumann spherical functions, respectively [3]. This was the method used in the present work. However, significant difficulties are encountered on this simple path involving the poor convergence of the series for radial spheroidal functions. These can be overcome by using a certain recursive formula for the coefficients of expansion of angular spheroidal functions, as well as a recurrent formula for spherical Neumann functions. Operating with the sequences of the ratios of later members to earlier members and considering an extremely large number of members of the series, a computer can be used to obtain tables of spheroidal functions for those parameter values for which the coefficients of expansion are tabulated.

It is no less difficult to calculate the coefficients of (7) which represent integrals of the products of the angular spheroidal functions with certain additional factors. It is extremely difficult to calculate these coefficients, although it is simple in principle. Each spheroidal function must be represented in the form of an expansion with respect to adjoint Legendre polynomials, and each polynomial must be used in convoluted form. The result is finally obtained at an infinite series of integrals of step functions with certain coefficients which include the coefficients of expansion of the spheroidal functions.

After these additional calculations, it becomes possible to solve system (6), since all of the special functions which enter into it are represented numerically. Considering the fact that every other integral in (7) becomes zero, depending upon the numbers ℓ and k, it becomes possible to divide system of equations (6) into two infinite systems of algebraic equations for odd- and even-numbered sought coefficients, respectively. In practical calculations, the order of the system matrix must be limited. Modern computing technology allows us to deal freely with complex matrix up to order 80; however, in our case the computer cannot determine the order of the matrices being manipulated. The limiting factor is the table of spheroidal functions which, based on [3], cannot be calculated for numbers $\ell>8$. Finally, the highest possible order of the matrix of the system of linear algebraic equations for even coefficients is 12, and 9 for odd coefficients. Experience in doing this calculation has shown that this order of matrices provides more or less acceptable accuracy of solution only for bodies with extremely small electrical dimensions. Thus, in this stage the solution of two complex systems of algebraic equations allows us to find all of the necessary coefficients of expansion of the field a,b,c which enter into (8) and (9)

The last stage consists of calculating the components of the total and secondary fields of the system using equations (9). This calculation presents, in principle, no difficulties.

As examples, the directivity patterns of an elementary dipole with current $I_x^{Э}$ located in the plane $\phi=0$ near the elongated spheroid in Fig. 1 were calculated. The following parameters were used for the spheroid: $h=1$, $\xi_0=1.044$, 1,077, 1, 2, 2.0. The dipole was located on the axis of the spheroid with radial coordinates of $\xi_0=2.0$, 2.65, 4.22, ∞. The directivity patterns were calculated for the planes $\phi=0$ and $\phi=\pi/2$. Figures 2-7 show the calculated directivity patterns. In this manner, questions associated with variation in the directivity patterns as a function of the transverse dimensions of the spheroid were investigated to a certain extent, since variation in ξ_0 designates a change primarily in the transverse dimensions; the directivity characteristics as a function of the distance between the dipole and spheroid were also investigated.

CONCLUSION

The present work provides concrete results for the problem of asymmetrical excitation of an elongated ideally conducting spheroid. The basic analytical formulas are given along with a commentary on the difficulties involved in making specific calculations. The main limitation on using the developed apparatus to obtain a wide group of sufficiently precise numerical results for

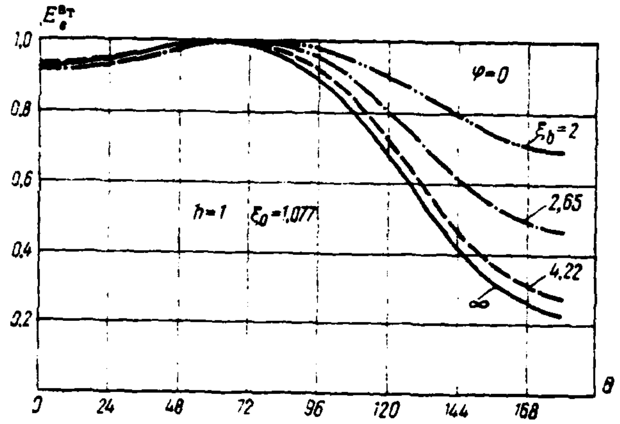

Fig. 2.

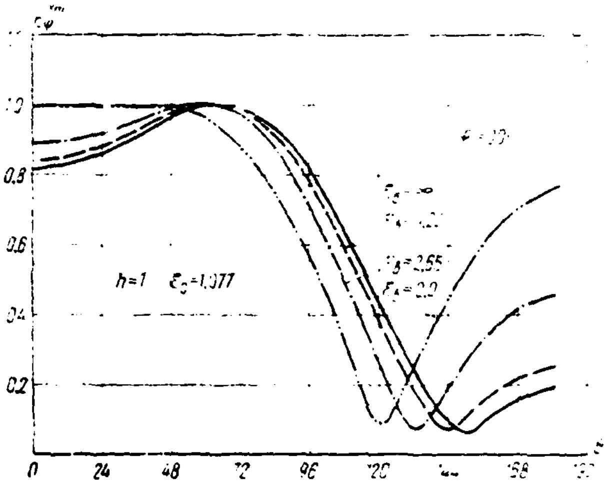

Fig. 3.

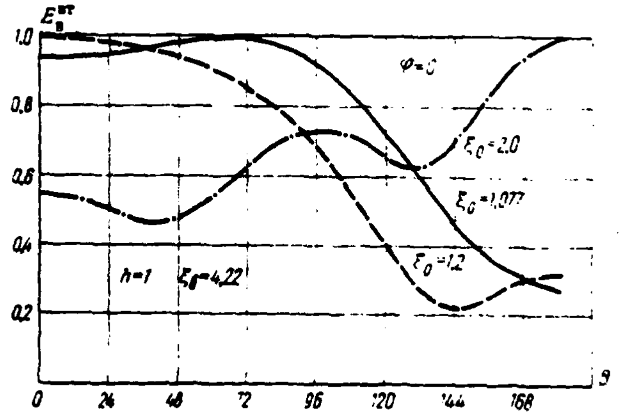

Fig. 4.

this problem, as well as other asymmetrical excitation problems, is the lack of complete tables of spheroidal functions. Instead of tables, it should be agreed that it is often convenient in practical calculations to use a computer program which follows a defined algorithm to compute the required function each time as needed. Such a program can usually successfully replace a table; however, developing an algorithm for calculating spheroidal functions with sufficient accuracy and writing the program represent an independent mathematical problem.

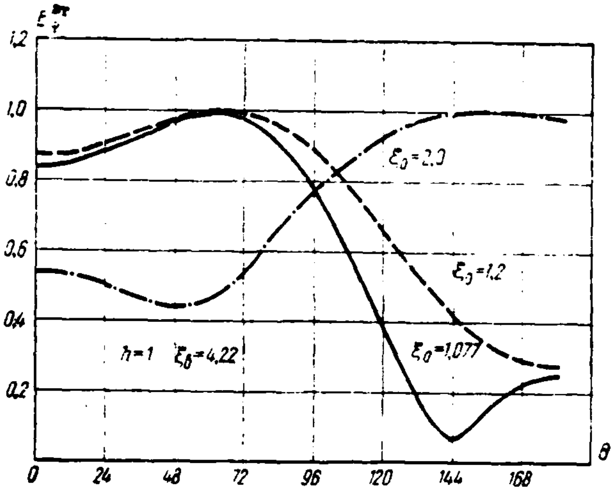

Fig.5.

The present work presents calculations, based on tables, of coefficients of expansion of spheroidal functions [3] which are substantially limited, which results in low accuracy of the result (of the order of 10-20% for the secondary field). The variation in the order of the system of algebraic equations with respect to the unknown coefficients of expansion for the field gives an idea of the accuracy of the solution. In addition, the results make it possible to investigate several interesting relationships.

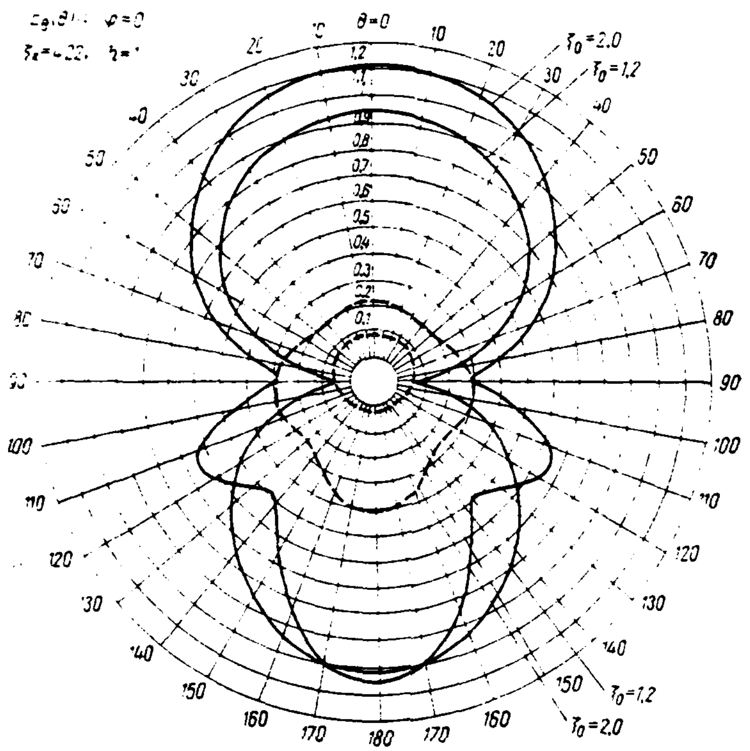

Fig. 6.

Figures 2 and 3 present series of patterns in the plane zx(ϕ=0) and zy(ϕ=π/2), respectively, which illustrates the change in the picture of the secondary field as a function of the distance between the spheroid and the elementary dipole. The directivity pattern changes little for the region of radial coordinates of dipole position ξ_0>4. This indicates that when the distance between the spheroid and the dipole exceeds one-half wavelength, and with a thin spheroid, the secondary field practically coincides with the plane-wave diffraction field.

The series of patterns in Figs. 4 and 5, referring respectively to planes zx(ϕ=0) and zy(ϕ=π/2), illustrate the relationship between the secondary field and the transverse dimensions of the spheroid. This relationship is strong. The patterns for the case of spheroid which is close to a sphere ξ_0=2 differs

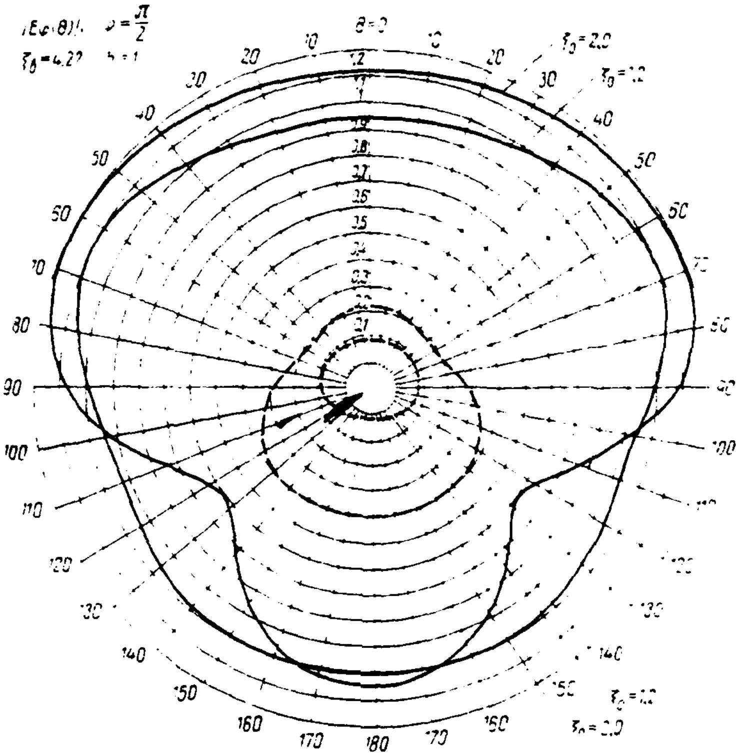

Fig. 7.

sharply from the patterns of thin spheroids.

Figures 6 and 7 use a polar system of coordinates to show the directivity patterns of the total (solid line) and secondary (dotted line) fields in the zx and zy planes. These patterns, as well as other calculations, show that the secondary field in all of the cases examined has significantly lower amplitude than the primary field. Therefore, the patterns of the total field differ from those for the primary field only for near-spherical spheroids.

LITERATURE

1. J. A. Stratton, P. M. Morse, L. J. Chu, R. A. Hutner. «Elliptic Cylinder and Spheroidal wave Functions», New Jork, 1941.

2. J. Meixner, FW Schäfke, «Mathieusche Funktionen und Sphäroidfunktionen», Berlin. 1954.

3. J. A. Stratton, P. M. Morse, L. J. Cnu, J. D. Little, F. J. Corbato, «Spheroidal wave Funktions», New Jork, 1956.

4. Carson Flammer, «Spheroidal wave Funktions». Stauford, California, 1957.

5. Г. Т. Марков «Радиотехника и электроника», т. II, вып. 4, 1957.

6. L. J. Chu, J. A. Stratton. Jour. Appl. Phys., vol. 12, 241, 1941.

7. E. C. Hatcher, A. Leither, Jour. Appl. Phys., vol. 25, 1250, 1954.

8. K. M. Siegel, F. V. Shyltz, B. H. Gere, F. B. Sleater, Trans IRE, AP-4, № 3, 1956.

9. Н. Н. Корбанский. Труды ВВИА им. Жуковского, вып. 630, 1957.

10. М. Г. Белкина. Сборник статей «Дифракция электромагнитных волн на некоторых телах вращения». «Советское радио», 1957.

11. Mayers, Trans, IRE, AP-4. 58, 1956.

12. C. P. Wells, Trans IRE, AP-4, № 1, 1958.

13. Д. А. Дупленков, С. Н. Иванов. Изв. высш. уч. завед. «Радиофизика», т. VII, № 3, 1964.

14. Г. Т. Марков, Д. А. Дупленков, Н. Ф. Осипович. Изв. высш. уч. зав. «Радиофизика», т. VIII, № 1, 1965.

15. Д. А. Дупленков, А. Н. Коваленко, ЖТФ, т. XXXV, № 8, 1965.

16. J. R. Wait, Radio Science, v. 1 (New series) № 4, 1966.

STATISTICS OF FIELD OF LINEAR ANTENNA WITH ARBITRARY AMPLITUDE-PHASE DISTRIBUTION AND ANY FORM OF ERROR CORRELATION COEFFICIENT

V.I. Zamyatin, L.G. Korniyenko

Asymptotic expressions are obtained for the average directivity pattern and efficiency of a linear antenna for the case of small and large (in comparison with antenna length) radii of the correlation phase errors. The expressions are suitable for arbitrary amplitude-phase distribution and any form of error correlation coefficient. A number of examples are examined.

1. As we know, one of the basic problems in statistical antenna theory is that of finding the statistical characteristics of the antenna field for given error statistics. Analytical results naturally depend upon what sort of error statistic we assign. Errors are usually assumed normal and stationary along the antenna. The correlation coefficient is usually Gaussian or exponential. Gaussian form, in particular, is used in [1], which contains the most complete exposition of the fundamentals of statistical antenna theory.

However, situations are possible in practice for which the error statistic differs from that used in [1] or other analogous works. In this connection, it is extremely important to develop statistical theory in the direction of eliminating various assumptions regarding error statistics. In particular, it is desirable to obtain convenient analytical relationships which are suitable for any form of error correlation coefficients. It is difficult to do this for arbitrary values of the error correlation radius. However, such relationships can be obtained for small or large (in comparison with the antenna size) correlation radii. The derivation and analysis of these relationships for arbitrary amplitude-phase distributions comprise the subject of the present article.

2. A linear system of continuously distributed sources with random phase errors is examined. To the extent possible, the directivity pattern will be

$$F(\psi)=\int_{-1}^{1}\int A(x)A^{*}(x_1)\,e^{i[\varphi(x)-\varphi(x_1)]+i\psi(x-x_1)}\,dx\,dx_1, \tag{1}$$

to within a constant factor, where A(x) is the determinate amplitude-phase distribution of the sources, $\phi(x)$ are the phase errors, assumed normal and stationary below, $\psi=\frac{\pi L}{\lambda}\sin\Theta$ is a generalized angle, $x=\frac{2z}{L}$ is a generalized coordinate. The asterisk denotes a complex conjugate quantity.

Averaging equation (1) and using an expression for the two-dimensional characteristic function (cf. for example, [2]), we find the average directivity pattern in terms of power

$$\overline{F}(\psi)=\int_{-1}^{1}\int A(x)A^{*}(x_1)\,e^{-\alpha[1-R(x-x_1)]+i\psi(x-x_1)}\,dx\,dx_1, \tag{2}$$

where $R(x-x_1)$ is the phase error correlation coefficient, and α is their dispersion.

Expression (2) can be transformed as follows:

$$\bar{F}(\psi) = e^{-\alpha}\left[F_0(\psi) + \sum_{m=1}^{\infty} \frac{\alpha^m}{m!} \int_{-1}^{1}\int A(x)A^*(x_1)R^m(x-x_1)e^{i\psi(x-x_1)}\,dx\,dx_1\right] =$$
$$= e^{-\alpha}\left[F_0(\psi) + \frac{1}{2\pi}\sum_{m=1}^{\infty} \frac{\alpha^m}{m!} \int_{-\infty}^{\infty} S_m(\tau)\,F_0(\psi-\tau)\,d\tau\right]. \tag{3}$$

Here $F_0(\psi)$ is the pattern in the absence of errors,

$$S_m(\tau) = \int_{-\infty}^{\infty} R^m(x)\,e^{-i\tau x}dx. \tag{4}$$

The first term in (3) is proportional to the pattern in the absence of errors; the second term determines the scattered (due to phase fluctuations) power. It characterizes the distortion in the shape of the directivity pattern. As we can see from (3), the angular distribution of the scattered power is a function of the type of correlation coefficient and the directivity pattern in the absence of errors.

3. Let us now consider the most important case of small phase errors.

The correlation functions which are used in practice can be represented in the following form:

$$R(x) = r(x)\sum_{n=-\infty}^{\infty} a_n\,e^{i\beta_n x}, \tag{5}$$

where r(x) is the envelope of the correlation coefficient. Here $\sum_n a_n = 1$, since R(0)=r(0)=1.

Now expression (3) takes on the form

$$\overline{F}(\psi) = e^{-\alpha}\left[F_0(\psi) + \frac{\alpha}{2\pi}\sum_n a_n I_n(\psi)\right], \tag{6}$$

where

$$I_n(\psi) = \int_{-\infty}^{\infty} S_r(\psi - \beta_n - \tau)\, F_0(\tau)\, d\tau \tag{7}$$

is the integral of the product of the undistorted pattern and envelope spectrum

$$S_r(\tau) = \int_{-\infty}^{\infty} r(x)\, e^{-i\tau x}\, dx. \tag{8}$$

It is apparent from relationship (6) that calculating the integral in (7) provides the basis for calculating the average pattern. Let us examine this integral for the cases of small and large (in comparison with antenna length L) error correlation radii ρ.

Small correlation radius ($\rho \ll L$). In this case, the spectrum width $S_r(\tau)$ is significantly greater than the width of the directivity pattern. If we assume that the maximum of the directivity pattern in the absence of errors is located in the direction $\psi = b$, then

$$\begin{aligned}\overline{F}(\psi) &\approx e^{-\alpha}\left[F_0(\psi) + \frac{\alpha}{2\pi}\sum_n a_n S_r(\psi - \beta_n - b)\int_{-\infty}^{\infty} F_0(\tau)\, d\tau\right] \approx \\ &\approx e^{-\alpha}\left[F_0(\psi) + \frac{\alpha}{2\pi} S(\psi - b)\int_{-\infty}^{\infty} F_0(\tau)\, d\tau.\right]\end{aligned} \tag{9}$$

Here $S(\tau)$ is the energy spectrum of the phase fluctuations, determined by expression (4) with $m=1$.

As we can see from (9), the angular distribution of the scattered power is independent of the amplitude-phase distribution, and is determined only by the energy spectrum of the phase fluctuations.

Let us consider the matter of antenna efficiency. If we assume that the power radiated by the antenna remains unchanged in the presence of errors, then

$$\frac{\overline{D}}{D_0} = \frac{\overline{F}(\psi)}{F_0(\psi)},$$

where $\overline{D}$ and D_0 are the average efficiency and efficiency in the absence of errors, respectively.

Using (9), we have the following for the case in question ($\rho \ll L$)

$$\frac{\overline{D}(b)}{D_0(b)} = e^{-\alpha}\left[1 + \frac{\alpha}{2\pi} S(b) \int_{-\infty}^{\infty} F_0(\tau)\,d\tau\right] \approx e^{-\alpha}. \tag{10}$$

In writing (10), we discarded the second term inside the square brackets, since $S(b) \ll 1$ when $\rho \ll L$, and the value of the integral is of the order π. The formula $\frac{\overline{D}}{D_0} = e^{-\alpha}$ is often encountered in various articles on antenna statistics. As follows from the above, this relationship is independent of the amplitude-phase distribution and the form of the correlation coefficient.

5. Let us now consider the case in which $\rho \gg L$. In this case, the function $S_r(\psi)$ varies much more rapidly than $F_0(\psi)$. The essential domain of integration in the integral in (7) is near the point $\psi - \beta_n$. Expanding $F_0(\tau)$ near this point, we have the following from (7):

$$I_r(\psi) = \sum_{\varkappa=0}^{\infty} \frac{F_0^{(\varkappa)}(\psi - \beta_n)}{\varkappa!} (-1)^{\varkappa} m_{\varkappa}, \tag{7a}$$

where $m_{\kappa} = \int\limits_{-\infty}^{\infty} S_r(\tau)\tau^{\kappa}\,d\tau = 2\pi(-i)^{\kappa}\, r^{(\kappa)}(0)$ is the kth moment of the envelope spectrum.

Since r(0)=1, r'(0)=0, the first two terms in series (7a) contain no information about the specific form of the correlation coefficient. Therefore, limiting ourselves further to three terms in the series (7a), we obtain the following from (6):

$$\bar{F}(\psi) \approx e^{-\alpha}\left\{F_0(\psi) + \alpha \sum_{n} a_n \left[F_0(\psi-\beta_n) - \frac{r^{(2)}(0)}{2} F_0^{(2)}(\psi-\beta_n)\right]\right\}. \tag{11}$$

It follows from expression (11) that the magnitude and angular distribution of the scattered power is a function both of the shape of the directivity pattern (i.e., the amplitude-phase distribution) as well as the type of correlation function.

6. Let us consider some examples.

a. A linear equiphase antenna with uniform amplitude distribution $A(x) = A_0 = 1/2$[1]. The correlation coefficient R(x)= $R(x) = e^{-\frac{x^2}{c^2}} \cos\beta x$, where $c = \frac{2\beta}{L}$ is the relative radius of the phase error correlation. When $\beta = 0$ we have the Gaussian correlation coefficient form which is widely used in antenna statistics. In the present case:

---

[1] We select the value of A_0 such that the value of the field in the direction of the maximum is equal to unity ($F_0(0)=1$).

$$S_r(\psi) = c\sqrt{\pi}\, e^{-\frac{c^2\psi^2}{4}}, \quad F_0(\psi) = \frac{\sin^2\psi}{\psi^2}.$$

When $c \ll 1$, $S(\psi) \approx c\sqrt{\pi}$ and

$$\overline{F}(\psi) \approx e^{-\alpha}\left[\frac{\sin^2\psi}{\psi^2} - \frac{c\sqrt{\pi}}{2}\alpha\right].$$

The scattered power is independent of the angular coordinates, and is fairly small. Therefore, the influence of the scattered power is felt only in the direction of the nulls of the pattern in the absence of errors.

When c>>1

$$\overline{F}(\psi) = e^{-\alpha}\left\{F_0(\psi) + \frac{\alpha}{2}\left[F_0(\psi-\beta) - \frac{r^{(2)}(0)}{2}F_0^{(2)}(\psi-\beta) + F_0(\psi-\beta) - \right.\right.$$
$$\left.\left. - \frac{r^{(2)}(0)}{2}F_0^{(2)}(\psi-\beta)\right]\right\} = e^{-\alpha}\left\{\frac{\sin^2\psi}{\psi^2} + \frac{\alpha}{2}\left[I(c, \psi-\beta) - I(c, \psi+\beta)\right]\right\}. \qquad (12)$$

where the function $I(c,\psi) = \frac{\sin^2\psi}{\psi^2} - \frac{1}{c^2\psi^4}\left[(3-2\psi^2)\cos 2\psi + 4\psi\sin 2\psi - 3\right]$

is tabulated in [1].

For $\beta=0$, expression (12) coincides precisely with the results in [1] Let us investigate the nature of the variation in the angular distribution of the scattered power $F_p(\psi)$ as a function of the quantity β, which characterizes the oscillation frequency of the correlation function with a relative phase error correlation radius c=6 (Fig. 1). It is apparent from Fig. 1 that as the frequency of β increases, the amount of scattered power in the direction of the main maximum of the theoretical pattern $F_0(\psi)$ gradually decreases, and increases in the vicinity of the side lobes. However, up to a certain value of β the amount of scattered power is maximum in the direction $\psi=0$. The nature of the angular distribution changes qualitatively for $\beta \geq 1.5$. The curve has two peaks with a valley at $\psi=0$. The power is redistributed from the main lobes to the side lobes of the pattern $F_0(\psi)$. As β increases, the maximum scattered power moves away from the ordinate, which for certain values of β leads to a sharp filling of the nulls of the theoretical pattern $F_0(\psi)$.

b. Linear equiphase antenna with Gaussian amplitude distribution

$A(x) = A_0 e^{-\frac{x^2}{B^2}}$ In this case $F_0(\psi) = \left[A_0 B \sqrt{\pi} e^{-\frac{\psi^2 B^2}{4}} \operatorname{Re} \Phi(z)\right]^2$,

where $z = \frac{1}{B} - i\frac{\psi B}{2}$, $\Phi(z) = \frac{2}{\sqrt{\pi}} \int_0^z e^{-t^2} dt$ -- probability integral. If we require that $F_0(0)=1$, then $A_0 = (B\sqrt{\pi} \operatorname{Re} \Phi(z)|_{\psi=0})^{-1}$.

As before, we take the correlation coefficient in the form

$$R(x) = e^{-\frac{x^2}{c^2}} \cos \beta x.$$

When c<<1, the results converge with the results obtained in section a.

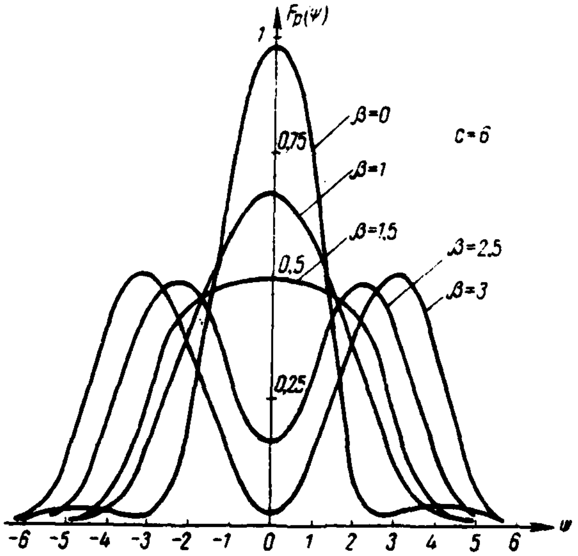

Fig. 1.

[Footnote, not keyed in text: A thorough table of Fourier transforms is given, for example, in [3]. -- Tr.]

Let us consider in more detail the case of large relative radii of phase error correlation (c>>1). In this case

$$\overline{F}(\psi)=\mathrm{e}^{-\alpha}\left\{F_0(\psi)+\frac{\alpha}{2}\left[F_0(\psi-\beta)-\frac{r^{(2)}(0)}{2}F_0^{(2)}(\psi-\beta)+\right.\right.$$

$$\left.\left.+F_0(\psi+\beta)-\frac{r^{(2)}(0)}{2}F_0^{(2)}(\psi+\beta)\right]\right\}.$$

where

$$\frac{1}{A_0^2}F_0^{(2)}(\psi)=B^4\pi\,\mathrm{e}^{-\frac{\psi^2B^2}{2}}[\psi^2B^2-1][\mathrm{Re}\,\Phi(z)]^2+B^3\sqrt{\pi}\,\mathrm{e}^{-\frac{1}{B^2}-\frac{\psi^2B^2}{4}}\times$$

$$\cdot\,\mathrm{Re}\,\Phi(z)[2\cos\psi-3\psi B^2\sin\psi]+2B^4\sin^2\psi\,\mathrm{e}^{-\frac{2}{B^2}}.$$

In order to calculate the quantity $F_0^{(2)}(\psi)$, we can use the table of the values of the function W(z) [4] and the expression

$$\mathrm{Re}\,\Phi(z)=1-\mathrm{e}^{-\frac{1}{B^2}+\frac{\psi^2B^2}{4}}\cdot[\mathrm{Re}\,W(iz)\cos\psi-\mathrm{Jm}\,W(iz)\sin\psi].$$

which can be obtained from the formula $\Phi(z)=e^{-z^2}W(-iz)-1$ [4]. Figure 2 shows curves which characterize the angular distribution of the scattered power $F_p(\psi)$ for c=6 and B=0.5, 5 for the different values of β=0,1,2,3. The values of B are selected such as to equate the angular distribution of the scattered power with a nearly uniform amplitude distribution (B=5) and a distribution which drops off rapidly toward the edges (B=0.5). It is apparent from the figure that the nature of the variations in the curve for the scattered power as a function of the frequency of β for B=0.5 remains the same as for B=5. However, for a dropping amplitude distribution the curves for the scattered power are less sensitive to changes in β. This means that when β varies we should expect a more severe distortion in the shape of the directivity pattern for a uniform amplitude distribution (especially for $\beta \gtrsim 1.5$). The latter is confirmed by Figs. 3 and 4, which show plots of the average directivity patterns in terms of power for B=0,5 (Fig.3) and B=5 (Fig. 4) with a relative phase error correlation radius of c=6 and dispersion α=0.5. It is also apparent from the figures that even for small phase errors and large correlation envelope radii the shape of the average directivity pattern can be distorted significantly (for large β).

7. We examined the case of small phase errors above. However, situations may occur in practice in which the errors are large (α>>1). In this case, we can find an asymptotic expression for the average directivity pattern. Let us look at the solution to this problem for the special case $A(x)=A_0=1/2$. The expression for the average directivity pattern will be

$$\overline{F}(\psi)=\frac{1}{4}\int_{-1}^{1}\int e^{-\alpha[1-R(x-x_1)]+i\psi(x-x_1)}dx\,dx_1.$$

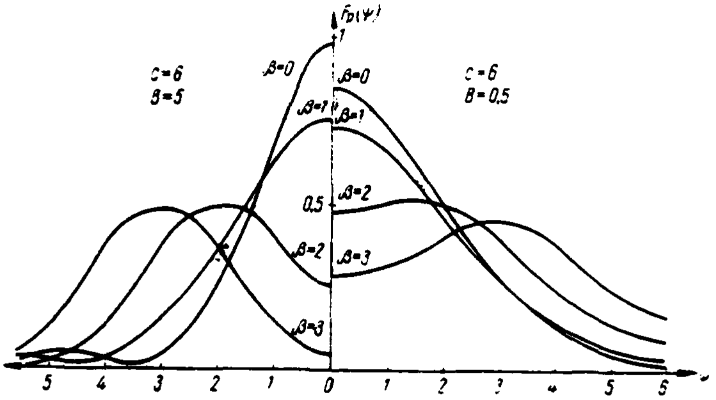

Fig. 2.

When α>>1, the main contribution to the integral is from the region in the vicinity of the point x=0 of the function R(x). Representing the correlation coefficient in the vicinity of this point as

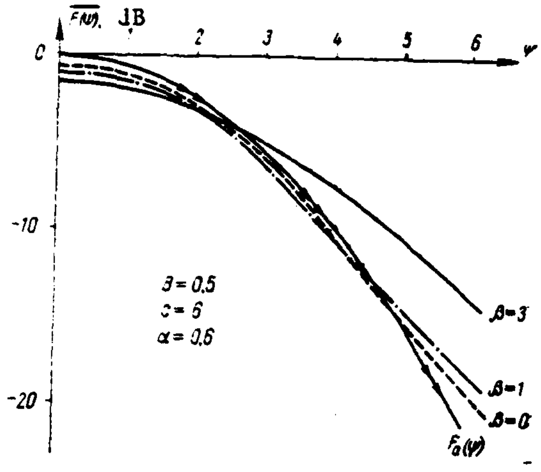
F(ψ), dB
1
2
3
4
5
6
ψ
0
-10
-20
β = 0.5
c = 6
α = 0.6
β=3
β=1
β=0
F₀(ψ)

Fig. 3.

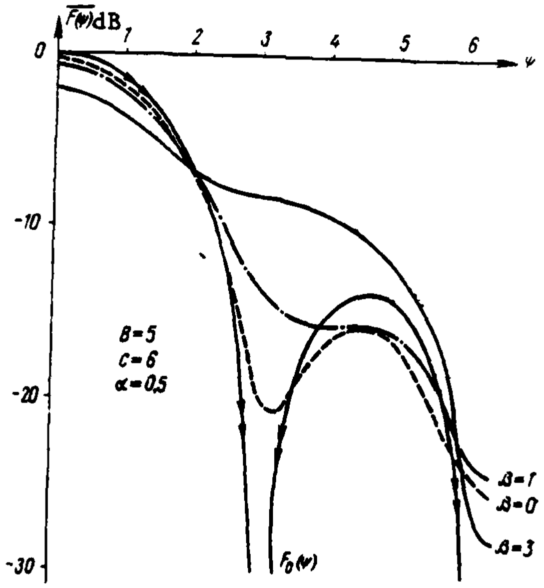
F(ψ) dB
1
2
3
4
5
6
ψ
0
-10
-20
-30
β=5
c=6
α=0.5
β=1
β=0
β=3
F₀(ψ)

Fig. 4.

$$R(x) \approx R(0) - R'(0)x - \frac{R^{(2)}(0)}{2}x^2 = 1 - \frac{R^{(2)}(0)}{2}x^2,$$

we obtain

$$\overline{F}(\psi) = \frac{1}{4}\int_{-1}^{1}\int e^{\frac{\alpha}{2}R^{(2)}(0)(x-x_1)^2+i\psi(x-x_1)}\,dx\,dx_1 = \frac{1}{4}I(c_\alpha, \psi),$$

where

$$c_\alpha = \sqrt{\frac{2}{\alpha[-R^{(2)}(0)]}}.$$

The integral

$$I(c_\alpha, \psi) = \int_{-1}^{1}\int e^{-\frac{(x-x_1)^2}{c_\alpha^2} - i\psi(x-x_1)}\,dx\,dx_1 =$$

$$= c_\alpha^2\sqrt{\pi}\, e^{-\frac{\psi^2 c_\alpha^2}{4}}\,\mathrm{Re}\left[\left(\frac{2}{c_\alpha} - i\frac{\psi c_\alpha}{2}\right)\Phi\left(\frac{2}{c_\alpha} - i\frac{\psi c_\alpha}{2}\right)\right] -$$

$$-c_\alpha^2\left[1 - \psi c_\alpha F\left(\frac{\psi c_\alpha}{2}\right) - e^{-\frac{4}{c_\alpha^2}}\cos 2\psi\right]$$

(Where $F(z) = e^{-z^2}\int_0^z e^{t^2}dt$).

is calculated and tabulated in [1]. Figure 5 shows graphs of the average directivity patterns for various c_α. As c_α drops (for example, as the errors increase), the average directivity pattern is "blurred". At a fairly small value of $-R^{(2)}(0)$, the quantity $c_\alpha \sim 1$ and the pattern acquires directional properties.

We note in conclusion that the methodology developed in this article can be used for other purposes than calculating the average directivity patterns and efficiency. In fact, a number of other statistical characteristics of antennas are also expressed through the integral $I_n(\psi)$, the value of which are given in this article for c<<1 and c>>1.

The authors thank Ya.S. Shifrin for supervising this work.

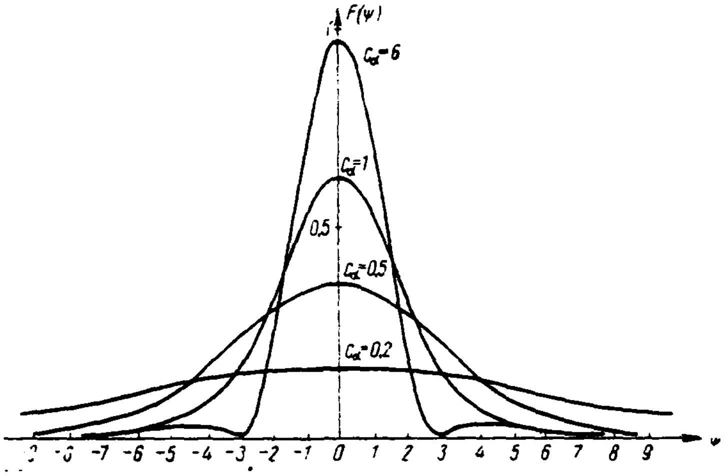

Fig. 5.

LITERATURE

1. Я. С. Шифрин. Статистика поля линейной антенны. Харьков, Артиллерийская радиотехническая академия. 1962.

2. Б. Р. Левин. «Теоретические основы статистической радиотехники». «Советское радио», 1966;

3. В. И. Тихонов. «Статистическая радиотехника». «Советское радио», 1966.

4. В. Н. Фадеева и Н. М. Терентьева. Таблицы значений интеграла вероятности от комплексного аргумента. Гос. изд-во технико-теоретической литературы. М., 1954.

BANDWIDTH PROPERTIES OF DECIMETER-BAND STRIPLINE Y-CIRCULATORS

M.V. Vamberskiy, S.A. Shelukhin, V.I. Kazantsev, B.P. Lavrov

This article analyzes the bandwidth properties of decimeter-band stripline Y-circulators operating above resonance. Recommendations are given on the choice of ferrite brand and basic design dimensions of a Y-circulator which make it possible to obtain a device which is optimal in terms of operating bandwidth. Various methods are considered for correcting the frequency response of Y-circulators.

INTRODUCTION

Ferrite stripline Y-circulators, which are used very widely in microwave technology, have an important disadvantage: the maximum operating bandwidth which can be provided without using any matching devices does not exceed 7-12% in the decimeter band.

The problem of creating Y-circulators with wider bandwidth has until now been solved almost purely experimentally.

Some quantitative relationships are obtained in [1] which illustrate the influence of the parameters of the ferrite and some of the dimensions of a Y-circulator on its bandwidth, but these data are not sufficient for competent design.

The purpose of the present work is to fill in the gap which exists in this area to some extent.

THEORETICAL ANALYSIS OF CIRCULATOR BANDWIDTH PROPERTIES

One possible approach which can be used to obtain quantitative relationships for circulation conditions and to calculate the Y-junction characteristics in the frequency band is to use the apparatus of scattering matrices.

The eigenvalues of the scattering matrix of a ferrite Y-junction with the configuration shown in Fig. 1 are described by the following expression [2]:

$$e^{i\Theta_\kappa} = -\frac{1 + i\frac{3\sqrt{3}Z_\Phi}{Z_0}\frac{h}{R}\frac{1}{4\pi}\sum\limits_{n=3m+\kappa}\left(\frac{\sin n\psi}{n\psi}\right)^2\frac{1}{\frac{n}{x}\frac{k}{\mu}-\frac{J_n'(x)}{J_n(x)}}}{1 - i\frac{3\sqrt{3}Z_\Phi}{Z_0}\frac{h}{R}\frac{1}{4\pi}\sum\limits_{n=3m+\kappa}\left(\frac{\sin n\psi}{n\psi}\right)^2\frac{1}{\frac{n}{x}\frac{k}{\mu}-\frac{J_n'(x)}{J_n(x)}}}, \qquad (1)$$

where k=0,1,2 is the eigenvalue number, m=0, ±1, ±2,...,

$$Z_\Phi = \sqrt{\frac{\mu_0\mu_\perp}{\varepsilon_0\varepsilon_\perp}};\ x = k_\perp R = \frac{2}{\pi}\sqrt{\mu_\perp\varepsilon}R;\ \mu_\perp = \frac{\mu^2 - k^2}{\mu}$$

Here μ_0, ε_0 -- magnetic and dielectric permeability, respectively, of medium filling the lead-in striplines;

ε -- dielectric permeability of ferrite;

μ and k -- diagonal and non-diagonal components of magnetic permeability tensor of ferrite, respectively;

λ -- wavelength in free space;

h -- height of ferrite disc;

R -- radius of ferrite disc;

$J_n(x)$ -- nth order Bessell function of the first sort;

$I_n'(x)$ -- its derivative with respect to x.

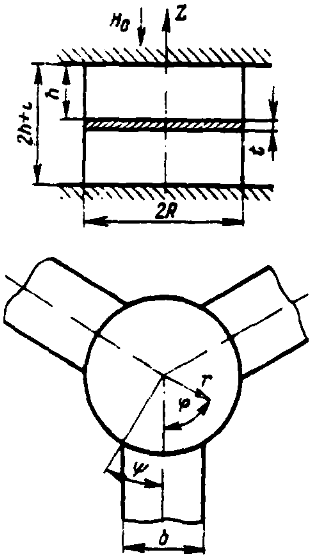

Fig. 1.

Imposing on the eigenvalues thus obtained the following necessary and sufficient conditions for turning a Y-junction into an ideal circulator:

$$\begin{aligned} \theta_0-\theta_1 &= \pm 120^\circ, \\ \theta_1-\theta_2 &= \pm 120^\circ, \\ \theta_2-\theta_1 &= \pm 120^\circ, - \end{aligned} \tag{2}$$

the circulation equations can be obtained.

The equations thus constructed are not limited to an a priori choice of the required number of harmonics excited in the ferrite disc, thus making it possible in principle to find arbitrarily precise relationships between the parameters of the ferrite and geometry of the Y-junction which satisfy the circulation conditions.

As a result of solving these equations by computer and subsequent processing of the results obtained, graphs were constructed (Fig. 2) which demonstrate the interconnection and interdependence at the circulation point between the parameters of the ferrite and the geometry of the Y-junction for various values of $\sigma=\gamma H_0/f$. The use of these graphs makes it easier to design Y-circulators.

Substituting the values found for the quantities x, k/μ, μ_1, h/λ and R/λ for the circulation point in expression (1), and knowing the frequency relationships of the ferrite parameters, we can calculate the eigenvalues within the frequency band. Then, using some connection (cf. e.g. [2]) between the elements of the Y-junction scattering matrix and its eigenvalues, it is also easy to obtain the bandwidth characteristics of the device. The behavior of a Y-circulator in the frequency band can only be described with sufficient accuracy (the better, the smaller the ratio k/μ at the circulation point [1,2]) using the first harmonics excited in the ferrite discs. We use the simple expression obtained in this approximation for the voltage gain of a Y-circulator into a decoupled branch γ (amount of decoupling $P_{\text{раз}}$ =20 log (1/Y), dB):

$$\dot{\gamma} = -\frac{4c^2F^2}{(4c^2-F^2)^2+12c^2F^2} - i\frac{2}{\sqrt{3}}cF\frac{-4c^2-F^2}{(4c^2-F^2)^2+12c^2F^2}, \tag{3}$$

where c=(k/μ)/1.84 and where the value used for the ratio k/μ is that occurring at the circulation point, $F=\frac{J_1'(x)}{J_1(x)}\approx-\frac{\delta f}{f_0}1{,}31$ [3].

Finding the absolute value of γ:

$$\gamma=\frac{2cF}{\sqrt{3}\sqrt{(4c^2-F^2)^2+12c^2F^2}}, \tag{4}$$

we can then connect the Y-circulator bandwidth with the ferrite parameters at the decoupling level of interest.

For the cases which are of interest to developers in which $P_{\text{раз}}$ =20 dB (γ=0.1) and $P_{\text{раз}}$ =15 dB (γ=0.178), we obtain these equations:

$$\frac{2\delta f}{f_0} \simeq 0{,}29\,\frac{k}{\mu} \quad (P_{\text{раз}} = 20\ \text{dB}), \tag{5}$$

$$\frac{2\delta f}{f_0} \simeq 0{,}54\,\frac{k}{\mu} \quad (P_{\text{раз}} = 15\ \text{dB}). \tag{6}$$

Considering that these relationships between operating bandwidth and the ratio k/μ at the circulation point are also valid for calculating using a larger number of harmonics, the frequency scale $2\delta f/f_0$ can be entered beside the scale for k/μ in the graphs above.

The values of the quantities for which the relationship is reflected by the curves in Fig. 2 are limited to those which are maximally realizable in the decimeter band using existing brands of ferrite by the value of relative saturation magnetization ($P_{max} \approx 6$) and values of the angle ψ (cf. Fig. 1) within limits of $15^\circ \leq \psi \leq 35^\circ$. These boundaries are, of course, fairly conditional, since Y-circulators can be created in practice in which the angle ψ will be less than 15° or greater than 35°; however, the accuracy of the proposed calculation is somewhat lower when applied to such devices.

SOME METHODS FOR EXPANDING OPERATING BANDWIDTH OF Y-CIRCULATORS

The operating bandwidth of a tuned Y-circulator can be expanded through two methods: by selecting ferrite parameters and geometrical dimensions for the Y-junction which approximately fulfill the circulation conditions over the broadest possible band of frequencies, or by synthesizing a correcting two-port

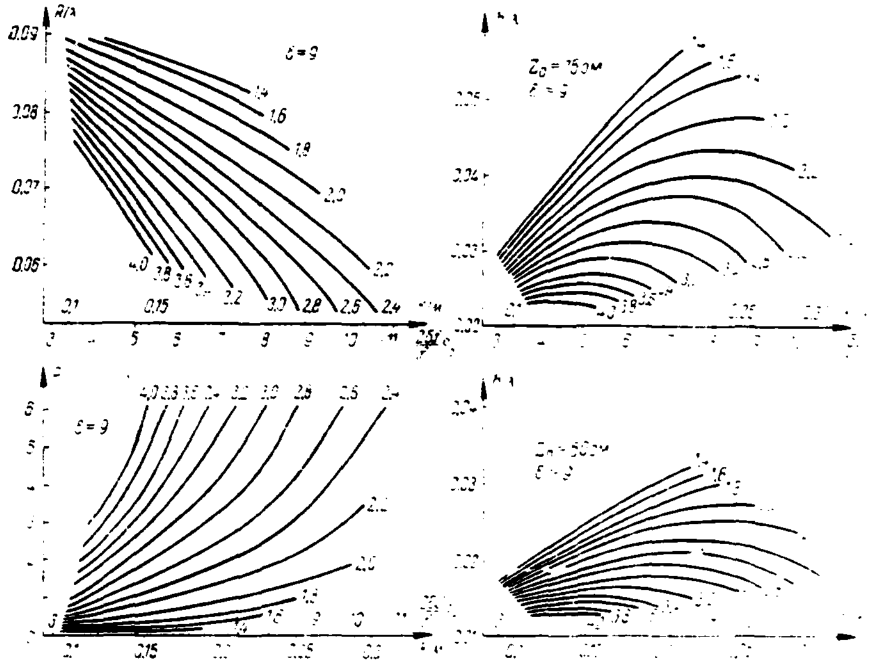

Fig. 2.

network which, when included in all sections of the device, compensates for the effects which occur when there is a departure from the circulation point.

Analysis of the curves in Fig. 2 shows that in order to create Y-circulators with greater bandwidth, ferrites should be used with the highest possible saturation magnetization, and the device should operate with small values of the magnetic field constants.

As the value of σ drops, the dissipative losses in the ferrite increase as a result of the fact that ferromagnetic resonance is approached. This limits the selection of operating values of σ on the part of small magnetic fields.

In the general case, in order to create Y-circulators with wider bandwidth it is desirable to have a material with the highest possible value of p and a narrow ferromagnetic resonance line ΔH.

One result of solving the circulator equations by computer is the relationship

$$\frac{h}{R}\frac{z}{Z_0}\sqrt{\frac{\mu}{\varepsilon}} \simeq 1.1\cdot 10^{-2}\frac{k}{\mu}. \tag{7}$$

This shows that the value of the ratio k/μ at the circulation point is inversely proportional to $\sqrt{\varepsilon}$. Consequently, the operating bandwidth of a Y-circulator increases as ε decreases in approximate proportion to $1/\sqrt{\varepsilon}$, hence the advisability of selecting a ferrite with the smallest possible value of ε .

Using the proposed graphs in designing Y-circulators makes it possible in each specific case to select a design version which provides a device with optimal operating bandwidth. However, as Fig. 2 shows, the maximally attainable bandwidth values are limited to values of approximately 10%, which often is not satisfactory for developers.

The bandwidth of a Y-circulator can be increased by introducing a slight gap between the ferrite discs and the grounded plates or center conductor. This can be explained by the reduced value of the effective dielectric permeability $\varepsilon_{э\phi}$ of the space in the center of the junction. For small gaps, $\varepsilon_{э\phi}$ can be defined using the formula

$$\varepsilon_{э\phi} = \frac{h}{\dfrac{l_з}{\varepsilon_з} + \dfrac{h - l_з}{\varepsilon}}. \tag{8}$$

where $\ell_з$ is the length of the gap; $\varepsilon_з$ is the dielectric permeability of the material in the gap; h is the distance between the center conductor and the grounded plates.

An experiment was conducted in the decimeter band to check this assumption using a prototype in which $\ell_3=0.1h$, $\varepsilon_3=1$, $\varepsilon=9$. The introduction of a gap increased the bandwidth by a factor fo 1.4, which confirms the theoretical conclusions.

Let us now turn to questions of expanding the bandwidth by using external correcting two-ports. As we know [3,4], a nonmutual reactive three-port network with a scattering matrix

$$\vec{S} = \begin{vmatrix} \dot{\alpha} & \dot{\beta} & \dot{\gamma} \\ \dot{\gamma} & \dot{\alpha} & \dot{\beta} \\ \dot{\beta} & \dot{\gamma} & \dot{\alpha} \end{vmatrix}, \tag{9}$$

becomes an ideal circulator when each of its sections has connected to it a reactive two-port in which the coefficient of reflection $\dot{\Gamma}_K$ is related with the elements of the matrix $\vec{S}$ as[1]

$$\dot{\Gamma}_K = \frac{\dot{\gamma}}{\dot{\alpha}\dot{\gamma} - \dot{\beta}^2}. \tag{10}$$

Using the expressions which define the bandwidth dependencies of $\dot{\alpha}$, $\dot{\beta}$, $\dot{\gamma}$ [2], we arrive at the following relationship for $\dot{\Gamma}_K$:

$$\dot{\Gamma}_K = \frac{-F^2 - i2\sqrt{3}\,cF}{F^2 + 12cF} \tag{11}$$

Figure 3 shows the frequency relationships of the absolute value of Γ_K and phase ϕ_K for a value of $k/\mu=0.3$.

---

[1] Equation (10) is written for the case $\gamma<\beta$.

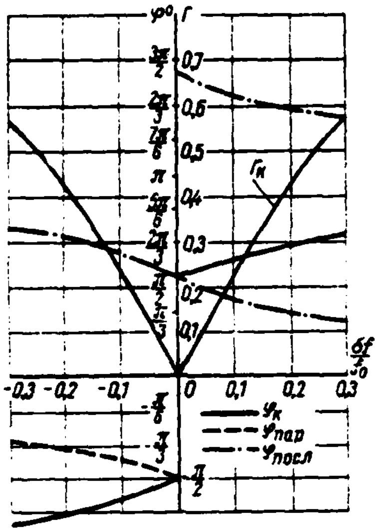

Fig. 3.

Using familiar methods from circuit theory [5] to examine the possibility of synthesizing reactive two-ports which implement the frequency relationship (11), we can arrive at the conclusion that they cannot be used to implement this relationship.

The characteristics of a Y-circulator can be improved significantly by using correcting two-port networks in which the coefficient of reflection is complex-conjugate with the coefficient of reflection $\dot{\alpha}$ of the original circulator:

$$\dot{\Gamma}_{\kappa} = \alpha^{*}. \qquad (12)$$

However, research analogous to the foregoing indicated that this frequency relationship is also impossible to realize using reactive (or, in the general case, passive) two-port networks.

Analyzing the frequency dependence of the absolute value of the coefficient of reflection needed for optimal correction, we can conclude that the latter can be realized by connecting two-port networks with the circuits shown in Fig. 4, where the Q of the tuned circuits are related with the quantity k/μ at the circulation point as

$$Q = \frac{0.696}{k/\mu}. \quad (13)$$

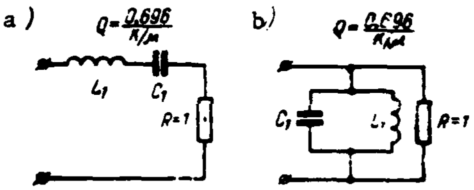

Fig. 4.

The frequency dependencies of the phases of the coefficients of reflection from these two-ports, assuming that a matched load (R=1) is connected to their input terminals, appear as

$$\varphi_{\text{посл}} = \arctan \frac{1,435k/\mu}{\delta f/f_0}, \quad (14a)$$

$$\varphi_{\text{пар}} = \pi - \arctan \frac{1,435k/\mu}{\delta f/f_0}. \quad (14b)$$

As can be seen from Fig. 3, the phase characteristics ϕ_K and $\phi_{\text{посл}}$ diverge rather substantially, with the divergence being the greater, the further the current frequency f is from the circulation frequency f_0. Obviously, in order to obtain the required phase values for the coefficient of reflection, the tuned circuit (Fig. 4b) which is connected to the line in parallel must be located at a distance of $\ell = \lambda_0/4$ from the ferrite-air interface plane.

An equivalent for a series resonant tuned circuit in the microwave range is a shorted line segment with length of $\lambda_0/2$, or a segment of open-ended line with length of $\lambda_0/4$. Considering (13), we express the characteristic impedances of these segments (stubs) through k/μ :

$$Z^{\text{кз}}_{0\,\text{посл}} = \frac{0{,}444}{k/\mu}, \tag{15a}$$

$$Z^{\text{рэ}}_{0\,\text{посл}} = \frac{0{,}888}{k/\mu}. \tag{15b}$$

The maximum bandwidth of a Y-circulator if series-connected stubs are used for correction is limited by the increase in phase error as the deviation from the circulation frequency becomes greater. Allowing for the influence of this phase error on the characteristics of a Y-circulator with series-connected stubs in its branches made it possible to calculate its bandwidth for various values of the ratio k/μ at the circulation point. Figure 5 shows the relationship obtained, which is approximated fairly accurately by the straight line

$$\frac{2\delta f}{f_0} = 0{,}63\,\frac{k}{\mu}. \tag{16}$$

If we move the point at which the stub is connected away from the plane of the ferrite-air interface, we can satisfy the conditions of optimal correction both with respect to absolute value and phase at frequencies f_1 or f_2, respectively lower or higher than the circulation frequency; the frequency characteristics of the circulator then have two peaks with a second extremal point at these frequencies. Figure 5a also shows the maximum bandwidth as a function of k/μ for these cases. In order to realize the bandwidths shown in this figure, the stub must be connected at a point approximately $1.6\lambda_0/4$ from the ferrite-air interface plane in order to obtain the second decoupling peak at a frequency higher than the circulation frequency of the original junction ($f_1>f_0$); this distance is approximately $0.3\lambda_0/4$ in order to obtain an analogous effect at a frequency $f_2<f_0$.

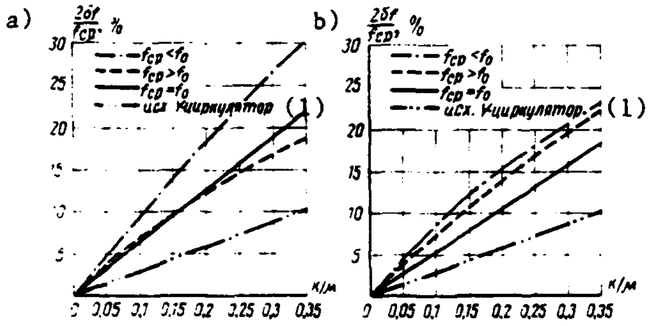

Fig. 5.. .

Key: (1) original Y-circulator.

Thus, series-connected stubs can be used to expand the bandwidth of a Y-circulator significantly. However, these are difficult to execute, especially at high power levels.

A simple equivalent to a parallel resonant tuned circuit in the microwave range is either a shorted line segment with length of $\lambda_0/4$, or a segment of open-ended line $\lambda_0/2$ long. In this case, the required values of the impedance characteristics are calculated by the formulas

$$Z^{\text{рз}}_{0\text{пар}} = 2{,}26\,\frac{k}{\mu}, \tag{17a}$$

$$Z^{\text{кз}}_{0\text{пар}} = 1{,}13\,\frac{k}{\mu}. \tag{17b}$$

Figure 5b shows the bandwidth at the 20 dB decoupling level as a function of the ratio k/μ at the circulation point for correction using parallel stubs connected at a point $\lambda_0/4$ from the plane of the ferrite-air interface. This relationship is approximated fairly closely by the straight line

$$\frac{2\Delta f}{f_0} \simeq 0{,}5\frac{k}{\mu}. \tag{18}$$

If we change the distance from the point at which the stub is connected and the ferrite-air interface plane we can, like in the case above, obtain a circulator frequency response with two peaks. Figure 5b shows the maximum bandwidth as a function of the ratio k/μ for these cases as well. The optimal distances for the stub connection point are approximately $\sim 0{,}7\frac{\lambda_0}{4}$ for frequencies higher than the circulation frequency, and approximately $\sim 1{,}4\frac{\lambda_0}{4}$ for frequencies below the circulation frequency.

In order to check the proposed relationships experimentally, a stub was used to expand the bandwidth of a Y-circulator, the characteristics of which are shown by the fine lines in Fig. 6 ($p=1$, $\sigma=1.8$). The ratio $k/\mu=0.25$ for this device. The following are the required values for the impedance characteristics:

$$Z_{0\text{пар}}^{\text{рэ}} = 56{,}5 \text{ Ohms},$$
$$Z_{0\text{пар}}^{\text{кэ}} = 28{,}2 \text{ Ohms},$$

Since it is fairly hard to realize a characteristic impedance of $Z_0=28.2$ Ohms, the correction was done using half-wave open-ended stubs. The heavy lines in Fig. 6 show the responses of a Y-circulator with the stubs. In order to achieve maximum bandwidth, an experiment was conducted to obtain a response with two peaks at frequencies below the circulation frequency. As a result (Fig. 7), the following responses were obtained with a band of ±10.5% of the center frequency:

$$P_{\text{раз}} \quad 20\ \partial б,\ P_{\text{вн}} \leqslant 0{,}8\ \partial б, \text{VSWR} \leqslant 1{,}4.$$

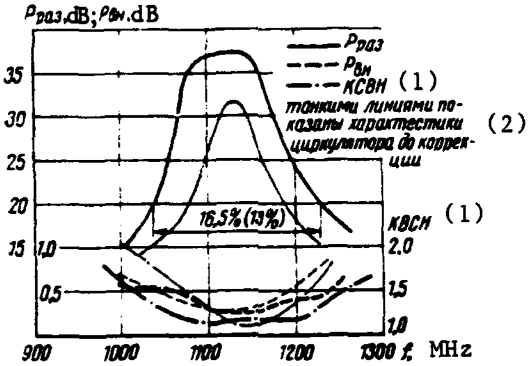

Fig. 6.

Key: (1) VSWR (voltage standing-wave ratio;
(2) fine lines indicate circulator response
prior to correction.

As was indicated above, it is fairly hard to implement series-connected stubs in striplines. Therefore, an experiment to illustrate their effect on the responses of a Y-circulator was setup using a Y-circulator with coaxial input feeders (Fig. 8), which made the configuration of the junction significantly different from that under consideration. With a value of $Z_0=3$ (at a calculated value of 6.3) and stub length of $\lambda_0/4$, the use of these stubs expanded the bandwidth at the 20 dB decoupling level from 4.8% to 14% (the bandwidth expansion was somewhat asymmetrical).

There is also another way to expand the bandwidth of Y-circulators which differs in principle from that explained above. A Y-junction with a ferrite is assigned so that, without being an ideal frequency at any of the frequencies within the range in question, it has frequency responses which are optimal for correction. This method can be implemented by using Y-circulators with dielectric transformers. The optimality criterion for the frequency responses of the original Y-junction should be compactness of the curves of its impedance within the frequency range on a circle diagram. Calculations showed that if the

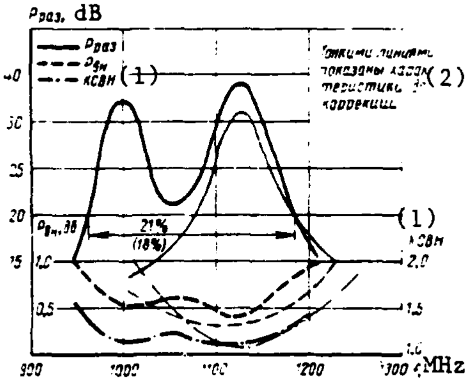

Fig. 7.

Key: (1) VSWR; (2) fine lines show responses prior to correction.

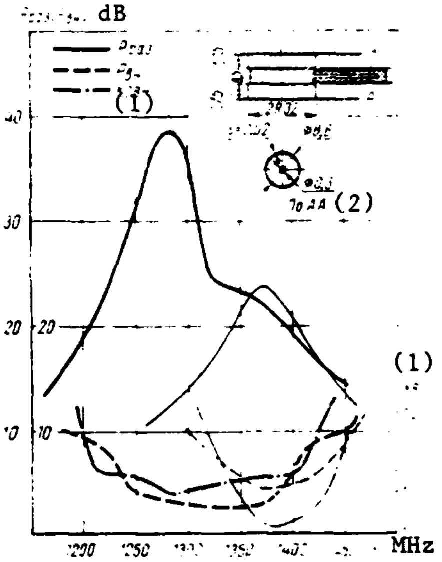

Fig. 8.

Key: (1) VSWR: (2) along AA.

imaginary component of the impedance $\dot{Z}$ of a Y-junction with a ferrite is zero at the center frequency of the band, the degree of compactness of the curve $\dot{Z}=\phi(f)$ (where f is frequency) is a function of the size of its real component R_0 at the circulation frequency f_0. Figure 9a shows the frequency dependency of $\dot{Z}$ for different values of R_0 (0.2, 0.3, 0.4, 0.5, 0.6, 0.7, 0.8, 1.0). The curves for $\dot{Z}=\phi(f)$ corresponding to $R_0=0.5-0.6$ are most compact. A circulator can now be obtained by connecting appropriate quarter-wave transformers to all of the Y-junction inputs.

It should be noted, however, that coupling between different branches of the initial Y-junction has a significant effect on the responses of a circulator obtained as a result of this correction.

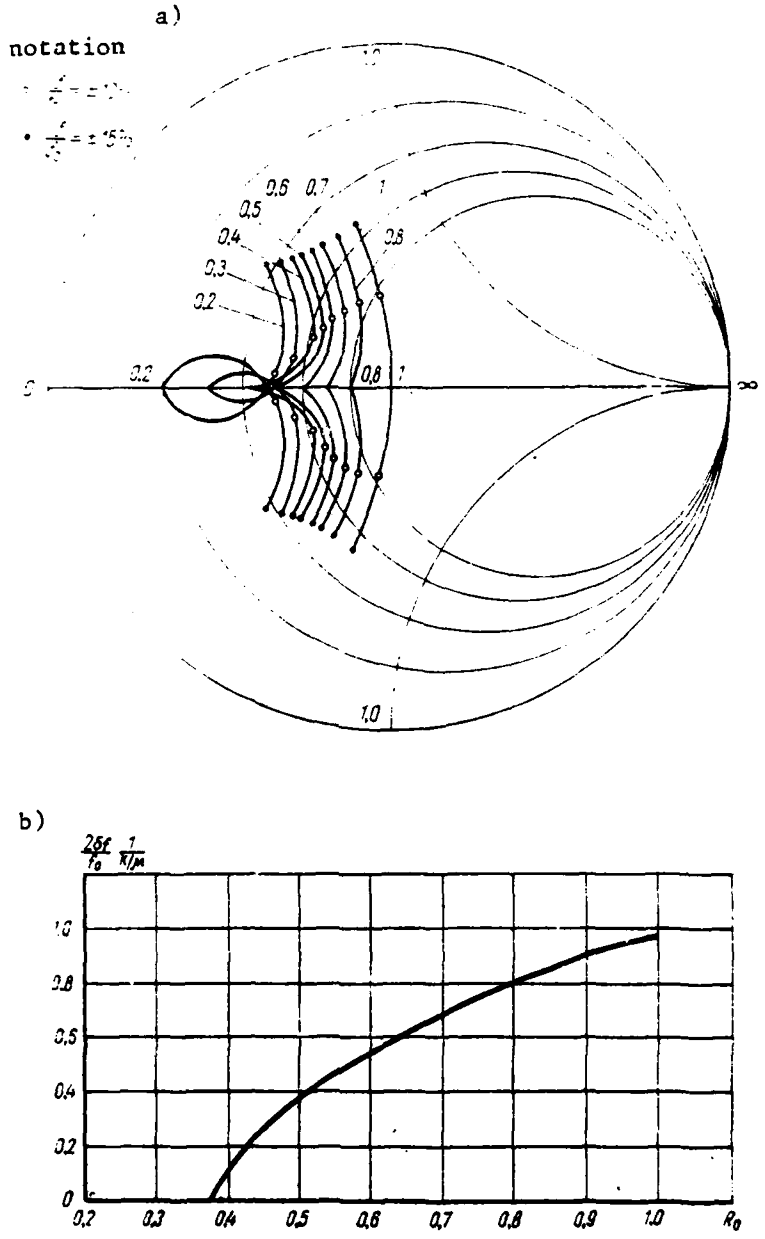
a)
notation
○ $\frac{f}{f_0} = \pm 10\%$
• $\frac{f}{f_0} = \pm 15\%$
1.0
0.6
0.7
1
0.5
0.4
0.3
0.2
0.8
0.2
0
0.8
1
∞
1.0
b)
$\frac{2\delta f}{f_0}\frac{1}{K/\mu}$
1.0
0.8
0.6
0.4
0.2
0
0.2
0.3
0.4
0.5
0.6
0.7
0.8
0.9
1.0
R_0

Fig. 9.

It can be shown that in the similar case in which the correcting devices are two-ports in which the coefficient of reflection is complex-conjugate with the coefficient of reflection of the original Y-junction, decoupling of greater than 20 dB can only be obtained if the decoupling provided at that frequency by the original junction $P_{раз} \geq 10.5$ dB. Invescigation of the frequency responses of a Y-junction with a ferrite showed that the width of the frequency band within which the original junction provides this decoupling is a strong function of R_0 (Fig. 9b). Comparison of the data in Fig. 9a and 9b allows to conclude that only when $R_0 \approx 0.5$-0.6 does the use of transformers allow maximum utilization of the capabilities of obtaining decoupling exceeding 20 dB within the frequency band.

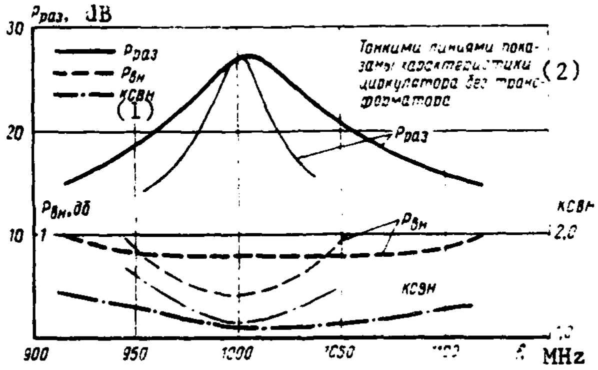

Fig. 10.

Key: (1) VSWR; (2) fine lines indicate circulator responses without transformer.

Selecting thus the quantity R_0, the geometrical dimensions of the ferrite discs can be calculated using the following formulas:

$$\frac{R}{\lambda} = \frac{0.29}{\sqrt{\mu_\perp \varepsilon}};$$

$$\frac{h}{\lambda} = A \frac{k/\mu}{\mu_\perp} \sqrt{\frac{R_0}{2 - R_0}}; \qquad (19)$$

$A = 0.35$ for $Z_0 = 75$ Ohm;
$A = 0.2$ for $Z_0 = 50$ Ohm.

Putting quarter-wave transformers with characteristic impedances $Z_T=\sqrt{R_0}$ in all branches of the Y-circulator designed using these data, we obtain a device which can operate in a near-circulation mode. Figure 10 shows the responses of two Y-circulators which use a 30SCh4 ferrite and have ferrite discs with equal heights. The ferrite discs in the Y-circulator without transformers had dimensions of h=7.8 mm, R=25 mm. A value of R_0=0.5 was selected for the case in which transformers were used, hence the disc radius of R=21.5 mm at the same height for the following transformer specifications: ℓ_T=49 mm (ℓ_T -- transformer length), ε_T=2.05 (ε_T -- dielectric permeability of transformer material). Polystyrene was the material used for the transformer. The best bandwidth characteristics were obtained with ℓ_T=45 mm for discs with a radius of R=21 mm. The bandwidth at the 20 dB level was approximately twice that of a circulator without transformers. The value of the magnetizing field in the device using transformers was 1.7 times lower than without transformers; the induced losses were somewhat higher, but agree well with the conclusions which follow from analyzing relationships (19).

CONCLUSION

Analysis of the bandwidth properties of ferrite plane Y-circulators operating beyond resonance indicates that the maximum attainable frequency bandwidth for these devices at the 20 dB decoupling level is 10-12% (without any matching devices).

As a result of investigating various methods for expanding bandwidth, it was established that introducing a gap between the ferrite specimens and grounded plates or inside conductor increases the bandwidth by a factor of 1.3-1.4; the use of series-connected stubs approximately triples the bandwidth, while parallel stubs and dielectric transformers increase the bandwidth by a factor of 2-2.5.

Specific requirements will dictate the use of each of the methods examined above. However, in most cases, especially when operating at high power levels, it is better to use parallel stubs, rather than series-connected, since the latter are difficult to build.

LITERATURE

1. Bosma H. «Полосковый Y-циркулятор». IEEE Trans on MTT, 1964, MTT-12, № 1.
2. Вамберский М. В., Шелухин С. А. «Применение метода собственных значений к расчету диапазонных характеристик полосковых Y-циркуляторов». XXII Всесоюзная Научная сессия, посвященная Дню радио, секция: Квантовая электроника, 1966.
3. Humphreys B. L., Dovies J. B. Синтез N-плечевых циркуляторов. IEEE Trans on MTT, 1962, MTT-10, № 6.
4. Вамберский М. В., Шелухин С. А., Гаврилов В. С. «Частотная коррекция ферритовых полосковых Y-циркуляторов реактивными четырехполюсниками». XXI Всесоюзная научная сессия, посвященная 70-летию со дня изобретения радио А. С. Поповым, секция квантовой электроники, 1965.
5. Сешу Сундалян, Балабанян Норман. «Анализ линейных цепей». Госэнергоиздат, 1963.